
**Towards Functional Optoelectronic
Nanocrystal Solids:
CuIn(Ga)Se₂, In_xSe_y and GaAs**

In Richtung funktioneller optoelektronischer
Nanokristall Festkörper:
CuIn(Ga)Se₂, In_xSe_y und GaAs

DISSERTATION

zur Erlangung des Doktorgrades
im Fachbereich Chemie
der Universität Hamburg

vorgelegt von

JANNIKA LAUTH
aus Offenbach am Main

NOVEMBER 2013

'The most exciting phrase to hear in science, the one that heralds new discoveries, is not 'Eureka!' but 'That's funny...'
-Isaac Asimov

The experimental work described within this thesis has been carried out between April 2010 and August 2013 at the Institute of Physical Chemistry at the University of Hamburg in the group of Prof. Dr. Horst Weller.

This dissertation essentially contains carried out and complemented scientific work which has been published under first authorship by Jannika Lauth in *Chemistry of Materials* and *Advanced Functional Materials*.

1. Reviewer: Prof. Dr. Horst Weller
2. Reviewer: Prof. Dr. Alf Mews

Date of thesis defense: 24.01.2014

Table of Contents

1	Introduction	1
2	Background Information and Theory	4
2.1	CuInSe ₂ and CuIn _{1-x} Ga _x Se ₂	4
2.2	Nucleation and Growth in Nanocrystals	8
2.3	Application of CuInSe ₂ and CuIn _{1-x} Ga _x Se ₂ Nanocrystals in Quantum Dot Solar Cells	11
2.4	Initial Ligands and Ligand Exchange	13
2.4.1	Initial Ligands	13
2.4.2	Ligand Exchange	14
2.5	Electrical Transport in Nanocrystal Solids	16
2.6	Indium Selenide and Assembly of 2D Indium Selenide Nanosheets	19
2.7	Gallium Arsenide	21
3	Results and Discussion	23
3.1	Trigonal pyramidal CuInSe ₂	25
3.2	Elongated CuInSe ₂	27
3.3	CuIn _{1-x} Ga _x Se ₂ NCs	30
3.4	Choice of Precursors	34
3.4.1	Selenourea	34
3.4.2	Selenium	34
3.4.3	Bis(trimethylsilyl)selenide	34
3.4.4	Copper Precursors	36
3.4.5	Indium and Gallium Precursors	36
3.5	Ligand Exchange and Nanocrystal Surface Modification of CI(G)S	38
3.5.1	Ligand Exchange: 1-Ethyl-5-thiotetrazole	38
3.5.2	Ligand Exchange: 1-Methyl-5-thiotetrazole	49
3.5.3	Surface Modification: Meerwein's Salt (Et ₃ OBF ₄)	56
3.6	<i>In-situ</i> XRD Heating Experiments - Sintering CIS NCs	61
3.7	<i>In-situ</i> TEM Heating Experiments - Sintering CI(G)S NCs and X-ray Photoelectron Spectroscopy of CIS Surfaces	67
3.7.1	Sintering Elongated CuInSe ₂ -ETT NCs	72

Table of Contents

3.7.2	<i>In-situ</i> TEM Heating of OLA Stabilized Elongated CuInSe ₂ NCs	79
3.7.3	Sintering CuIn _{1-x} Ga _x Se ₂ -ETT NCs	85
3.8	Small Angle X-ray Scattering (SAXS) of CI(G)S NCs	89
3.9	Electrical Transport Measurements and Conductivity	91
3.9.1	ETT stabilized CuInSe ₂ and CuIn _{1-x} Ga _x Se ₂ NCs	92
3.9.2	MTT stabilized CuInSe ₂ and CuIn _{1-x} Ga _x Se ₂ NCs	100
3.9.3	OLA stabilized CuInSe ₂ and CuIn _{1-x} Ga _x Se ₂ NCs	101
3.10	2D Indium Selenide Nanosheets	103
3.11	Gallium Arsenide Nanocrystals	109
3.11.1	Three-step Formation of III-V Nanocrystals	109
3.11.2	Molecular Gallium to Arsenic Ratio in the Reaction	111
3.11.3	Reactivity of Gallium(III) Halides and HSAB Principle	112
3.11.4	GaAs Synthesis Reaction Temperature	113
3.11.5	Applicability of the Transmetalation Reaction	113
4	Summary	115
5	Experimental	118
5.1	CuInSe ₂ and CuIn _{1-x} Ga _x Se ₂ NC Syntheses	118
5.1.1	Trigonal pyramidal CuInSe ₂	118
5.1.2	Elongated CuInSe ₂	119
5.1.3	CuIn _{1-x} Ga _x Se ₂	119
5.2	Choice of Selenium Precursors	121
5.2.1	Elemental Selenium	121
5.2.2	Bis(trimethylsilyl)selenide	121
5.3	Ligand Exchange and Surface Modification	122
5.3.1	1-Ethyl-5-thiotetrazole (ETT)	122
5.3.2	1-Methyl-5-thiotetrazole (MTT)	122
5.3.3	Meerwein's Salt (Et ₃ OBF ₄)	123
5.4	2D Indium Selenide Nanosheets	124
5.5	GaAs Nanocrystals	125
5.6	Methods and Equipment	126
5.7	Chemicals - Safety and Waste Disposal	128
6	GHS List	133
	Acronyms	144
	Acknowledgments	153
	Curriculum Vitae	155

Publications

156

Affirmation

158

1 Introduction

Rethinking and restructuring our understanding of energy resources away from fossil fuels and towards regenerative energy approaches is a constant and ever-growing concern.

The sun represents a promising renewable energy source: One hour of its power reaching the earth's surface could provide one year of the world's energy need, if only harvested efficiently.

Solar energy is reliably clean and cheap and has driven the invention of solar cells for harvesting it a long way with many different materials as absorbers and increasing efficiencies of the devices.

Still, most of the solar cells in everyday use are semiconductor silicon-based even though the performance of the material is determined by its small absorption coefficient and indirect band gap, causing devices to be tens of microns thick to enable efficient solar energy absorption. Especially in the emerging thin film solar cell sector the use of silicon therefore is confined.

It is constantly searched for semiconductor absorber materials that exhibit high sun conversion efficiencies but at the same time at reasonable costs.

Among a variety of different solar cells, semiconductor thin film devices have become increasingly popular as they feature high sun conversion efficiencies at smaller material quantities and thereby can save costs.

CuInSe_2 and $\text{CuIn}_{1-x}\text{Ga}_x\text{Se}_2$ (CI(G)S) have been extensively studied for the application in solar cells as they exhibit a direct band gap suitable for best sun conversion efficiencies at AM1.5 (see 2.1).^[1,2]

One crucial problem in processing the materials for applications is the relatively complicated ternary (quaternary) CI(G)S system. Commonly used reaction pathways involve evaporation of the reaction components at high vacuum and selenization methods which are expensive, complex and do not always assure a distinct stoichiometry of the materials.

Furthermore, the application of the CI(G)S materials as so called "inks" on flexible substrates (for novel solar cell applications like bendable devices) requires production and processing temperatures well below gas phase reaction temperatures.

An alternative way to control the desired stoichiometry of CI(G)S and avoid hazardous reactions from the gas phase are wet-chemical synthesis approaches for CI(G)S nanocrystals (NCs). Colloidal CI(G)S NCs from solution

can be processed as "inks" onto different substrate types and additionally exhibit distinct favorable properties which are described in detail in section 2.3.

The main goals of this thesis are

- The development of synthetic pathways to colloidal I-III-VI₂ nanostructures and the related compounds In_xSe_y and GaAs.
- The application of a residue-free ligand exchange strategy to improve sintering processes in I-III-VI₂ NCs.
- Electrical transport studies on I-III-VI₂ NCs towards their suitability for and application in solar cells.

First, CuIn(Ga)Se₂ NCs of high quality in terms of crystallinity, reproducibility and size distribution are synthesized. Synthesis ways from literature are therefore improved to enable the comparison of the materials' performance in electrical transport measurements.

Second, a ligand exchange procedure for the obtained CI(G)S NCs is established. The NCs are exchanged with 1-ethyl-5-thiotetrazole (ETT) as thermally degradable ligand which on the one hand secures their colloidal stability and on the other hand decomposes virtually residue-free.

Third, densely packed CI(G)S NC solids are produced by spin-coating of the materials. Electrical transport measurements and conductivity determination of the CI(G)S are performed subsequently.

Conductivities of ligand exchanged NC films are determined in the dark and under illumination and compared to conductivities of initially oleylamine stabilized CI(G)S films which generally suffer from poor conductivity.

After thermolysis of the thermally degradable ligand, CI(G)S NC solids feature significantly improved conductivity, underpinning the important role of 1-ethyl-5-thiotetrazole for processing virtually bare NCs from a wet-chemical approach.

The virtually bare CI(G)S NCs can be easily sintered to form dense chalcopyrite films without altering the crystal phase in a temperature range of ~ 400 °C.

Pursuing the reactivity of certain components of the I-III-VI₂ compounds, In_xSe_y nanostructures are synthesized. The obtained two-dimensional In_xSe_y nanosheets show that the reaction mechanism for the structure formation is changed when copper is omitted from reaction and the stabilizing ligand is slightly varied. In_xSe_y sheets represent exceptionally thin layered semiconductor materials that are very interesting (see 2.6) for electrical transport measurements although the stoichiometry of the material has to be further elucidated.

Connecting the role of the third main group elements indium and gallium with additional promising semiconductor materials for solar cells, a general synthesis route for III-V NCs, mainly GaAs, is established.

The presented transmetalation reaction pathway offers the possibility to process the most common III-V NCs: GaAs, InP, InAs and GaP.

In this work it is shown that by carefully probing and adjusting the reaction conditions and behavior of the different elements in the compounds investigated, rather complicated I-III-VI₂ and III-V NCs can be rationally controlled to yield promising functional materials for regenerative energy conversion.

2 Background Information and Theory

This chapter deals with the properties and features of the investigated materials.

Reaction mechanisms for the formation of $\text{CuIn}(\text{Ga})\text{Se}_2$ from the solid state side of view are considered and connected to the compound formation at the nanoscale.

Basics of nanocrystal formation are elucidated in terms of nucleation and growth conditions. All investigated systems show non-classical nucleation and growth (see 2.2).

The application of CI(G)S NCs as absorbers in quantum dot solar cells is discussed and analyzed as well as the functionalization of the NC surface prior to the determination of the electrical transport in organics-free closely assembled NC solids.

The chapter is completed by the characterization of two-dimensional In_xSe_y nanosheets and GaAs NCs.

2.1 CuInSe_2 and $\text{CuIn}_{1-x}\text{Ga}_x\text{Se}_2$

CuInSe_2 and $\text{CuIn}_{1-x}\text{Ga}_x\text{Se}_2$ represent promising materials for regenerative energy conversion and thin film solar cells and have been extensively studied. The direct band gap of 1.04 eV for pure CIS is adjustable by the amount of gallium incorporated into the crystal lattice resulting in an increased band gap of up to ~ 1.15 eV which is close to the optimum of best sun conversion efficiencies at AM1.5.^[1,2] This tunability and its high absorption coefficient surpassing 10^5 cm^{-1} predestine the material for the use in thin film solar cells.^[3] Figure 2.1 is adapted from Jaffe and Zunger^[4] and shows the superior absorption of CuInSe_2 in comparison with other semiconductor photovoltaic materials at AM1.5.

The chalcopyrite crystal structure unit cell of the $\text{CuIn}(\text{Ga})\text{Se}_2$ system can be described as two face centered cubic unit cells stacked into each other in c-direction. Every second tetrahedral hole is thereby occupied by selenium atoms (see Figure 2.2.).

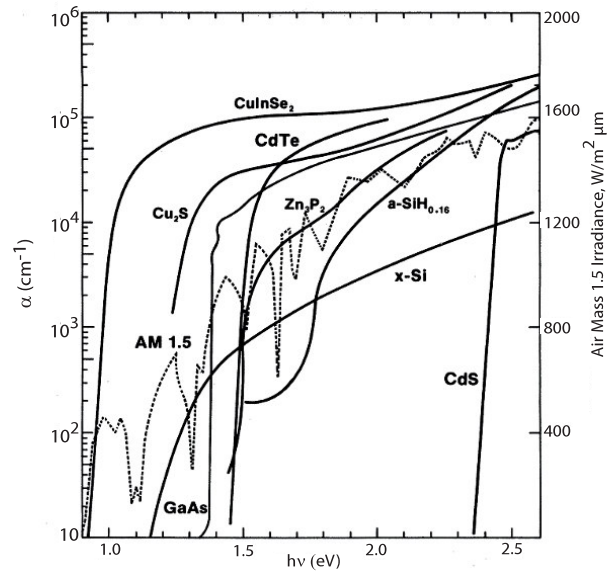


Figure 2.1: Absorption of CuInSe_2 in comparison with other established semiconductor photovoltaics, Figure adapted from reference^[4].

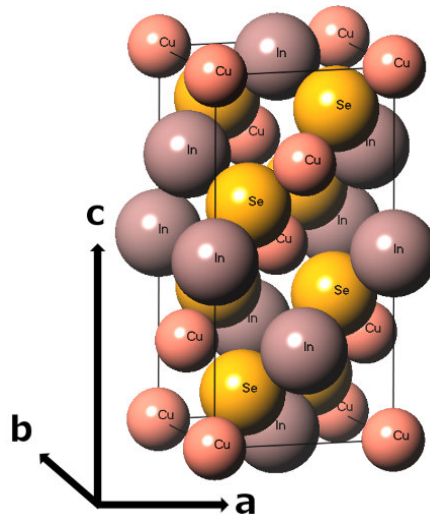
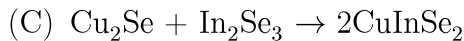


Figure 2.2: Crystal structure of CuInSe_2 and $\text{CuIn}_{1-x}\text{Ga}_x\text{Se}_2$, theoretically In^{3+} atoms can be linearly replaced by Ga^{3+} atoms.

A detailed description of the formation mechanism of $\text{CuIn}(\text{Ga})\text{Se}_2$ in solid state reactions has been predicted and experimentally proven by Hergert *et al.* using *in-situ* XRD.^[1,5,6]

Different formation ways for the chalcopyrites from the binary compounds copper selenide and indium selenide which form first are described:



In the solid state reaction In_4Se_3 is formed in a first step. To yield InSe for reaction (A) or (B), this In_4Se_3 is selenized in a subsequent step by CuSe_2 which forms from excess selenium by reaction (E).

Eventually InSe and CuSe are released in (E) for reaction *via* (A) to yield CuInSe_2 . CuSe additionally can "lose" selenium yielding Cu_2Se for reaction (B). Reaction (C) only occurs when reaction (A) and (B) are suppressed, as InSe forms faster than In_2Se_3 .

Finally reaction (D), the formation of $\text{CuIn}_{1-x}\text{Ga}_x\text{Se}_2$ only starts when reaction (B) has already begun and solely by interdiffusion of CuGaSe_2 into CuInSe_2 . CuGaSe_2 is formed at higher temperatures (673 K) and crosses directly over into interdiffusion of CuGaSe_2 into CuInSe_2 *via* reaction (D).

The formation reaction of $\text{CuIn}_{1-x}\text{Ga}_x\text{Se}_2$ is favorable because the position of the Se^{2-} anions in their anion sublattice of the chalcopyrite unit cell can remain unchanged as the structure equals a cubic anion and cation sublattice. A (re)arrangement of the In^{3+} and Ga^{3+} cations occurs relatively easy as their cation radii are much smaller than the anion radius of Se^{2-} .^[5]

NC synthesis approaches commonly differ significantly from solid state reactions as NC materials feature uniquely altered properties (see 2.2). CI(G)S NC syntheses in this work are based on one-pot and modified "hot injection" approaches as it proves to be extremely difficult to synthesize the binary NC compounds copper selenide, indium selenide and gallium selenide for combination of the materials in satisfying quality.

The investigated syntheses lead to the assumption that the formation mechanism of CIS NCs follows the solid state reaction mechanism *via* (A) and (B) described above. For CIGS NCs the interdiffusion reaction (D) is assumed as NC products exhibit a relatively low but reproducible gallium content.^[5]

Three different types of chalcopyrite NCs are investigated:

- Trigonal pyramidal CuInSe_2
- Elongated CuInSe_2
- $\text{CuIn}_{1-x}\text{Ga}_x\text{Se}_2$

Trigonal pyramidal CuInSe_2 NCs are synthesized by a modified hot injection method (see 2.2 and 5.1.1) whereas elongated CuInSe_2 and $\text{CuIn}_{1-x}\text{Ga}_x\text{Se}_2$ NCs are formed by one-pot syntheses.

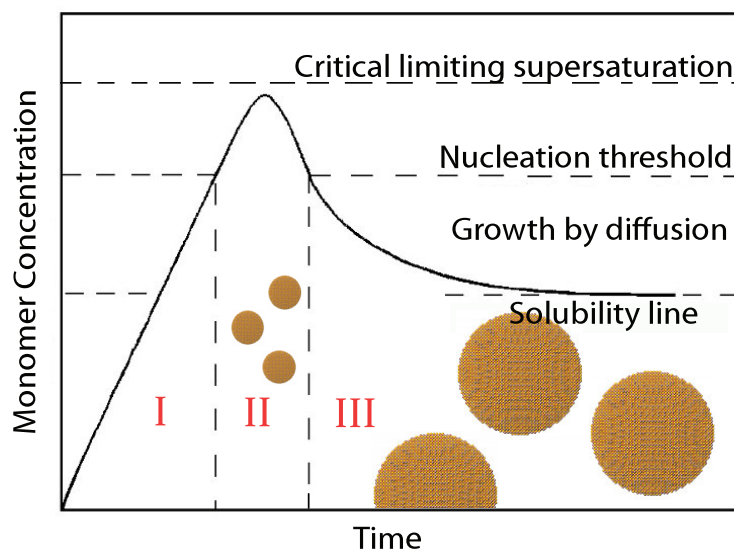


Figure 2.3: LaMer diagram for nucleation and growth, adapted from LaMer and Dinegar.^[9]

2.2 Nucleation and Growth in Nanocrystals

In 1950 LaMer and Dinegar presented a model for the formation of monodisperse sulfur hydrosols which is still widely used to generally describe nucleation and growth processes in three stages for colloidal systems pictured in Figure 2.3.

Metal salts (copper, indium and gallium halides in this study) are used as precursors for NC syntheses. These metal salts are reduced up to a saturation concentration in stage I (see Figure 2.3) to form so called (elemental metal) monomers in solution. This process normally takes place at high reaction temperatures and fast addition of the precursors until a critical concentration of monomers is reached and supersaturation arises in stage II. At this stage spontaneous homogeneous nucleation sets in and small nuclei are formed very rapidly in stage II. The point of nucleation thereby limits the state of supersaturation. In stage III the growth process of the formed nuclei is nurtured by the remaining monomers.^[7,8]

To obtain narrow size distributed NCs, the nucleation burst in stage II has to be kept as short as possible and separated from the growth of the formed nuclei. An effective separation of nucleation and growth is achieved by using the *hot injection* method for syntheses pioneered by Murray, Norris and Bawendi *et al.*^[10] The precursors for the monomer formation are added to the

reaction at a very fast rate to enable a short nucleation burst. Subsequently the reaction temperature is decreased to allow growth of the NCs and prevent further nucleation.

The NC reactions in this study fail to be conducted by *hot injection* methods following the classical LaMer nucleation and growth model. The investigated syntheses are mostly one-pot approaches including the complete combination of the educts to start the reaction at elevated temperatures. Nucleation and growth cannot be exactly separated by this procedure.

One crucial factor for the one-pot approach are the third main group elements indium and gallium, present in all investigated NC types. Indium and gallium exhibit a high covalent bond share in related compounds.^[11] An ionic monomer formation of indium and gallium is rather unlikely as the bare atoms and ions are chemically unstable, so that precursors for third main group elements containing syntheses often have to be strongly complexed. This leads to high temperatures to surpass the activation energy for reaction.^[12]

A distinct separation of nucleation and growth processes, as in the case of II-VI NC syntheses^[10,13,14], has so far not been achieved for third main group containing synthesis approaches.^[12]

However, in this work it is shown that it is possible to obtain narrow size distributed I-III-VI₂ and III-V NCs. The results can be explained by adapting a model very recently described by Buhro and co-workers.^[15] They characterize the fact that many NC syntheses fail to be explained solely by classical nucleation and growth processes and expand the concept by introducing *aggregative* nucleation and growth. *Aggregative* nucleation and growth means that at the beginning of the reaction very small NC cluster are formed, so called primary NCs, that in the course of the reaction aggregate, coalesce and finally recrystallize to form bigger and (often) narrow size distributed NCs. This process has been directly observed for example for metal platinum NCs by Alivisatos and co-workers in a liquid cell inside the TEM.^[16]

Furthermore Buhro and co-workers describe that *aggregative* nucleation and growth is highly dependent on the colloidal instability of the primary NCs leading to aggregation.^[15,17] The colloidal stability of the primary NCs therefore is directly dependent on the precursor concentration, reaction temperature and stabilizer/solvent that leads to their formation. As intentionally destabilizing primary NCs by varying the stabilizer and/or solvent yields changed growth conditions, one should be able to control NC syntheses. It is thereby crucial to consider that *aggregative* nucleation and growth and classical LaMer nucleation can co-exist or both occur time-shifted.^[15]

By applying the *aggregative* nucleation and growth model to the formation of $\text{CuIn}(\text{Ga})\text{Se}_2$ NCs (see 3.1, 3.2 and 3.3), one can excellently describe and explain the initial formation of smaller primary CI(G)S NCs in solution merging into the formation of bigger crystallites.^[18,19]

The formation of two-dimensional In_xSe_y nanosheets (see 3.10) can be likewise explained by the *aggregative* nucleation and growth concept. Their lateral growth is possible *via oriented attachment*, which is a form of *aggregative* growth of exceptionally small NCs (by stabilizing effects of the ligand and solvent).^[15]

The formation of GaAs NCs represents the combination of the classical LaMer model with the *aggregative* one. First, elemental gallium monomers are formed by reducing the gallium halide precursors with *n*-butyllithium. These seeds are assumed to nucleate small primary GaAs NCs which grow in a subsequent step at high temperatures to yield bigger but narrow size distributed GaAs NCs.^[12]

2.3 Application of CuInSe_2 and $\text{CuIn}_{1-x}\text{Ga}_x\text{Se}_2$ Nanocrystals in Quantum Dot Solar Cells

Size quantization effects in crystalline semiconductor materials set in when the crystallite size reaches the size of the BOHR exciton radius of the material and have been widely described, characterized and investigated in the last 30 years.^[20-23] The band gap of NC materials can be controlled and varied by changing the NC size whereby its energy increases with decreasing NC diameter. This effect leads to intriguing and useful altered properties of the semiconductor materials.

The band gap alteration in NCs can commonly be determined by absorption measurements which depict maxima for discrete excitonic transitions of numerous semiconducting NC materials.

CuInSe_2 exhibits a BOHR exciton radius of 10.6 nm.^[24,25] This means that size quantization effects in CIS should set in when NCs reach sizes around 20 nm.^[20,23] However, absorption spectra of CI(G)S NCs investigated in this work lack distinct excitonic absorption features. This phenomenon is in accordance with observations made by Zhong *et al.*^[26,27] and others^[28,29] who attribute this behavior to the existence of inherent and surface traps in the NCs blurring absorption maxima.^[18] Nevertheless, the slightly increased band gap in CI(G)S NCs is determined by applying the direct band gap method of Tauc *et al.*^[30] (see 3.2 and 3.3).

One crucial problem in easily processing CuInSe_2 and $\text{CuIn}_{1-x}\text{Ga}_x\text{Se}_2$ for solar cell applications is their relatively complicated crystal system (see 2.1). Commonly used reaction pathways for thin films involve evaporation of the reaction components at high vacuum and selenization methods which are expensive, complex and hazardous and do not always assure a distinct stoichiometry of the materials.^[31-33]

Furthermore, usually high reaction temperatures limit the use of substrates for depositing the materials. Especially in the sector of flexible applications this fact seriously confines the use of gas phase reaction processed CuIn(Ga)Se_2 .

An alternative way to control the desired stoichiometry of CI(G)S and avoid hazardous reactions from the gas phase are wet-chemical synthesis approaches for CI(G)S NCs. Colloidal CI(G)S NCs from solution have distinct favorable properties compared to solid state materials:

1. For CI(G)S NCs the tunability of the band gap resides in the range of 1.04 eV for pure CuInSe_2 and 1.68 eV for pure CuGaSe_2 by either incorporating gallium into the crystal lattice or reducing the NC di-

ameter. A combination of both factors leads to improved flexibility in processing.

2. Wet-chemically produced NCs can be easily and scalably applied onto different surfaces and flexible substrates by spin-coating, dip-coating, spray painting, ink-jet printing and roll-to-roll techniques. This offers an unprecedented freedom in the solution-processability of the materials.
3. Densely packed monolayers of NCs can exhibit a five-fold absorption enhancement per quantum dot compared to NCs in solution. This behavior can be explained by improved dipolar coupling in close monolayers and emphasizes the useful properties of NCs for solar cells.^[34]
4. The tunability of the NC band gap enables the assembly of multi-junction quantum dot solar cells. Their advantage is that they can significantly surpass the SHOCKLEY-QUEISSER limit^[2] of $\sim 33\%$ on single-junction power conversion efficiency.^[35]
5. In semiconductor NC materials the process of *Multiple Exciton Generation* (MEG) can occur. Here, a high energy photon creates multiple excitons, respectively charge carriers, instead of creating just one exciton and losing additional energy as heat.^[36-38] The effect has been used recently for highly efficient solar energy harvesting.^[39,40]

Key points (3)-(5) are promising ways of utilizing NCs and show first research level applications. In this work, points (1) and (2) are comprehensively elucidated and improved to produce CI(G)S NCs suitable and usable for these applications in the near future.

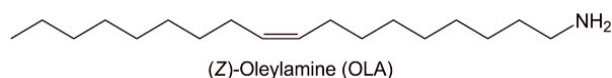


Figure 2.4: Oleylamine as initial ligand in CI(G)S NC syntheses.

2.4 Initial Ligands and Ligand Exchange

One problem that has to be addressed in wet-chemically processed NCs is the way they are stabilized. To be accessible and profitable in electronic applications like solar cells, NC materials have to be highly conductive.

However, most NCs are stabilized with organic long-chained capping molecules, so called ligands^[41], that on the one hand secure solution-processability but on the other hand prevent interparticle charge carrier transport and hence conductivity in NC films.

This general problem is addressed in this work by ligand exchanging CI(G)S NCs with a thermally degradable ligand and enhancing the interparticle communication in associated NC solids (3.8 and 3.9).

2.4.1 Initial Ligands

The initial ligand oleylamine (OLA, see Figure 2.4) used for CI(G)S NC syntheses is widely used as stabilizer in NC systems. It is liquid at room temperature, has a boiling point of ~ 350 °C and can therefore be used as stabilizer and high boiling solvent at the same time.

The long-chained organic molecule with the double bond is assumed to form metal coordinating complexes as precursors for the formation of the NCs.^[42] The amine group thereby binds to the metal clusters or primary NCs during nucleation and growth and eventually to the atoms on the surface of the NCs. The double bond of the compound helps to effectively decompose the selenium precursors to yield reactive selenium species for the crystallite formation. Oleylamine undergoes special reaction pathways with the most commonly used selenium precursor for NC syntheses in this work: selenourea ($\text{SeC}(\text{NH}_2)_2$).

The provision of reactive selenium species for the reaction with the copper, indium and gallium precursors thereby can be described by adapting a concept for the reaction of sulfur and selenium with double bonds made by Bullen *et al.*^[43]

As selenium is known to undergo vulcanization reactions very similar to sulfur, selenium species released from selenourea can react at elevated temperatures with oleylamine and form cyclic octaselenium, chain-like selenium and short selenium bridges coordinating to its double bond (see Figure 2.5).

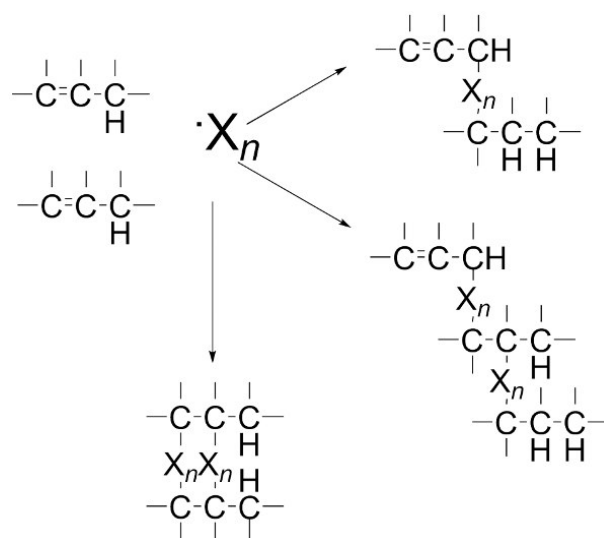


Figure 2.5: Possible vulcanization reactions of reactive selenium with monoalkenes, X_n is for selenium or sulfur with the chain length max. $n = 8$.^[43]

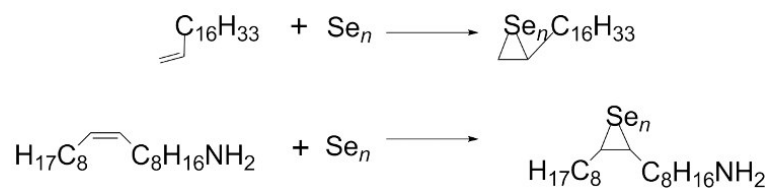


Figure 2.6: Addition of selenium species to the 1-octadecene and the oleylamine double bond.^[43]

The reaction was proven for elemental selenium coordinated to 1-octadecene and is also very reasonable for the addition to the double bond of oleylamine (see Figure 2.6). For the course of the reaction, oleylamine is used as the sole ligand. However, after the CI(G)S formation, the obtained NCs are further stabilized by the addition of *n*-Trioctylphosphin (TOP).

As TOP is known to strongly bind to selenium atoms^[44] and dangling bonds of unsaturated sulfur and selenium atoms on the NC surface^[45], it is used to additionally improve colloidal stability of the pristine CI(G)S NCs.

2.4.2 Ligand Exchange

A certain advantage of oleylamine is that it is relatively weakly bound to the NC surface, so that ligand exchange reactions can be easily performed.

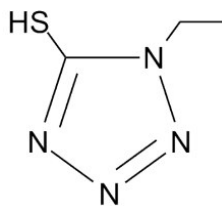


Figure 2.7: 1-Ethyl-5-thiotetrazole (ETT) as thermally degradable ligand for CI(G)S NCs.

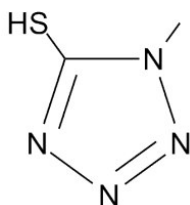


Figure 2.8: 1-Methyl-5-thiotetrazole (MTT) as thermally degradable ligand for CI(G)S NCs.

To improve the performance of CuIn(Ga)Se₂ NCs in electronic applications, they are ligand exchanged from OLA to 1-ethyl-5-thiotetrazole (ETT, see Figure 2.7). ETT has shown its suitability as thermally degradable ligand and sulfur source in the synthesis of CdS NCs.^[46] It decomposes without leaving organic residues (see 3.5) and can be synthesized according to well established literature procedures.^[47,48]

ETT is applied to CI(G)S NCs to produce virtually bare NCs from wet-chemical solution for the first time.^[18]

For comparison of the general applicability of thiotetrazole-based ligands for CI(G)S NCs, 1-methyl-5-thiotetrazole (MTT, see Figure 2.8) is likewise used for ligand exchange of the NCs. The compound is commercially available.

The third CI(G)S NC surface treatment is conducted with Meerwein's salt (Et₃OBF₄) which is known to strip oleylamine off NC surfaces and should also lead to ligand-free NCs.^[49]

The ligand exchange and the surface treatment results for CI(G)S are compared and ranked for their compatibility with efficiently enhanced electrical transport properties of the NCs (see 3.5 and 3.9).

2.5 Electrical Transport in Nanocrystal Solids

As charge carriers have to travel through interparticle distances from one NC to the next, efficient electrical transport is strongly dependent on the dielectric medium surrounding the NCs, the ligands. Most ligands are long hydrocarbon-based ones, representing significant tunneling barriers for charge carriers and resulting in poor electrical transport in these assemblies as charge carriers fail to overcome the interparticle medium.^[50]

The goal hence for NC solids is to improve the so called *Coupling Energy* β (see equation 2.1) which increases with decreasing interparticle distance, so that NCs can couple more efficiently for electrical transport.^[50] β is characterized by^[50-52]

$$\beta \approx h\Gamma \quad (2.1)$$

whereas h is the Planck's constant and Γ the tunneling rate which is described by^[50,52,53]

$$\Gamma \approx \exp\{-2(2m^* \Delta E/\hbar^2)^{\frac{1}{2}} \Delta x\} \quad (2.2)$$

where m^* is the effective mass of the charge carriers, and ΔE and Δx are the height of the tunneling barrier and the distance between two adjacent NCs.^[7,50]

From equation 2.2 one can derive that the tunneling rate drops exponentially with increasing Δx (the interparticle medium, ligand length) and is a little less dependent of the barrier height ΔE and the effective mass m^* . This means that by reducing the interparticle medium, respectively distance, stronger coupling and associated improved electrical transport is achieved.^[18,50,54,55]

Additionally to the *Coupling Energy* the *Coulomb Charging Energy* (E_c) is important for electrical transport. For an electron to travel between two NCs, E_c represents the additional energy required for the NC to be charged with an additional electron. E_c and the radius (r) of the NC are inversely related, this means, the smaller the NC, the higher E_c (see equation 2.3):^[50,51,56,57]

$$E_c = e^2/(4\pi\epsilon_m\epsilon_0r) \quad (2.3)$$

ϵ_0 is the vacuum permittivity, ϵ_m the dielectric constant of the NC surrounding medium and e the unit charge.

Electronic or structural disorder ($\Delta\alpha$) is the last component in the determination of the electrical transport in NC assemblies. Wet-chemically

produced NCs always show derivation from the ideal case and exhibit different NC sizes and hence energies for charge carriers to travel the NCs. The migration rate of charge carriers thereby drops with increasing disorder.^[50,52]

The goal for researchers to accomplish is the combination of an efficient and high *Coupling Energy* and *Tunneling Rate* with a small *Coulomb Charging Energy* of the NCs at a reasonable crystal size permitting size quantization effects. In an ideal case the NCs show as little electronic and structural disorder as possible.

Lastly it has to be stated, that different charge transport mechanisms in NC solids are possible, namely sequential tunneling and thermally assisted nearest-neighbor hopping.^[50] Both mechanisms can be only distinguished from each other by their differing temperature dependencies of the conductivity of the investigated NCs.^[50,58] Mentzel *et al.* thereby showed that conductivity of different semiconductor NCs capped with bulky ligands occurred *via* nearest-neighbor hopping.^[58]

The formation of tunneling barriers from bulky ligands, used in NC syntheses, represents a crucial drawback still preventing most NC species from being accessible and profitable for electronic applications.

Wet-chemical approaches on the one hand represent low-cost ways to synthesize the material but on the other hand the obtained NCs are commonly stabilized with long-chained organic capping agents that secure stability in solution and prevent aggregation. At the same time, these organic surfactant molecules inhibit electronic interparticle interactions resulting in insulating behavior of NC assemblies (see above).^[50]

There are ways to increase the conductivity in NC solids for example by using inorganic metal chalcogenide complex ligands (MCCs)^[59,60] but these involve the use of toxic and hazardous anhydrous hydrazine and are hard to apply in industrial large-scale dimensions.

Chemical treatments with 1,2-ethanedithiol^[61] and ethanethiol^[62] show that photovoltaic device efficiency and electrical transport of NC films can be enhanced but ligand exchange is performed after the deposition of the NCs confining the flexibility of device fabrication.

Further approaches like the use of thiocyanate as capping agent^[63] and Meerwein's salt^[49] for removing stabilizing amines, carboxylates and phosphonates have not yet been shown for CI(G)S NCs. Recent results in stripping ligands off of NC surfaces with $(\text{NH}_4)_2\text{S}$ ^[64] may be promising but have to show their abilities in determining the electrical transport properties of the NC materials.^[18]

In this work, electrical transport in the chalcopyrite NC system CI(G)S is investigated upon exchange from the initial oleylamine ligand shell to the

2 Background Information and Theory

thermally degradable 1-ethyl-5-thiotetrazole molecule (see 3.9). The capability of ETT as ligand and reactant for CdS NCs has been first described by Voitekovich *et al.*^[46] In this work, it is successfully implemented for the first time for CI(G)S NCs.^[18]

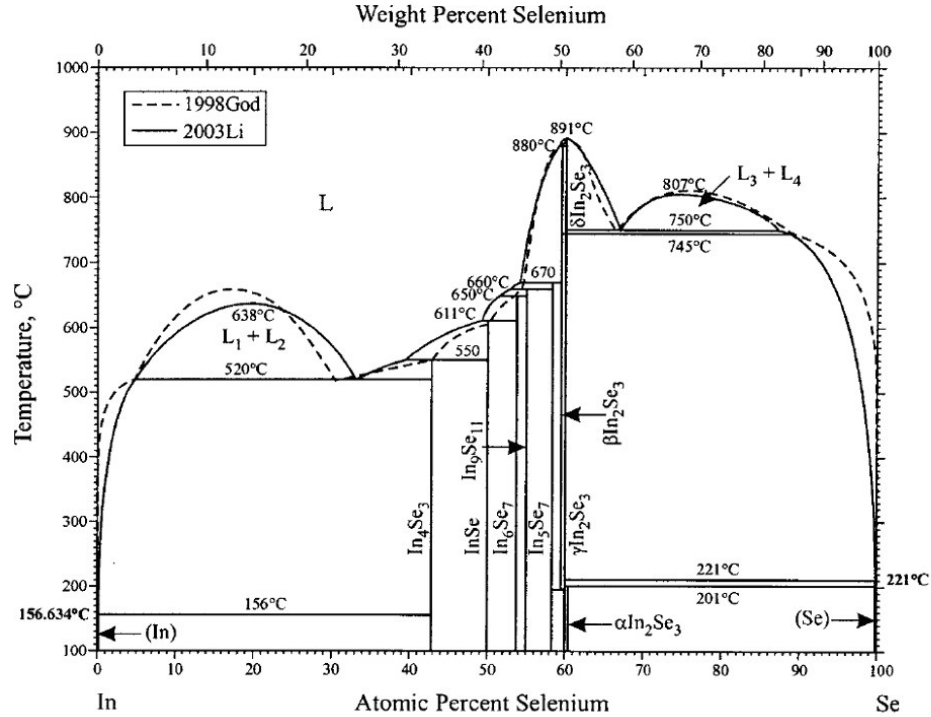


Figure 2.9: Phase diagram of numerous indium selenide phases and stoichiometries.^[74]

2.6 Indium Selenide and Assembly of 2D Indium Selenide Nanosheets

Indium selenide is an interesting semiconductor material existing in many different phases and stoichiometries due to valence electron number mismatch of the components (In^{III} and Se^{VI}).^[65]

Stoichiometries found include InSe ^[1,66], In_6Se_7 ^[1,67] and In_2Se_3 ^[1,68,69].

In_2Se_3 thereby occurs in five different phases α , β , γ , δ and κ , whereas the most stable phases are the α , β and γ phase.^[65,70–73]

Figure 2.9 depicts the complicated phase diagram of the compound.^[74]

In this work, first synthesis and characterization results for two-dimensional exceptionally thin layered In_xSe_y nanosheets are shown. The formation mechanism of the structures can be described by *aggregative* growth and associated *oriented attachment* of indium selenide to yield two-dimensional

crystalline structures when the copper component in CuInSe_2 syntheses is omitted (see 2.2).^[15]

Depending on the reaction time, the obtained nanosheets either show a hexagonal or a trigonal form. This observation is explained with a concept of Hayashi *et al.*^[75] They describe the hexagonal InSe phase to exhibit two types of growth direction known to feature different reactivity towards the incorporation of selenium into the compound.^[75]

By providing an excess of selenium, both possible growth directions of the InSe structure can be supplied adequately for reaction and the InSe structures grow hexagonal. In contrast, a decrease of selenium in reaction leads to the formation of rather trigonal InSe.

The model of Hayashi *et al.* is in accordance with the obtained results and has been adapted by other groups to describe the two-dimensional growth of indium selenide nanostructures before.^[75,76]

By further elucidating the stoichiometry and dimensions of the processed In_xSe_y nanosheets it will be possible to determine the electrical transport properties of the materials.

2.7 Gallium Arsenide

III-V semiconductor compounds, GaAs in particular, can be classified as basic materials in fabricating modern optoelectronic devices and solar cells.^[77–79] GaAs is a direct band gap material (1.42 eV at 300 K)^[80,81] showing superior electronic properties to commonly used silicon with an indirect band gap (1.12 eV at 300 K)^[80]. GaAs has a higher electron mobility allowing devices to be operated at frequencies above 250 GHz. Additionally its band gap is much closer to the optimum for reaching best conversion efficiencies at AM1.5-1 calculated to be 1.34 eV.^[2,82]

However, the use of GaAs has been restricted as there are difficulties in growing and optimizing the material. This, up to now, has made GaAs-based solar cells too expensive to be used as standard solar cell material. As well as in solid state research, colloidal GaAs and different other III-V semiconductor NCs have attracted much attention and significant technological interest in the field of NC research in the last decade because of their exceptional properties associated with their intrinsic properties and the quantum confinement (see 2.3). Due to its large exciton diameter of 19 nm, quantum confinement effects in GaAs should already occur at rather big crystallite sizes.^[83,84]

Nevertheless, difficulties in establishing applicable and feasible synthesis routes have strongly restricted the exploration and utilization of size dependent properties in nanocrystalline III-V materials up to now.^[83] The relatively high covalent character in the tetrahedral bonded atomic lattice of III-V semiconductors causes problems in effective NC synthesis. The ionic precursor reaction routes used to obtain monodisperse, well defined II-VI NCs like CdSe^[10,13,14] fail for most III-V semiconductor syntheses because of the instability of bare atoms of the third and fifth main group (see 2.2).^[12]

However, there are few methods to obtain nanocrystalline GaAs material. Non-wet-chemical ways like metal organic chemical vapour deposition (MOCVD) may result in very uniform and clean GaAs structures without crystal defects^[85,86], but highly toxic precursors like arsine and pyrophoric substances like trimethylgallium are used for this assemblies, so that many attempts have been made to find a less toxic and more cost-effective wet-chemical route for high quality NCs.

The few existing wet-chemical ways are mainly based on the dehalosylation reaction established by Wells *et al.* Herein a gallium or indium salt was reacted with highly toxic tris(trimethyl)silylarsine ((TMS)₃As) in a high boiling solvent.^[87] A modification of the dehalosylation reaction by Kher and Wells resulted in nanocrystalline GaAs structures.^[88] Olshavsky *et al.* and Uchida *et al.* synthesized GaAs NCs with (TMS)₃As in quinoline.^[84,89,90]

Butler *et al.* prepared GaAs nanocrystalline material based on the method of Wells *et al.* and discussed optical properties of the obtained material.^[91] Janik *et al.* presented a way to obtain GaAs by using a single source precursor $[\text{H}_2\text{GaAs}(\text{SiMe}_3)]_3$. Subsequent pyrolysis resulted in the formation of GaAs.^[92] Malik *et al.* showed absorption measurements of GaAs NCs synthesized from GaCl_3 and $\text{As}(\text{NMe}_2)_3$.^[93] GaAs NCs obtained by the described routes lack monodispersity and crystallinity.

With a special eye on the reactivity of the third main group element of III-V compounds, tailored III-V NCs are obtained by applying a general synthesis approach.

This work has been carried out in collaboration with Dr. Tim Strupeit who first discovered and described the GaAs synthesis in his thesis.^[94] Building on these results, I continued and elaborated the work which resulted in a joined publication in *Chemistry of Materials*.^[12]

A simple solution-processed synthesis route for GaAs NCs with narrow size distribution and high crystallinity using wet-chemical methods and commercially available inexpensive precursors with reduced toxicity is presented. The reaction pathway can be described in three steps, starting with a transmetalation reaction between the gallium(III) halide precursor GaCl_3 and the reduction agent *n*-butyllithium. At elevated temperatures, elemental gallium is released in this process and enables the formation of GaAs NCs with magnesium arsenide (Mg_3As_2) as arsenic source.^[12]

A variety of different III-V semiconductor NCs including GaAs, InP, InAs and GaP are obtained using this transmetalation reaction pathway.

3 Results and Discussion

This chapter includes the synthesis, characterization and improvement of the three chalcopyrite NC types chosen for investigation by synthesis variations.

First, the consecutive progress of $\text{CuIn}(\text{Ga})\text{Se}_2$ NCs suitable for ligand exchange in terms of precursor choice, size distribution and crystallinity is described.

Second, the successful ligand exchange and functionalization of $\text{CI}(\text{G})\text{S}$ NCs with different ligands, mainly 1-ethyl-5-thiotetrazole, is proven by comprehensive analysis of the ligand exchange process. This includes *Attenuated Total Reflectance Fourier Transformation Infrared Spectroscopy*, *Thermogravimetric Analysis*, *X-ray Photoelectron Spectroscopy* and *Small Angle X-ray Scattering* measurements.

The readily feasible thermolysis of the applied thiotetrazole-based ligands for the first time leads to the formation of virtually bare surfaced chalcopyrite NCs.

In-situ X-ray Diffraction and *in-situ Transmission Electron Microscopy* heating experiments emphasize the full benefit of the ligand-free $\text{CI}(\text{G})\text{S}$ NCs that can be sintered at moderate temperatures without altering the chalcopyrite crystal phase and stoichiometry of the material and yielding crystalline quasi-solid state assemblies.

Third, densely packed NC films of the ligand exchanged $\text{CI}(\text{G})\text{S}$ NCs are produced and the electrical transport properties and conductivity of 1-ethyl-5-thiotetrazole and 1-methyl-5-thiotetrazole stabilized NCs are specified prior to and after thermolysis of the particular ligand.

These conductivities are then related to electrical transport properties determined exemplarily for oleylamine stabilized $\text{CI}(\text{G})\text{S}$ NCs. Conductivity measurements reveal that formerly 1-ethyl-5-thiotetrazole and 1-methyl-5-thiotetrazole stabilized NC films after thermolysis of the ligand exhibit significant enhanced electrical transport compared to oleylamine stabilized NC films. Additionally, oleylamine stabilized NCs feature undesirable carbonization effects.

In the further course of the chapter the formation of two-dimensional In_xSe_y nanosheets is discussed which are obtained by varying the reaction conditions for $\text{CI}(\text{G})\text{S}$ syntheses. The formation of In_xSe_y nanosheets of-

3 Results and Discussion

fers insights into *aggregative* nucleation and growth and *oriented attachment* processes.

The chapter closes with the successful general synthesis approach for narrow size distributed GaAs and associated III-V semiconductor NCs which has not been possible before.

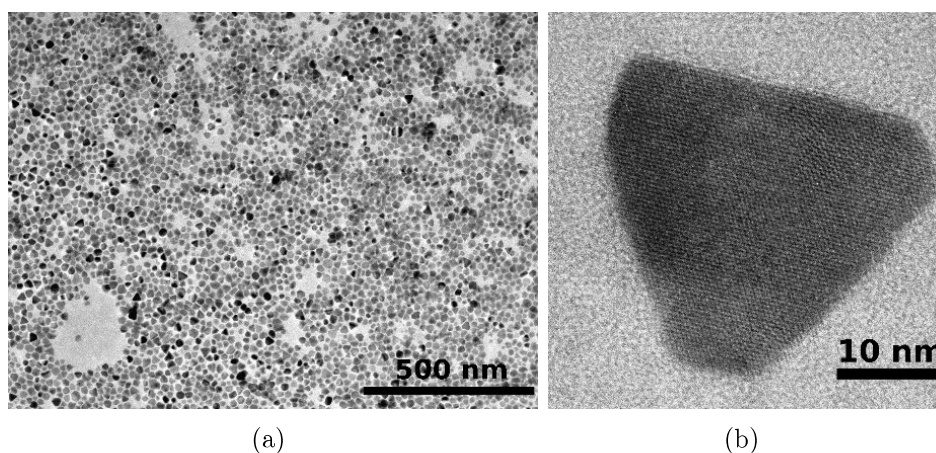


Figure 3.1: A typical NC synthesis result for trigonal pyramidal CIS with (a) an overview and (b) a single CIS NC.

3.1 Trigonal pyramidal CuInSe_2

Trigonal pyramidal CIS synthesized according to Koo *et al.*^[95] exhibit a broad size distribution of 19 nm (average longest edge length, ± 6 nm, see Figure 3.1 and 3.3b for size histogram of the NCs). Trigonal pyramidal CIS are initially capped with oleylamine assuring their colloidal stability but leading to etching of the NCs within a short period of time.^[95] Figure 3.2 shows the NCs' associated XRD pattern with vertical red lines indicating the corresponding solid state tetragonal CuInSe_2 reflexes (JCPDS #00-40-1487). Figure 3.3a shows a Vis-NIR absorption spectrum of trigonal pyramidal CIS without distinct excitonic transition features. This absence can be explained by intrinsic defects in the tetragonal distorted chalcopyrite crystal structure and surface originating trap states in the CIS NCs.^[18,26-29]

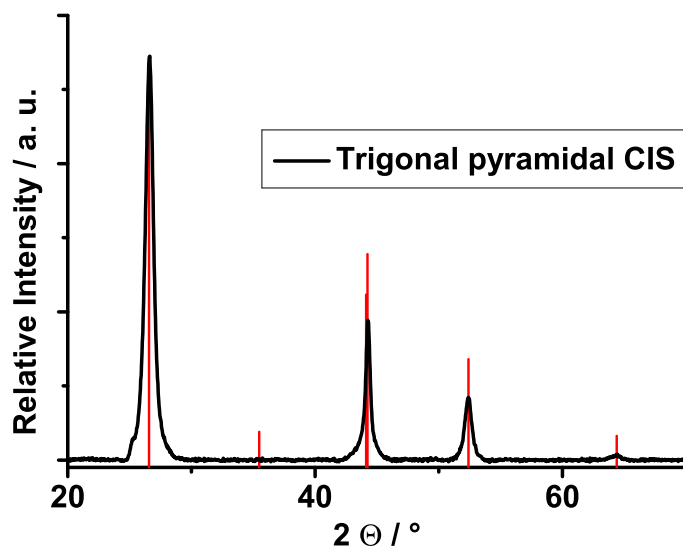


Figure 3.2: XRD pattern of trigonal pyramidal CIS NCs with the associated CuInSe_2 reference (JCPDS #00-40-1487).

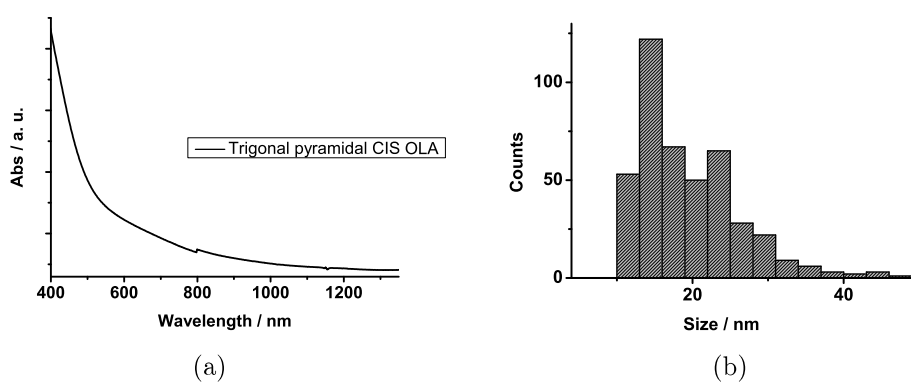


Figure 3.3: (a) Vis-NIR absorption spectrum of trigonal pyramidal NCs and (b) associated size distribution histogram.

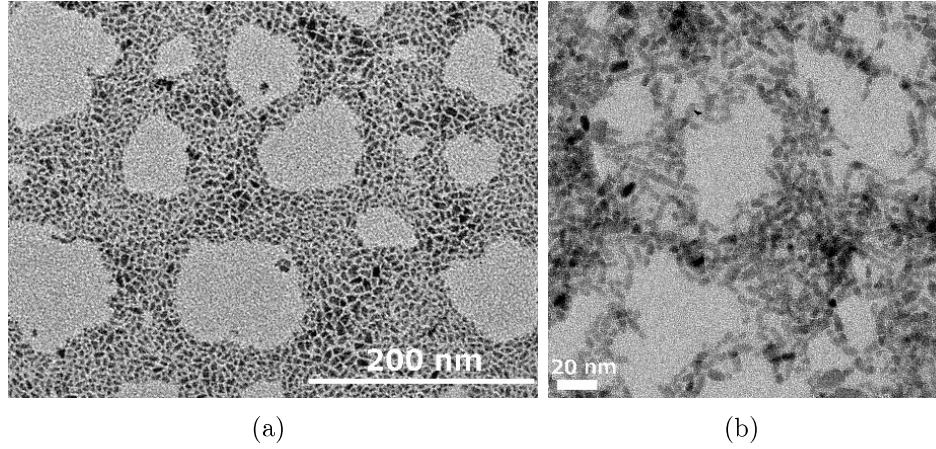


Figure 3.4: (a) Elongated CIS NC synthesis overview with (b) high resolution image of CIS NCs.

3.2 Elongated CuInSe₂

Elongated CIS NCs with a small size distribution are obtained by varying a synthesis method of Panthani *et al.*^[19] Elemental selenium as precursor is replaced by more reactive selenourea (see 3.4.1). With this slight synthesis variation the reaction time is reduced from four hours to one hour and the uniformity of the NCs is increased (see Figure 3.4 for TEM images and Figure 3.12 on page 35 for comparison). The NCs have a mean size of 7 nm (± 2 nm) (see Figure 3.5b) and are slightly elongated.

XRD patterns of elongated CIS NCs show the chalcopyrite crystal phase with slightly broadened reflexes compared to trigonal pyramidal CIS XRD patterns (see Figure 3.5a).

Generally, constructive interference of incident X-rays with lattice planes of crystals results in observable diffraction reflexes under a specific angle (θ) if BRAGG's law is valid. This is only the case, when the path difference of X-rays interfering with crystal lattice planes (with spacing d), is a multiple integer of the X-rays' wavelength (see BRAGG equation 3.1):^[96]

$$n \cdot \lambda = 2d \cdot \sin \theta \quad (3.1)$$

where n is an integer, λ is the wavelength of incident X-rays, d is the spacing of the atomic lattice planes and θ is the angle between the incident X-ray and the lattice plane normal.

A NC powder XRD sample contains a statistical number of NC lattice planes contributing to the detected reflex pattern under BRAGG conditions.

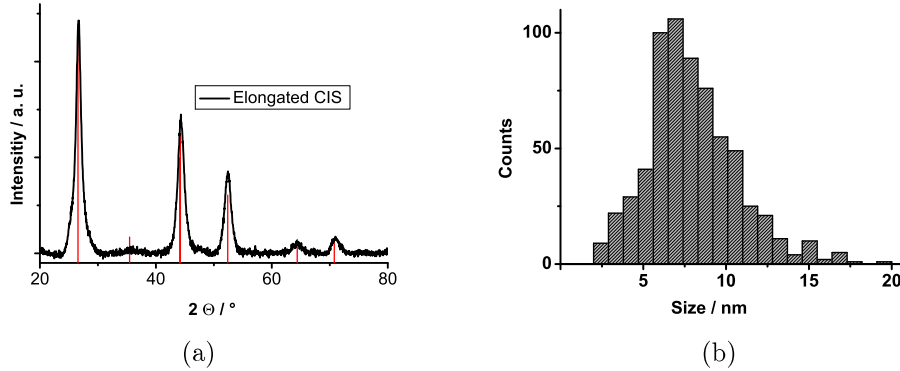


Figure 3.5: (a) XRD of elongated CIS NCs, vertical red lines indicate the CuInSe₂ reference (JCPDS #00-40-1487) and (b) size distribution histogram of the NCs.

Amongst other possible origins like crystal lattice stress/strain, broadening of reflex patterns in NC samples is often caused by the limited dimensions of the crystalline domains.

Broadening of the reflexes of elongated CIS NC's XRD in comparison with trigonal pyramidal CIS NC's reflexes in particular occurs, as by stepwise decrease of the NC size, the number of NC lattice planes, perfectly meeting the BRAGG conditions decreases as well. With fewer atoms and more small atomic imperfections contributing to the XRD pattern, the elongated CIS NC's diffractogram is composed of the averagely broadened reflex value.

Absorption spectra of elongated CIS NCs exhibit a shoulder in the measurement curve at 932 nm. By using the direct band gap method,^[30] the energy of the band gap is plotted against the square of the absorbance α^2 . The tangent applied to the function and extrapolated to the x-axis is used to estimate a band gap of 1.3 eV for elongated CIS NCs (see Figure 3.6b). This value is blue-shifted compared to 1.0 eV for bulk CuInSe₂ and indicates quantum confinement.

However, it has to be noted that the band gaps obtained by the Tauc-plot are to be understood only as approximations as the size distribution of the CI(G)S NCs and the application of tangents to the obtained curves lead to possible deviations of band gap values.

Elongated CIS NCs are compared with trigonal pyramidal CIS to investigate the possible influence of quantum confinement effects on the electrical transport properties of the CuInSe₂ materials. Furthermore, the effect of

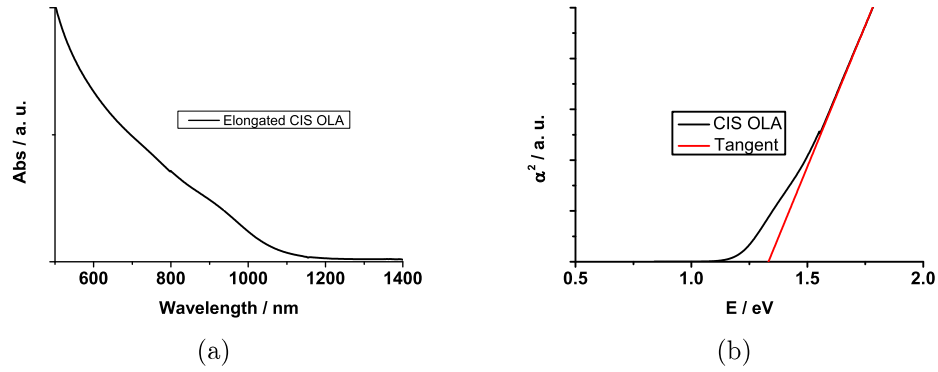


Figure 3.6: (a) Vis-NIR absorption spectrum of elongated CIS with a slight shoulder at 932 nm and (b) a Tauc-plot approximated band gap of 1.3 eV.

different CIS NC sizes on the ligand exchange behavior and processability of the NCs is determined.

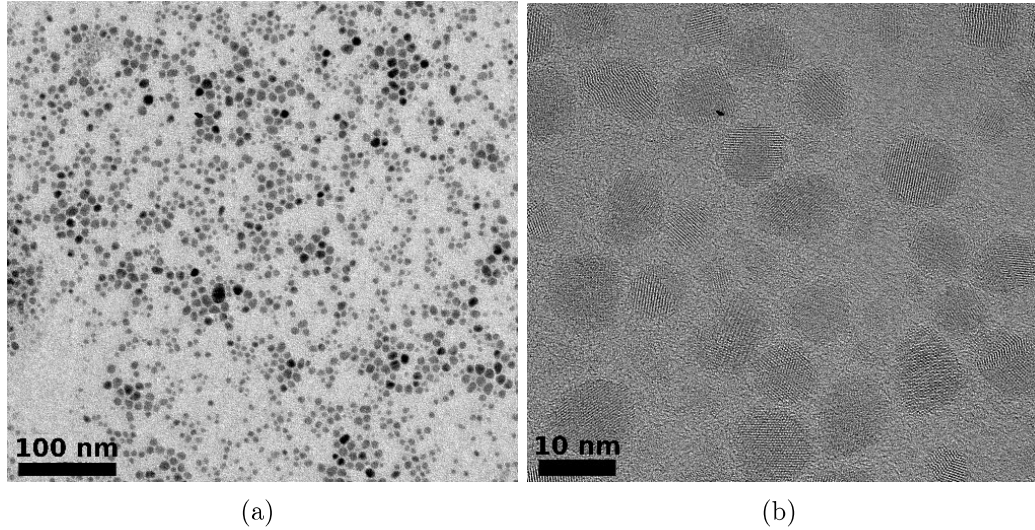


Figure 3.7: (a) A typical CIGS NC synthesis overview and (b) high resolution TEM images of CIGS NCs.

3.3 $\text{CuIn}_{1-x}\text{Ga}_x\text{Se}_2$ NCs

$\text{CuIn}_{1-x}\text{Ga}_x\text{Se}_2$ NCs are synthesized according to a slightly varied reaction procedure of Panthani *et al.*^[19] As described in 2.1, the formation of CI(G)S NCs occurs *via* interdiffusion of the ternary compounds CuInSe_2 and CuGaSe_2 . The formation of CuGaSe_2 proceeds slower than the formation of CuInSe_2 (as the CuGaSe_2 reaction starts from Ga_2Se_3 , exhibiting slower reaction kinetics than the formation of InSe for CuInSe_2) and the interdiffusion of the two ternary compounds lacks entirety.

The size of the obtained NCs is uniform with a mean diameter of 6 nm (± 1 nm) (see Figure 3.7 for TEM images and 3.8b for histogram). XRD patterns exhibit a $\text{CuIn}_{1-x}\text{Ga}_x\text{Se}_2$ composition close to the stoichiometry $\text{CuIn}_{0.75}\text{Ga}_{0.25}\text{Se}_2$ described by Hergert *et al.* (see Figure 3.8a).^[1,5,6]

Absorption spectra lack an excitonic transition shoulder like described for CIS NCs in 3.2. By applying the direct band gap method, CIGS NC's band gap is initially approximated to ~ 1.3 eV (see Figure 3.9b).

Energy Dispersive Spectroscopy (EDS) of two typical NC batches exhibits a reproducible gallium content between 3.42 and 13.83 atom percent in CI(G)S NCs (see Figure 3.10 respectively 3.11 and tables 3.1 and 3.2).

The CI(G)S NC synthesis results show that reproducible incorporation of high gallium amounts is a critical issue in wet-chemical NC syntheses.

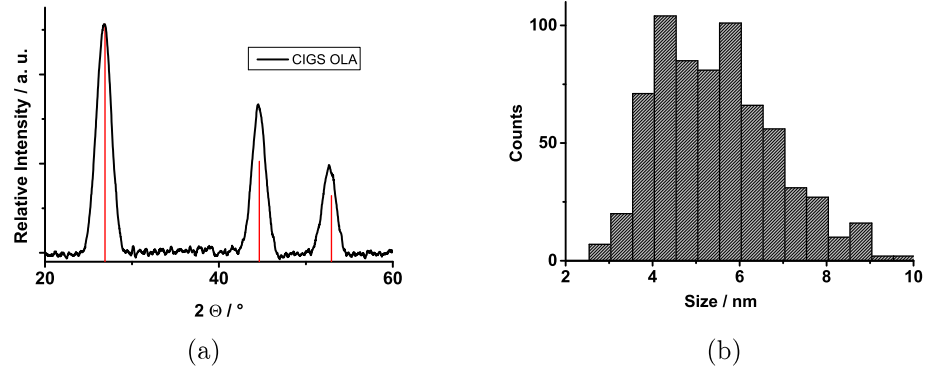


Figure 3.8: (a) XRD of CIGS 2 OLA NCs, vertical red lines indicate the $\text{CuIn}_{0.75}\text{Ga}_{0.25}\text{Se}_2$ reference (JCPDS # 00-035-1102) as closest match and (b) a size distribution histogram of CIGS 1 OLA NCs.

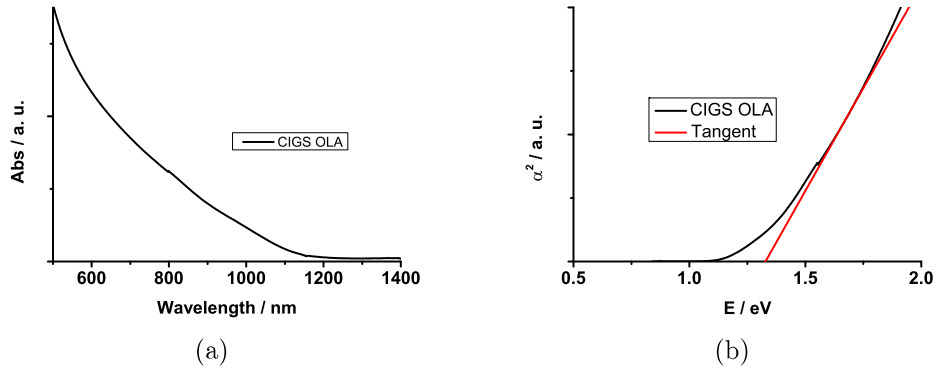


Figure 3.9: (a) Vis-NIR absorption spectrum of CIGS NCs with (b) an estimated direct band gap of ~ 1.3 eV.

CIGS 1 OLA		
Element	Atom%	Error
Cu K*	15.63	0.92
Ga L*	3.42	5.23
Se (Ref.) L*	58.05	0.29
In L*	22.90	0.54

Table 3.1: EDS of CIGS NCs in atom%.

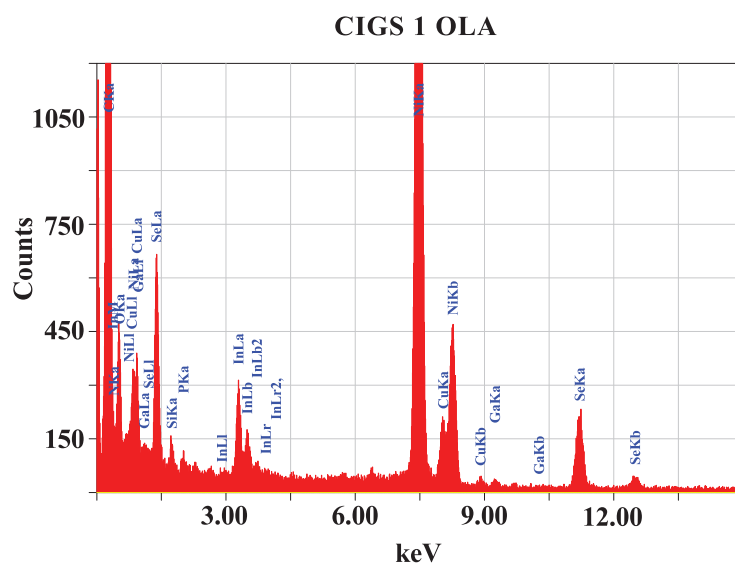


Figure 3.10: EDS of CIGS NCs containing 3.42 atom percent gallium.

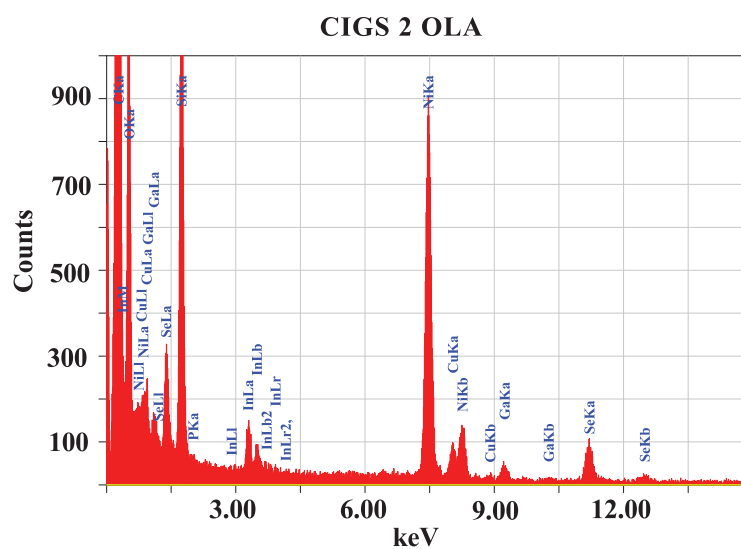


Figure 3.11: EDS of CIGS NCs containing 13.83 atom percent gallium.

CIGS 2 OLA		
Element	Atom%	Error
Cu K*	16.16	2.54
Ga L*	13.83	3.69
Se (Ref.) L*	47.65	1.01
In L*	22.35	1.58

Table 3.2: EDS of CIGS NCs in atom%.

However, the obtained CI(G)S NCs exhibit quantum confinement effects with an increased estimated band gap of ~ 1.3 eV. This value is higher than the value for common thin film $\text{CuIn}_{1-x}\text{Ga}_x\text{Se}_2$ solar cells with a gallium ratio of ~ 7 % and a band gap of ~ 1.15 eV.^[1]

The three processed chalcopyrite NC types are used to compare their suitability for forming solution-processed, ligand-free NC solids with enhanced electrical transport properties.

3.4 Choice of Precursors

Different results obtained throughout the course of this study show that the reactivity of the precursors is crucial for a reaction to yield crystalline and narrow size distributed NC products. Third main group components in CI(G)S NCs have to be carefully adjusted in reactivity to the selenium precursor as they exhibit a high degree of covalency in chemical bonds which has to be considered when choosing possible precursors (see 2.2).^[11,12]

In a successful synthesis, the reactivity of the selenium precursors is empirically adapted to indium and gallium halides used as precursors.

3.4.1 Selenourea

The syntheses described in 3.1, 3.2 and 3.3 are conducted with selenourea as precursor and yield the best and most reliable results for the investigated reactions.

The reactivity of selenourea on the one hand is high enough to allow for a controlled reaction with the indium and gallium precursors but on the other hand the compound is chemically stable enough to enable moderate reaction conditions. Selenourea features complete solubility in OLA at temperatures between 205 and 215 °C leading to a high transformation rate of the compound in reactions. However, due to its toxicity selenourea is handled with care (see 5.1.1, 5.1.2, 5.1.3 and 5.7).

Selenourea is applied exclusively for the formation of CI(G)S NCs used for ligand exchange and electrical transport measurements.

3.4.2 Selenium

Attempts with elemental selenium as precursor generally require longer reaction times and yield less uniform NCs (see Figure 3.12). Selenium is soluble in oleylamine at higher temperatures (>200 °C) but its transformation rate for NC reactions is significantly lower compared to reactions with selenourea.

CI(G)S NCs synthesized with elemental selenium as precursor are therefore excluded from ligand exchange reactions and electrical transport measurements.

3.4.3 Bis(trimethylsilyl)selenide

Bis(trimethylsilyl)selenide ((TMS)₂Se) is a highly reactive selenium precursor. Following a dehalosilylation approach first described by Wells *et al.*^[87] (TMS)₂Se is used in CIS NC syntheses with indium(III) chloride and Cu(I)

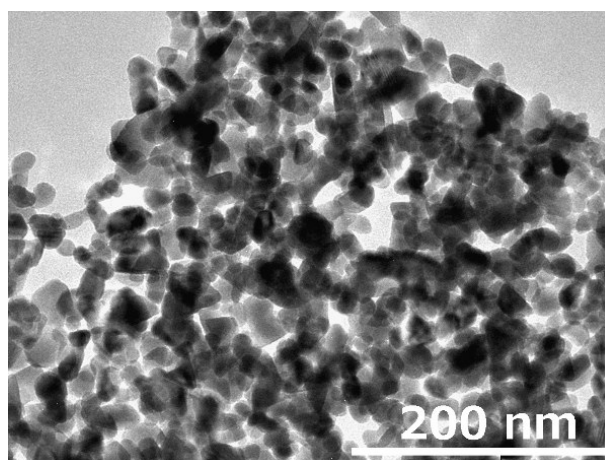


Figure 3.12: A CIS NC synthesis result with elemental selenium as precursor.

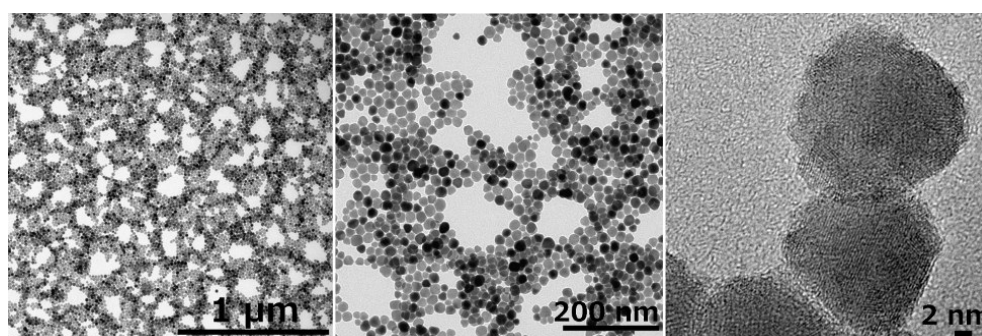


Figure 3.13: CuInSe_2 NCs obtained with $(\text{TMS})_2\text{Se}$ as precursor.

acetate as reactants. Its transformation rate for CIS NC syntheses is exceptionally high compared with the transformation rate of selenourea.

Due to its high toxicity, moisture sensitivity and volatility, $(\text{TMS})_2\text{Se}$ has to be handled extremely careful under SCHLENK-conditions or working inside a nitrogen filled glovebox.

Figure 3.13 depicts $(\text{TMS})_2\text{Se}$ -based CIS NCs. The obtained particles exhibit uniform sizes of ~ 22 nm and feature the same chalcopyrite crystal structure as trigonal pyramidal and elongated CIS (see Figure 3.14 for XRD with narrow reflexes).

To obtain statistical data for this work, many CI(G)S NC syntheses were carried out and prepared for ligand exchange and electrical transport measurements. The practicability of $(\text{TMS})_2\text{Se}$ as selenium precursor is limited by its high toxicity and associated safety precautions. Furthermore, the price

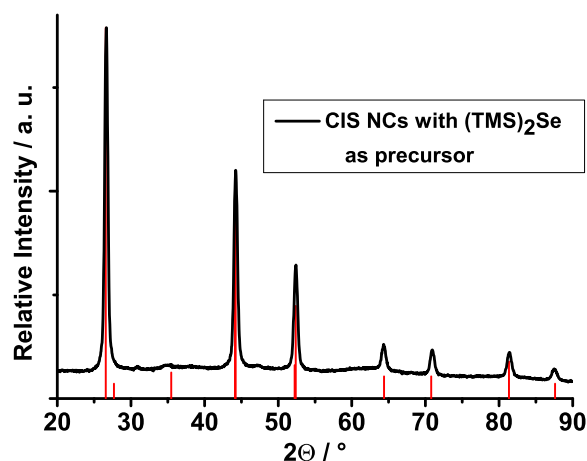


Figure 3.14: XRD pattern of CIS NCs obtained with $(\text{TMS})_2\text{Se}$ as precursor with red lines indicating the CuInSe_2 reference (JCPDS #00-40-1487).

of the compound is significantly higher than the price of selenourea which represents a better precursor for the CI(G)S NCs investigated.

However, when planning to synthesize novel chalcopyrite NCs in terms of NC morphology (e.g. exceptionally big as well as exceptionally small NCs) $(\text{TMS})_2\text{Se}$ represents a valuable precursor.

3.4.4 Copper Precursors

Copper(I) acetate and copper(I) chloride are used as copper precursors. The compounds have shown to be reactive in the formation of $\text{CuIn}(\text{Ga})\text{Se}_2$ NCs with Cu^+ stoichiometry. XPS measurements show that Cu^+ in obtained CuInSe_2 retains its oxidation state and is not oxidized to Cu^{2+} (see 3.7).

3.4.5 Indium and Gallium Precursors

Indium(III) precursors other than indium(III) halides lack the formation of $\text{CuIn}(\text{Ga})\text{Se}_2$ or In_xSe_y NCs. The use of indium(III) acetate and indium(III) acetylacetonate in combination with selenium as precursor leads to the formation of indium oxide NCs and structures.

Indium(III) chloride is used as sole indium(III) precursor in this work as it has shown its suitability for third main group containing NC syntheses in previous studies.^[12]

For the formation of CIGS NCs, gallium(III) iodide is chosen as gallium precursor. The formation rate of Ga_2Se_3 occurring during reaction is smaller than the formation rate of InSe (see 2.1)^[5]. In good correlation with the *Hard and Soft Acids and Bases* (HSAB) principle introduced by Pearson, the leaving group ability of the indium(III) and gallium(III) halides enhances from fluoride over chloride and bromide to iodide; the bigger the halide, the better its ability to stabilize a negative charge.^[12,97,98] This ability leads to the assumption that indium and gallium available for the CIGS NC reaction is formed the slowest from indium(III) and gallium(III) fluorides and the fastest from indium(III) and gallium(III) iodides and verifies the combination of InCl_3 and GaI_3 as precursors for CIGS NC syntheses.

By carefully combining the reactivities of the precursors, it is possible to obtain high quality CI(G)S NCs in terms of reproducibility, crystallinity and size distribution.

3.5 Ligand Exchange and Nanocrystal Surface Modification of CI(G)S

This section deals with the functionalization of the obtained CI(G)S NCs with respect to their applicability as wet-chemical "inks" for ligand-free NC solids.

Two thiotetrazole-based ligands, mainly 1-ethyl-5-thiotetrazole (ETT) and 1-methyl-5-thiotetrazole (MTT), are used for testing their stabilizing effect on CI(G)S NCs. 1-Ethyl-5-thiotetrazole is synthesized by well established literature procedures,^[47,48] whereas 1-methyl-5-thiotetrazole is commercially available.

The results described within this section show that ligand exchange with 1-ethyl-5-thiotetrazole proceeds faster and more entirely than ligand exchange with 1-methyl-5-thiotetrazole, yielding ETT stabilized NC "inks" for solution-processing and electrical transport measurements (see 3.9).

1-Methyl-5-thiotetrazole is tested to expand the applicability of thiotetrazoles as stabilizing ligands for CI(G)S in general.

The most important feature of ETT and MTT thereby is their thermal degradability at moderate temperatures. The facile thermolysis of the thiotetrazoles is tested on CI(G)S NCs, processing virtually bare NC surfaces and ligand-free NC solids.

Eventually, the solution-based ligand exchange of CI(G)S NCs with thiotetrazoles is compared to a recently described solid state surface treatment method with Meerwein's salt which is applied for the first time to CI(G)S NCs after their deposition from solution.

ETT is ranked first as ligand by virtue of its universal utility for CI(G)S NC functionalization.

3.5.1 Ligand Exchange: 1-Ethyl-5-thiotetrazole

In 2008 Voitekhovic *et al.* described the suitability of 1-R-5-thiotetrazoles for solution-phase and solventless single precursor synthesis of thiotetrazole capped CdS NCs.^[46] Here, they reacted cadmium precursors with different 1-R-5-thiotetrazoles (R = ethyl, *tert*-butyl, hexyl, 1-adamantyl, phenyl) which led to various CdS NC shapes depending on the substituent R. The single precursor approach is interesting for the purpose of this work as Voitekhovich *et al.* described 1-R-5-thiotetrazoles to undergo thermolysis at moderate temperatures, yielding CdS NCs in the solventless single precursor route from cadmium thiotetrazolate.^[46]

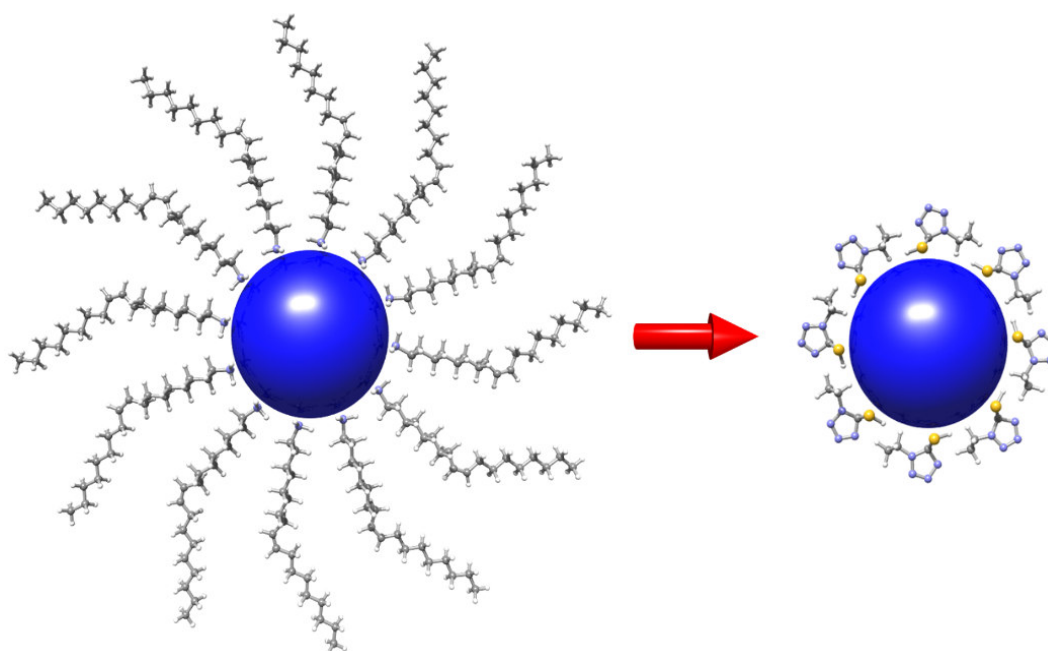


Figure 3.15: Ligand exchange scheme of oleylamine stabilized NCs with 1-ethyl-5-thiotetrazole.^[18]

Adapting and extending this approach, initially OLA capped CI(G)S NCs are ligand exchanged with 1-ethyl-5-thiotetrazole (ETT, see Figure 3.15) to obtain virtually bare surfaced CI(G)S NCs from solution. For this purpose, CI(G)S NCs are heated to the thermolysis temperature of ETT after ligand exchange.

For the ligand exchange procedure, OLA stabilized CI(G)S, dissolved in chloroform are mixed with ETT, likewise dissolved in chloroform. The ligand exchange solutions are incubated under stirring at 50 °C for 20 to 30 hours. A first hint for successful stabilization of the NCs with ETT is their "change of polarity". Whereas OLA stabilized NCs are precipitated with polar 2-propanol, CI(G)S NCs ligand exchanged with ETT are precipitated with unpolar solvents *n*-hexane or *n*-heptane.

ETT exchanged and purified NCs are redissolved in chloroform and used for characterization, thin film preparation and electrical transport measurements. CI(G)S NCs maintain their size distribution and appearance after ligand exchange with ETT (see Figure 3.16). Absorption spectra of ligand exchanged CI(G)S NCs are compared with absorption spectra of pristine NCs, thereby excluding absorption measurements of ETT exchanged trigo-

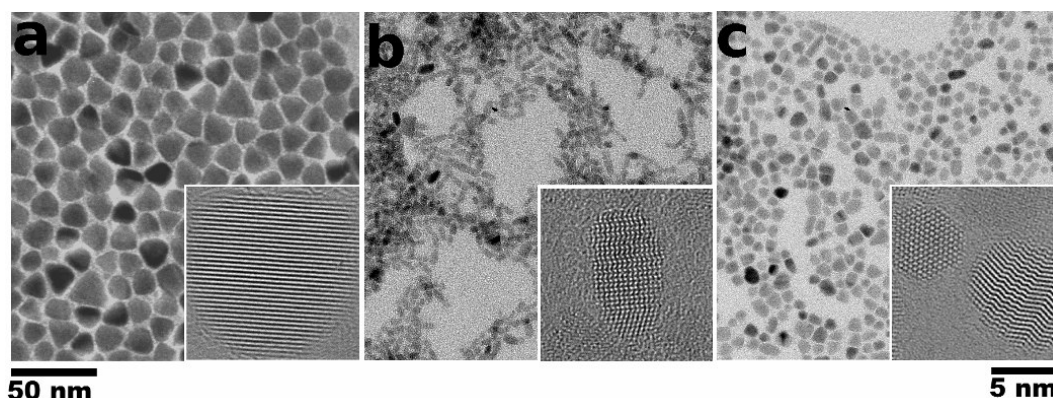


Figure 3.16: TEM images of 1-ethyl-5-thiotetrazole stabilized (a) trigonal pyramidal CIS, (b) elongated CIS and (c) CIGS and associated insets with single NCs.^[18]

nal pyramidal CIS NCs, as strong scattering made a comparative analysis impossible.

Elongated CIS and CIGS NCs' absorption stays unaltered after ligand exchange (see Figure 3.17).

3.5.1.1 Attenuated Total Reflectance Fourier Transformation Infrared Spectroscopy (ATR-FTIR)

Ligand exchange reactions are monitored by different characterization techniques including *Attenuated Total Reflectance Fourier Transformation Infrared Spectroscopy* (ATR-FTIR). Figure 3.18 exemplarily shows IR spectra of initially OLA capped and ETT exchanged trigonal pyramidal CIS NCs (Δ -CIS).

A well-known feature is the olefinic ($-\text{HC}=\text{CH}-$) stretching mode of the double bond in oleylamine at 3006 cm^{-1} .^[99] This stretching mode is observable in the OLA stabilized sample and completely absent in all ETT stabilized NC samples (see Figure 3.18 and 3.19).^[18]

Distinct asymmetric and symmetric $-\text{CH}_2$ stretching vibrations of OLA occur near 2925 and 2850 cm^{-1} in OLA capped samples (see Figure 3.18 and 3.20). After ETT exchange, the $-\text{CH}_3$ vibration of the ethyl-group in ETT at 2950 cm^{-1} emerges. The $-\text{CH}_2$ vibration at 2850 cm^{-1} is still visible with lower intensity (due to only one $-\text{CH}_2$ group in ETT, see Figure 3.18).

OLA stabilized samples show broad N-H vibrations at 3250 cm^{-1} and 1650 cm^{-1} (see Figure 3.20). These N-H vibrations are completely absent in

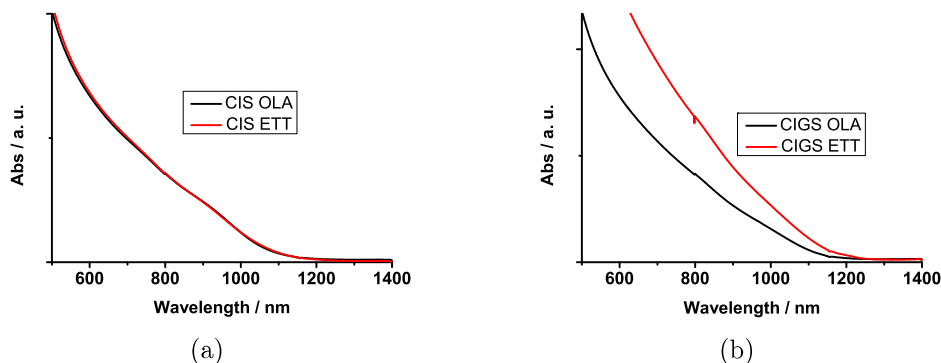


Figure 3.17: Vis-absorption spectra of OLA and ETT stabilized (a) elongated CIS with a shoulder at 932 nm prior to and unaltered after ligand exchange and (b) CIGS NCs with the same general absorption onset for OLA stabilized and ETT exchanged CIGS NCs at ~ 1050 nm ≈ 1.2 eV.

ETT capped NC samples and confirm the assumption that ligand exchange of OLA by ETT was successful (see Figure 3.19).

ETT capped NCs show the weak stretching vibration of the tetrazole rings bound to the NC surface near $1020\text{--}1160$ cm^{-1} (see Figure 3.19).^[100,101] As described by Voitekhovich *et al.* these vibrations tend to alter due to different binding possibilities of the tetrazole rings to the NC surface.^[46]

Furthermore, in ETT capped NC samples the distinct vibration of the pure and unbound ligand at 3067 cm^{-1} is absent. This might be due to reduced vibration possibility of ETT when bound to a NC surface.^[18]

3.5.1.2 Thermogravimetric Analysis (TGA)

As ETT is known to decompose at moderate temperatures^[46,48], the thermolysis of the ligand bound to NC surfaces is followed by *Thermogravimetric Analysis* (TGA).

NC samples are heated at a rate of 20 $^{\circ}\text{C}/\text{min}$ up to 550 $^{\circ}\text{C}$ under nitrogen flow and between 550 $^{\circ}\text{C}$ to 900 $^{\circ}\text{C}$ under a nitrogen/oxygen environment to remove residual carbon contents as carbon dioxide. Figure 3.21a shows the thermolysis of pure ETT with a single mass loss (94 %) at 218 $^{\circ}\text{C}$ visible in the first derivative of the measurement which is attributed to the decomposition of the ligand. Figure 3.21b shows that ETT capped CI(G)S NCs exhibit the same decomposition trend with a first mass loss attributed to ETT thermolysis between $218\text{--}255$ $^{\circ}\text{C}$. The second big mass loss occurring

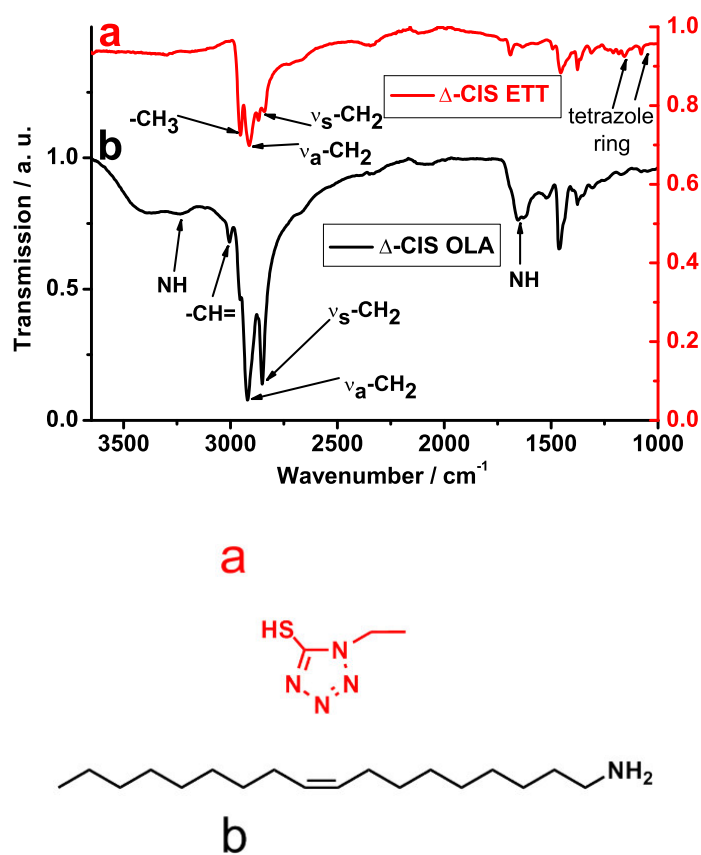


Figure 3.18: IR spectra of oleylamine stabilized and 1-ethyl-5-thiotetrazole exchanged NCs, exemplarily shown for trigonal pyramidal CIS (Δ -CIS).^[18]

3.5 Ligand Exchange and Nanocrystal Surface Modification of CI(G)S

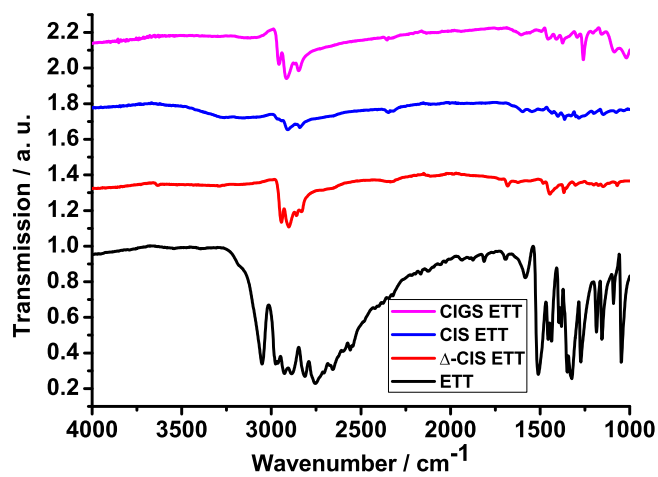


Figure 3.19: IR spectra of pure ETT and all ETT exchanged CI(G)S NC types.^[18]

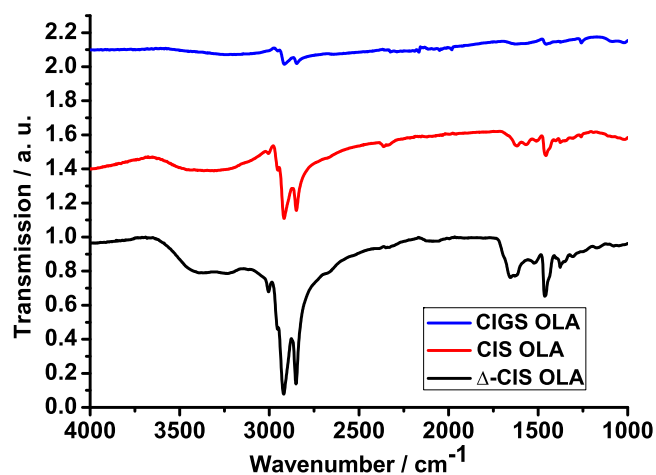


Figure 3.20: IR spectra of all OLA stabilized CI(G)S NC types.^[18]

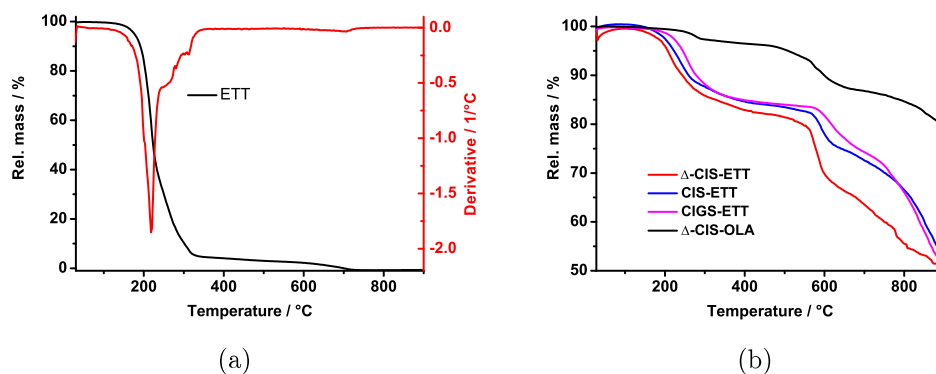


Figure 3.21: TGA of (a) pure ETT with a thermolysis temperature of 218 °C and (b) ETT stabilized CI(G)S NCs with an OLA stabilized trigonal pyramidal NC sample for comparison; all ETT capped NCs show a distinct first mass loss attributed to ETT thermolysis in the range of 218-255 °C.^[18]

at ~ 600 °C originates from selenium which evaporates from the NC sample at these temperatures. At ~ 700 °C remainders dissociate as volatile species under oxidative conditions.

When comparing the first derivatives of ETT and OLA capped CI(G)S NCs, it is visible that all ETT capped NCs undergo ligand thermolysis at lower temperatures than OLA stabilized NC samples (see Figure 3.22, 3.23 and 3.24).

Trigonal pyramidal CIS NCs' ligand associated first mass loss for ETT capped samples occurs at 218 °C, whereas OLA capped NCs show a more diffuse mass loss in the range of 278 °C.

Elongated CIS NCs capped with ETT show a first mass loss at 237 °C compared to a first mass loss at higher temperatures of 288 °C for OLA capped samples (see Figure 3.23).

CIGS NCs exhibit a thermolysis temperature of 255 °C for ETT, whereas OLA capped samples show a first mass loss in the range of ~ 265 -270 °C (see Figure 3.24).

The reason for smaller NCs to exhibit higher ETT thermolysis temperatures might be due to ETT binding stronger to the surface of smaller NCs than to the surface of bigger ones.

It has to be noted that the thermolysis temperature of ETT depends on the heating rate of the compound. To study the effect of the heating rate, the thermolysis experiment on pure ETT is repeated at 5 °C/min instead of

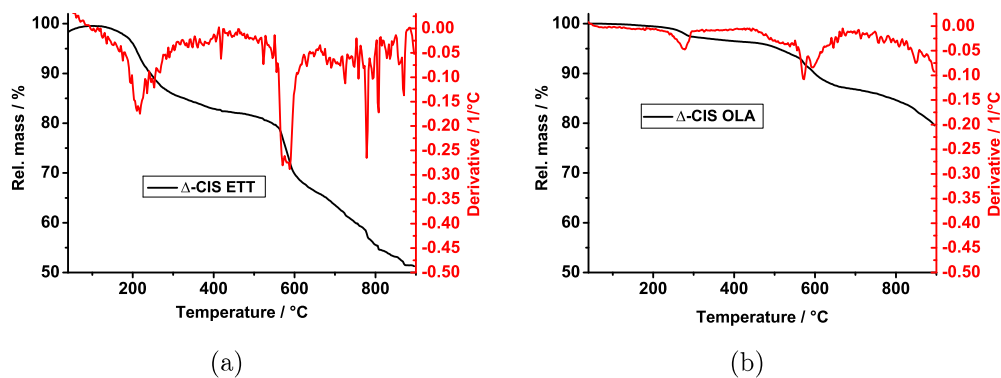


Figure 3.22: TGA of (a) ETT stabilized trigonal pyramidal CIS NCs with a thermolysis temperature of 218 °C and (b) OLA stabilized trigonal pyramidal CIS with a thermolysis temperature of \sim 278 °C.

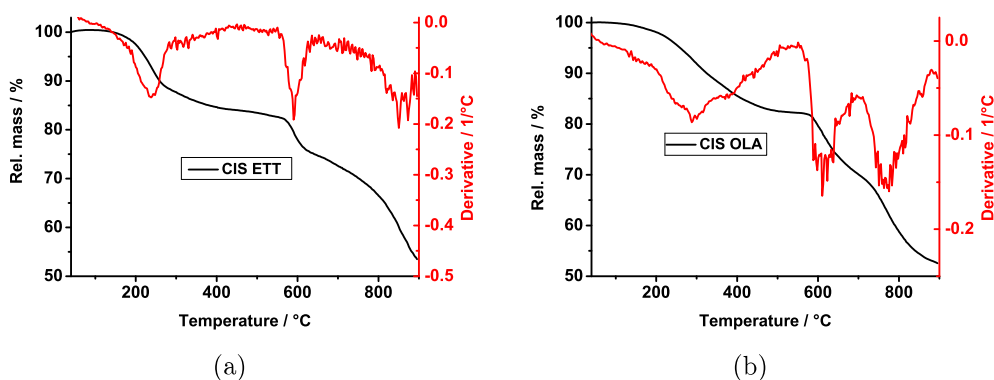


Figure 3.23: TGA of (a) ETT stabilized elongated CIS NCs with thermolysis temperature of 237 °C and (b) OLA stabilized elongated CIS with thermolysis temperature of \sim 288 °C.

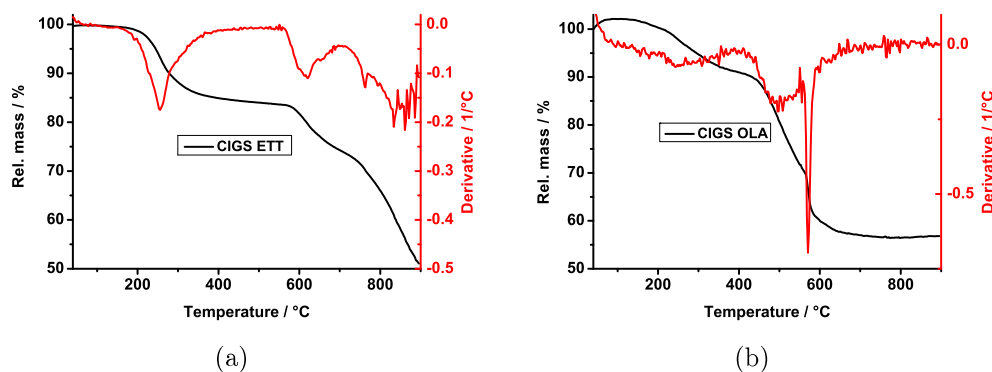


Figure 3.24: TGA of (a) ETT stabilized CIGS NCs with a thermolysis temperature of 255 °C and (b) OLA stabilized CIGS with a thermolysis temperature of \sim 265-270 °C.

20 °C/min. This results in full thermolysis of the ligand but at a reduced temperature of only 185 °C (see Figure 3.25). The decomposition of the compound hence is a kinetically controlled process.

However, to assure comparable conditions for all CuIn(Ga)Se₂ NC types investigated, only the fast heating rate of 20 °C/min is discussed.

Electron Ionization Mass Spectrometry (EI-MS) elucidates the decomposition way of ETT. With respect to a big fragment ion at m/z (%) 59 (68) [HSCN⁺] originating from thiocyanic acid, the ring fragmentation reaction for cadmium 1-ethyl-5-thiotetrazole proposed by Voitekhovich *et al.* can be confirmed.^[18,46]

An azide based decomposition of ETT is suggested as the spectrum lacks nitrogen associated mass peaks but shows fragment ions at m/z (%) 87 (8) [HSCN₃⁺] as azide and sulfur containing part of the tetrazole ring and protonated azide at m/z (%) 43 (15) [HN₃⁺].^[102,103]

Using the combined spectroscopic, thermogravimetric and spectrometric data, it is concluded that ETT decomposes virtually completely under the described conditions, leaving the surface of CI(G)S NCs organics-free with residual sulfur.^[18]

By spin-coating ETT stabilized CI(G)S NCs onto silicon substrates and subsequently thermolyzing the ligand, densely packed CI(G)S NC films are obtained which are analyzed for their electrical transport properties (see section 3.9)

Figure 3.26, 3.27 and 3.28 show ETT stabilized CI(G)S NC films after the thermolysis of the ligand.

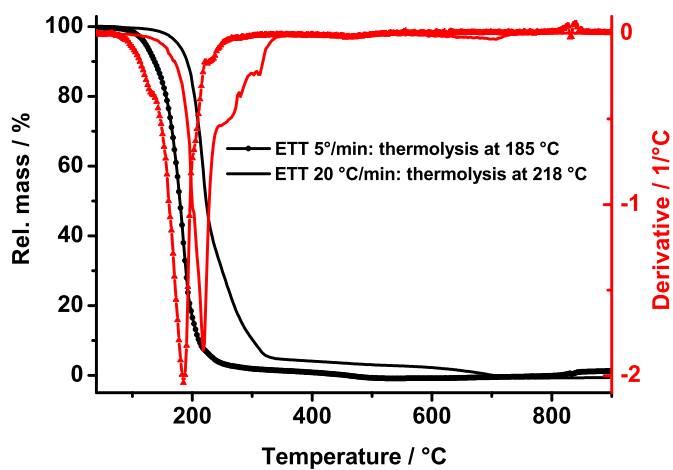


Figure 3.25: A slower heating rate of 5 °C/min leads to a reduced thermolysis temperature of ETT (185 °C) compared to heating at a rate of 20 °C/min (218 °C).

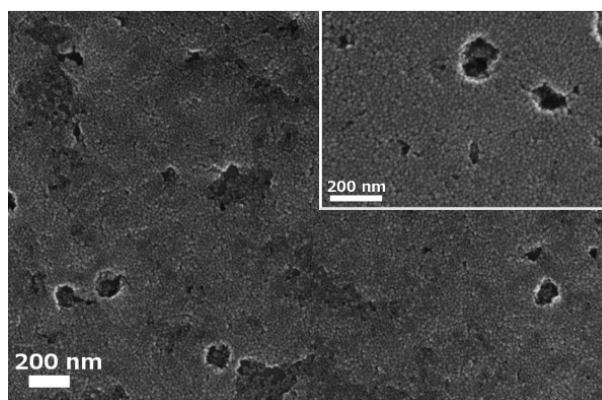


Figure 3.26: A film of trigonal pyramidal CIS NCs after thermolysis of ETT and inset with slightly higher magnification of the NCs.

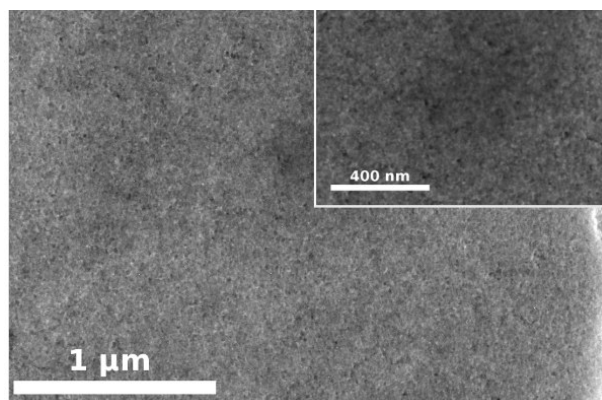


Figure 3.27: A film of elongated CIS NCs after thermolysis of ETT and inset with higher magnification of the NCs.

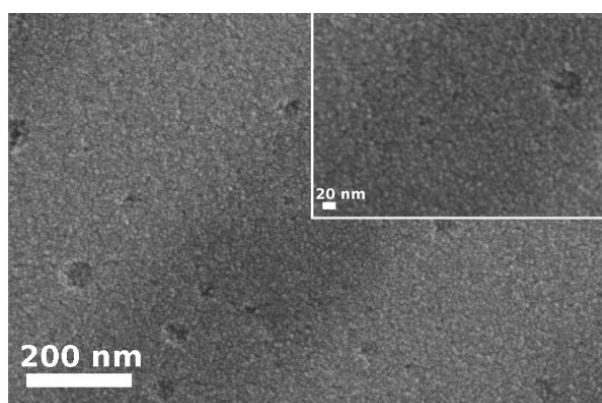


Figure 3.28: CIGS NC film after the thermolysis of ETT with an inset of higher magnified NCs.

3.5.2 Ligand Exchange: 1-Methyl-5-thiotetrazole

The commercially available and thermally degradable 1-methyl-5-thiotetrazole (MTT) is tested to expand the application of thiotetrazoles as stabilizing ligands for CI(G)S NCs. A comparison between the conductivities for ETT, OLA and MTT stabilized films is made. An emphasis is put on the influence of the slightly shorter ligand towards the electrical transport properties of the exchanged NC films (see section 3.9).

All CI(G)S NC types are ligand exchanged with MTT and their colloidal stability is compared with ETT capped NCs.

It is shown that probably due to their size (19 nm \pm 6 nm), MTT and ETT capped trigonal pyramidal NCs lack long-time stability (days to weeks).

Furthermore, trigonal pyramidal CIS NCs are known to be sensitive to etching by ligands (as described for OLA).^[95] MTT as ligand as well leads to etching of the NCs, whereas ETT capped samples show only occasionally etched NCs. Figure 3.29 depicts a TEM image of trigonal pyramidal CIS of the same batch ligand exchanged with MTT and ETT under otherwise equal conditions (CIS-MTT: 2 days after ligand exchange, CIS-ETT: 2 weeks after ligand exchange).

Elongated CIS NCs are readily ligand exchanged with MTT and lack etching effects or changes in the NC appearance.

For stabilizing CIGS NCs with MTT, a solvent change from chloroform to tetrahydrofuran (THF) is required and a high MTT excess is used. Ligand exchange solutions require longer incubation than exchange solutions with ETT (see 5.3.2).

3.5.2.1 ATR-FTIR

Figure 3.30 shows IR spectra of pure MTT and MTT exchanged CI(G)S NCs. The characteristics of the IR spectra of MTT resemble those of ETT with the exception that the vibration of the $-\text{CH}_3$ group in MTT is less distinct as in ETT as there is one $-\text{CH}_2$ group less in the compound.

The IR spectrum of MTT capped trigonal pyramidal CIS shows distinct signals between 2990-2880 cm^{-1} , in the range of $-\text{CH}_2$ and $-\text{CH}_3$ vibrations. As the spectrum exhibits even more distinct vibrations than pure MTT (see Figure 3.30) it is assumed that the MTT exchange proceeds incompletely for trigonal pyramidal CIS, leaving residual oleylamine at the NC surface which features stronger $-\text{CH}_2$ and $-\text{CH}_3$ vibrations.

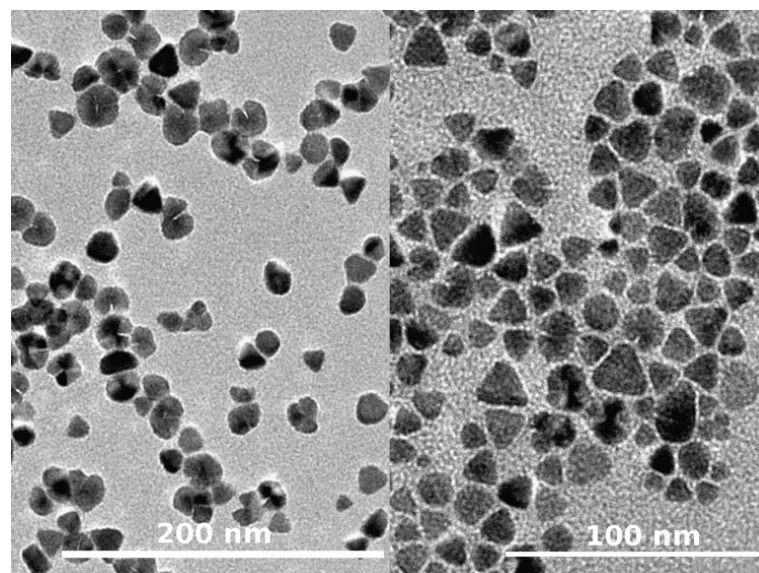


Figure 3.29: Etching of trigonal pyramidal CIS NCs after ligand exchange with MTT (left) and negligible etching effects after ligand exchange with ETT (right).

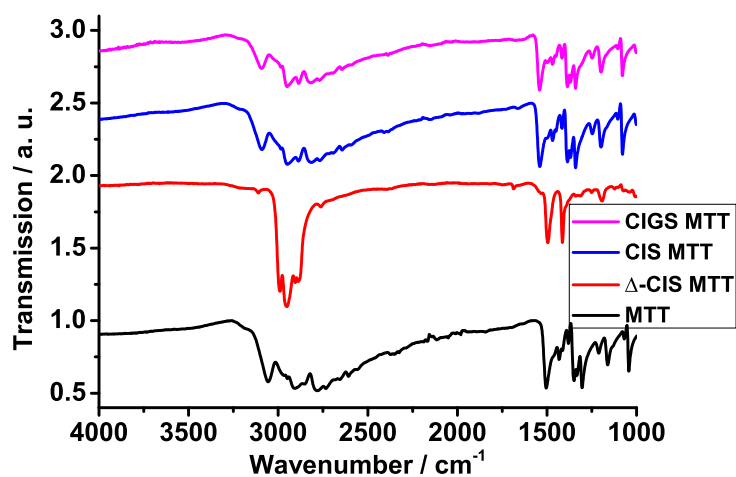


Figure 3.30: IR spectra of pure MTT and MTT ligand exchanged CI(G)S NCs with the trigonal pyramidal CIS sample showing distinct methyl vibrations.

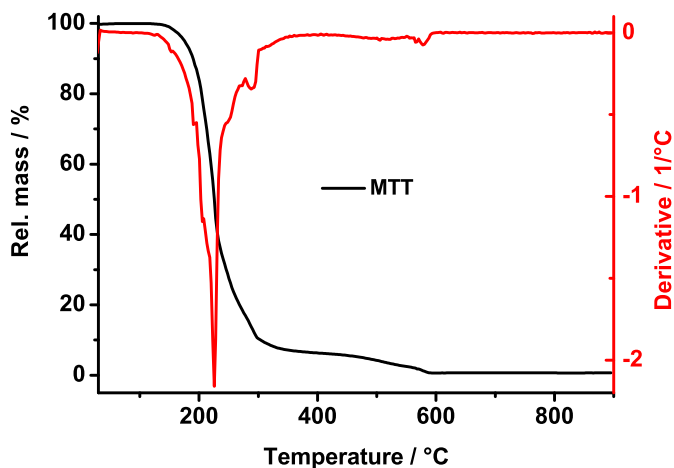


Figure 3.31: TGA of pure MTT with a thermolysis temperature of 225 °C.

3.5.2.2 TGA

To enable an even milder thermolysis treatment for ligand exchanged CI(G)S NCs, it is tested if MTT decomposes at lower temperatures than ETT.

TGA of pure MTT exhibits a likewise kinetically controlled process with a thermolysis temperature of 225 °C for the compound and an associated biggest mass loss of 91 %. (see Figure 3.31). This temperature lies in the same range and only slightly higher as the thermolysis temperature determined for pure ETT (218 °C).

When investigating the mass loss and associated derivatives of the three MTT ligand exchanged CI(G)S NC types, it turns out that at lower MTT amounts covering the NCs, the thermolysis temperature of MTT decreases compared to NCs capped with ETT.

Figure 3.32 shows the TGA of MTT and ETT capped trigonal pyramidal CIS in comparison. The first and biggest mass loss attributed to MTT thermolysis occurs at 187 °C. This is 31 °C lower than in ETT covered samples. A more diffuse mass loss in the range of 300 °C may be attributed either to the complete thermolysis of MTT or thermolysis of residual oleylamine still covering the NC surface (like detected in IR spectra, see 3.5.2.1, Figure 3.30).

It is clearly visible in TGA analyses that by using MTT as ligand, more material than can be possibly bound to the NC surface decomposes, leaving only ~6 % inorganic residues representing the remainders of the NCs (see Figure 3.32).

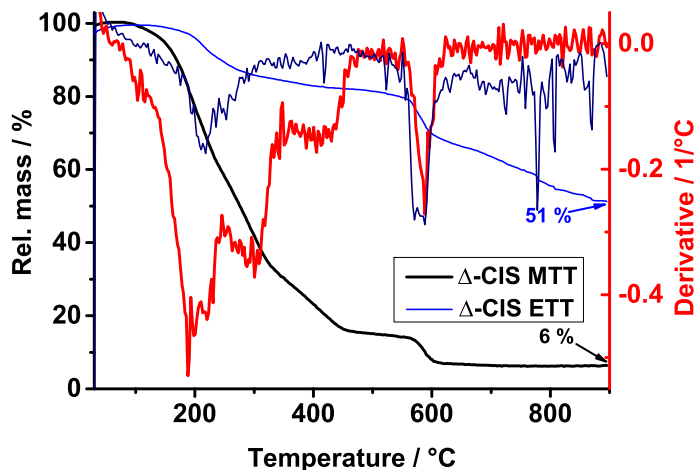


Figure 3.32: TGA of MTT and ETT stabilized trigonal pyramidal CIS in comparison with a high MTT excess dominating in trigonal pyramidal CIS exchange reactions: The ETT stabilized sample shows 51 % inorganic residues after thermolysis, whereas the MTT stabilized sample only exhibits 6 %.

This means that a higher MTT excess has to be used in ligand exchange than in ETT ligand exchange and is in accordance with observations made with the performance of the exchange procedure.

Typically, more MTT is dissolved in chloroform than ETT for stabilizing the NCs. When (re)precipitating NCs for purification, small colorless residues, probably uncapped MTT, recrystallize.

To conclude, stabilizing trigonal pyramidal CIS with MTT leads to a high amount of unbound ligand that recrystallizes. However, it might be possible to improve the ligand exchange rate by modifying the exchange conditions.

Elongated CIS NCs are readily stabilized with MTT. TGA shows that NC samples contain 53 % inorganic residual mass after thermolysis of the ligand. The first mass loss in the TGA curve attributed to MTT thermolysis occurs at 238 °C, the same temperature as for ETT capped elongated CIS (see Figure 3.33 and Figure 3.23 on page 45).

MTT capped CIGS NCs exhibit interesting decomposition behavior when heated to the thermolysis temperature of the ligand. Figure 3.34 shows a first mass loss of 17 % in MTT capped CIGS already occurring at 170 °C and a second mass loss of 12 % at 260 °C.

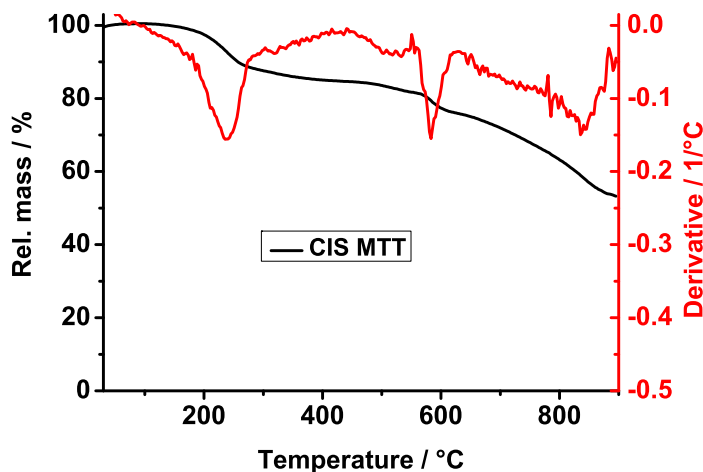


Figure 3.33: TGA of MTT stabilized elongated CIS NCs with a thermolysis temperature of 238 °C.

A two-stage MTT thermolysis seems reasonable here, as 170 °C is assumed to be the thermolysis temperature of pure MTT. Although the thermolysis temperature of pure MTT has been detected at higher temperatures (at 225 °C), the amount of the sample thermolyzed was significantly higher than the MTT amount used for NC stabilization.

Apparently, additionally to the kinetically controlled thermolysis of the thiotetrazole-based ligands by the heating rate, the weigh-in portion of MTT for thermolysis may have also an impact on the decomposition temperature of the compound. At 260 °C however, MTT bound to the CIGS NCs' surface most likely starts to thermolyze (like in ETT capped CIGS NCs at 255 °C) leaving 53 % inorganic residues.

Figure 3.35 exemplarily shows a densely packed CIGS NC film after thermolysis of the MTT ligand.

Despite the ligand exchange issues, MTT exchanged CI(G)S NC are characterized for their electrical transport properties (see section 3.9).

In conclusion, the use of ETT as ligand for CI(G)S NCs is more universal than the use of MTT as ligand for the chalcopyrite systems. Important insights in this section show that the thermolysis temperature of the thiotetrazole ligands is kinetically controlled and depends on the thermolysis heating rate.

By further adjusting the ligand exchange procedure to MTT, it might be possible to reduce the compound amount necessary for ligand exchange. A

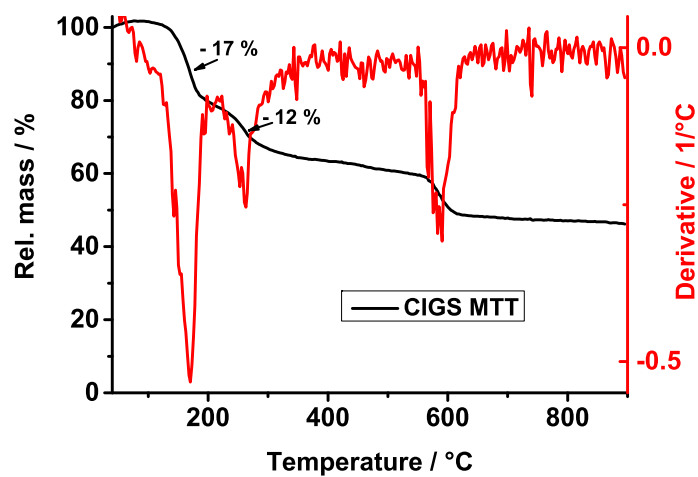


Figure 3.34: TGA of MTT stabilized CIGS NCS with the first mass loss of the excess unbound ligand at 170 °C and second mass loss of the NC bound ligand at 260 °C.

solvent adjustment and incubation temperature modification are the first steps taken to address the problem (see Experimental 5.3.2).

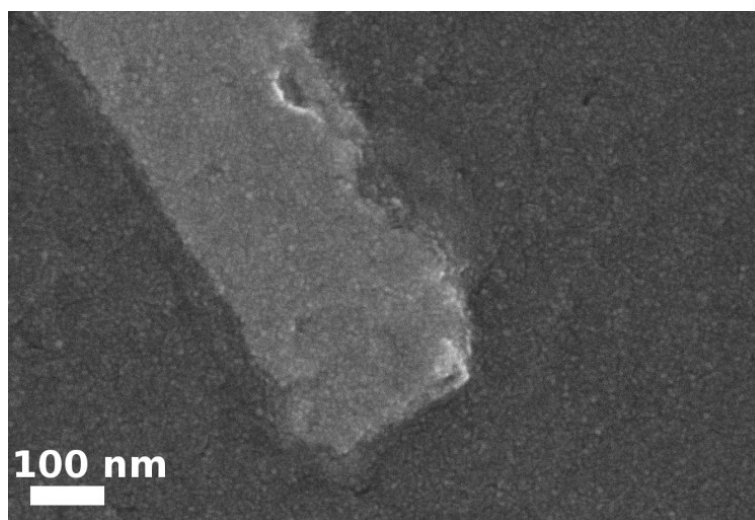


Figure 3.35: A densely packed MTT stabilized CIGS NC film on a gold electrode after annealing at 260 °C.

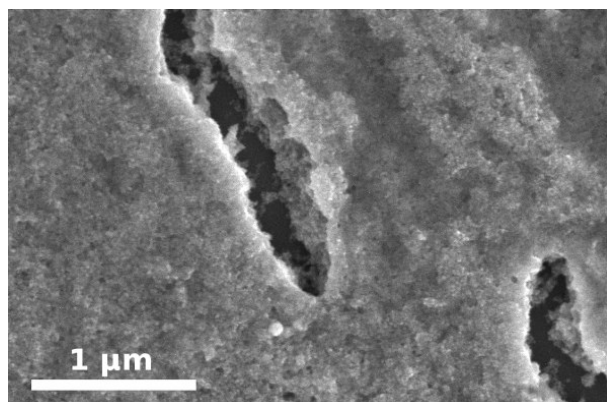


Figure 3.36: A trigonal pyramidal CIS NC film exhibiting cracks after treatment with Et_3OBF_4 .

3.5.3 Surface Modification: Meerwein's Salt (Et_3OBF_4)

Besides ligand exchanging CI(G)S NCs with thiotetrazoles, a different surface modification method is applied to remove oleylamine off CI(G)S NC surfaces.

Rosen *et al.* described the use of trialkyl oxonium salts (e.g. Et_3OBF_4) and other Meerwein compounds to mildly strip oleylamine, oleic acid and phosphine-based ligands off various NC surfaces without destroying the particular NCs.^[49] Et_3OBF_4 acts as strong alkylating agent which, in our case, reacts with the amine group of OLA, releasing the ligand from the then positively charged NC surface with BF_4^- as weakly bound counter ion.^[49]

The Meerwein's salt approach is applied for the first time to CI(G)S NCs.

The ligand stripping is performed under "solid state" conditions which means that the treatment with Et_3OBF_4 is applied after the NC deposition. It has to be stated that this can confine the applicability of the method as the ligand exchange might not be complete. Furthermore, solid state treatments often lead to crack formation in thicker NC assemblies.

Oleylamine capped trigonal pyramidal NCs are drop-coated onto a silicon substrate and treated with a 500 mM solution of Et_3OBF_4 (95 mg in 10 mL dichloromethane). The immersed substrates are rinsed with *n*-hexane to remove residual Et_3OBF_4 . Figure 3.36 shows a trigonal pyramidal CIS NC film with cracks (although the image features a small magnification of 1 μm and a wide range of the film). The same "film-cracking" observation is made for Et_3OBF_4 treated elongated CIS and CIGS NC films (see Figure 3.38 and 3.40).

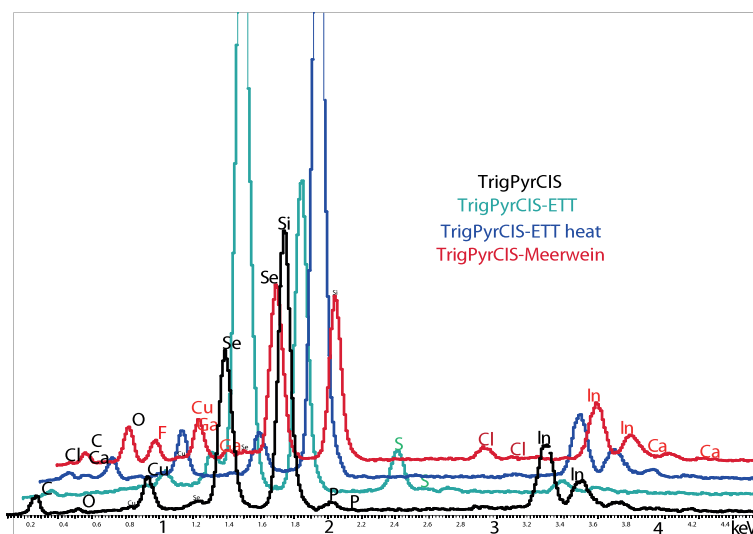


Figure 3.37: EDS of Et_3OBF_4 treated trigonal pyramidal CIS NC films.

To determine if residues of the Et_3OBF_4 treatment remain on the NCs, EDS of OLA stabilized CI(G)S NCs, ETT ligand exchanged NCs and NCs treated with Et_3OBF_4 are compared.

Figure 3.37 shows a spectrum of OLA capped trigonal pyramidal CIS, interestingly exhibiting a phosphorus and gallium signal although the NCs lack to be treated with TOP as additional stabilizing ligand and should not contain gallium. The phosphorus and gallium signals might originate from contamination of the sample or impurities in Et_3OBF_4 . Additionally, the spectrum reveals that after the Et_3OBF_4 treatment the sample contains fluorine, chlorine, calcium and large oxygen signals. This indicates the incomplete removal of the excess Meerwein's salt by rinsing the substrates with *n*-hexane.

EDS of elongated CIS NCs likewise exhibits fluorine (see Figure 3.39) pointing to an incomplete removal of the excess Meerwein's salt by *n*-hexane.

Figure 3.40 shows a CIGS NC film treated with Et_3OBF_4 with the associated EDS in Figure 3.41 featuring chlorine residues.

However, all CI(G)S NC stabilized with ETT show sulfur signals originating from the thiotetrazole ligand. After the treatment with Et_3OBF_4 or ligand exchange with ETT, no TOP remains on the CI(G)S NCs.

All CI(G)S NC samples treated with ETT as ligand show reduced carbon content after the thermolysis of the ligand. EDS measurements show that ETT capped CI(G)S NCs completely lose additional ligand originating ele-

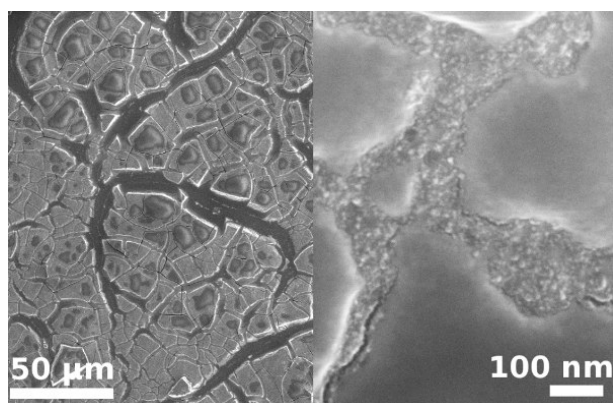


Figure 3.38: An elongated CIS NC film treated with Et_3OBF_4 and exhibiting cracks.

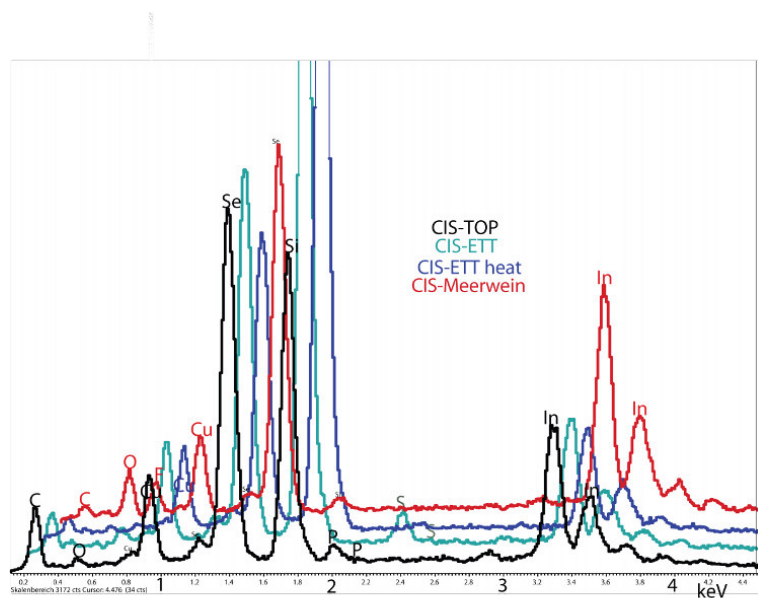


Figure 3.39: EDS of a Et_3OBF_4 treated elongated CIS NC film.

3.5 Ligand Exchange and Nanocrystal Surface Modification of *CI(G)S*

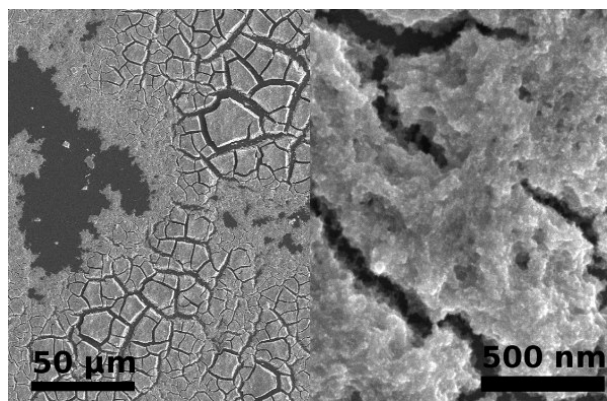


Figure 3.40: CIGS NCs treated with Et_3OBF_4 with film exhibiting cracks.

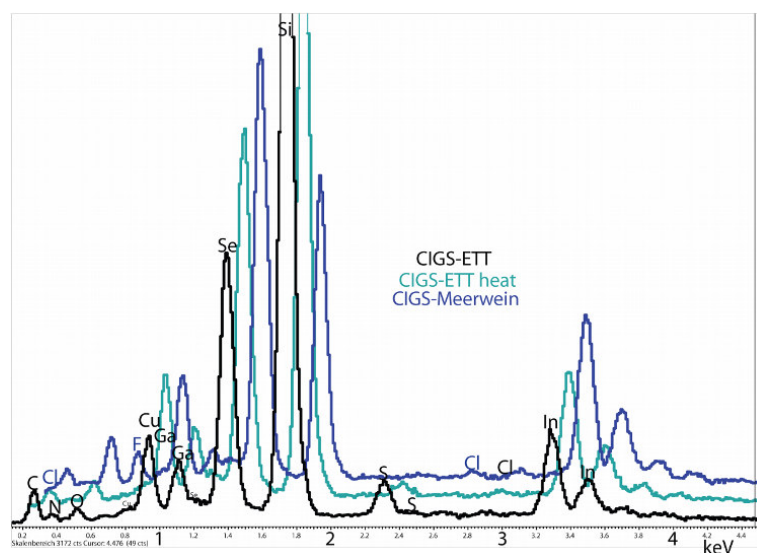


Figure 3.41: EDS of Et_3OBF_4 treated CIGS NC films.

ments (like sulfur, see Figure 3.37, 3.39 and 3.41) after the NC annealing step at 260 °C, whereas Et_3OBF_4 treatment might leave inorganic residues (fluorine or chlorine) originating from incomplete reactant removal and possible impurities.

In conclusion, the use of Et_3OBF_4 leads to inferior NC film formation in comparison with the thiotetrazole-based ligand exchange. The processed NC films universally exhibit film cracking which probably will lead to reduced effectiveness in electrical transport of the materials. Furthermore, the Et_3OBF_4 treatment has to be performed under inert gas conditions working inside the glovebox, whereas thiotetrazole-based ligand exchange can be performed under ambient conditions. As the NC films treated with Et_3OBF_4 contain residues from the treatment (at least halogens), blurred results in electrical transport measurements cannot be excluded.

The use of Et_3OBF_4 is effective with limitations in applicability to CI(G)S NCs and has to be thoroughly adjusted to enhance its utility. A first step would be to expand the solid state approach to a process in solution which has been possible with the Meerwein treatment for other NC types like CdSe/ZnS and CdSe/CdS quantum dots.^[49]

3.6 In-situ XRD Heating Experiments - Sintering CIS NCs

The successful ligand exchange of CI(G)S NCs with 1-ethyl-5-thiotetrazole described in 3.5 opens opportunities in using the materials properties after they have been deposited onto substrates from solution. One crucial feature of ETT is its thermolysis at relatively low temperatures (185-218 °C) depending on the heating rate and heating time (see 3.5.1).

The effect of the ETT ligand exchange on the sintering behavior of elongated CIS NCs is investigated. *In-situ* XRD measurements of ETT and OLA capped CIS NCs heated from 30-900 °C reveal sintering properties of the NCs and are compared with *in-situ* TEM heating experiments of elongated CIS NCs. (see 3.7). At every heating equilibration step, a diffractogram is recorded to monitor reflex width and crystal structure variations in the samples.

Especially for the determination of the electrical transport, it is important to assure that NCs lack sintering under the temperature treatment applied at 260 °C to thermolyze ETT (see 3.9) and form dense, nanostructured materials without increasing the grain size.^[104]

Sintering effects are thereby described by the elimination of interparticle pores in a granular material by atomic diffusion and driven by capillary forces.^[104]

The elongated CIS NC sample is filled into an Al₂O₃ crucible for the measurement. Once the particular temperature is reached the sample is equilibrated for 30 minutes. The Al₂O₃ crucible thereby exhibits sharp reflexes that are excluded from analysis and highlighted in most diffractograms by gray boxes.

Figure 3.42 shows the diffractogram of ETT capped elongated CIS NCs at room temperature compared with a diffractogram of OLA capped NCs measured on a silicon support plate.

The CIS NCs reflexes of both diffractograms fit the associated JCPDS card # 00-040-1487 for chalcopyrite CIS, whereas in the ETT stabilized elongated CIS NC diffractogram aluminum oxide reflexes of the crucible are visible at 25.58 °, 35.15 °, 37.78 °, 43.36 ° and 52.50 ° 2 Θ .

The reflexes chosen for the investigation and originating from CuInSe₂ are the distinct (112) reflex at 26.58 °, (204)/(220) at 44.12/44.23 °, (301) at 47.75 ° and the (312) reflex at 52.40 ° 2 Θ .

Figure 3.43 shows that by *in-situ* heating elongated CIS NCs in the range of 30 °C over 260 °C up to ~500 °C, no narrowing of the reflex width is detected in the diffractograms. It can therefore be assumed that at least in

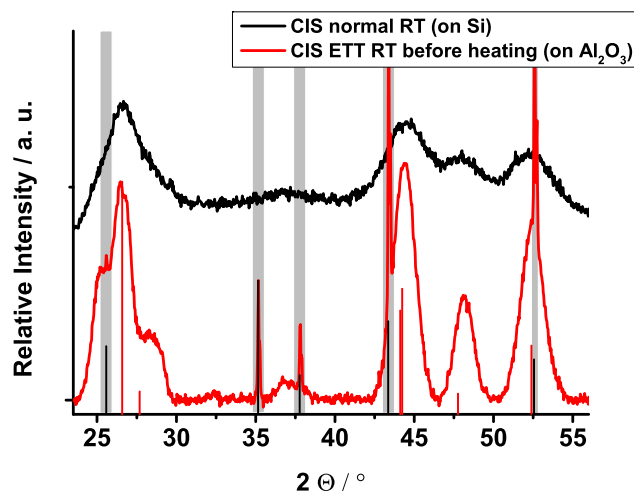


Figure 3.42: XRD of OLA stabilized elongated CIS NCs, measured on a silicon support plate (black) and ETT stabilized elongated CIS NCs measured inside the Al_2O_3 crucible (red), both diffractograms measured at room temperature.

the CI(G)S-ETT annealing range of 260 °C under ambient pressure, the NCs feature no sintering effects.

From 500 °C on, the CuInSe_2 reflexes start to narrow slightly as the material starts to (re)form to bulk (for comparison, see Figure 3.55 on page 73). Between 650 °C to 800 °C CuInSe_2 NC reflex widths significantly narrow.

Figure 3.44 shows the CIS sample at 800 °C exhibiting sharp CuInSe_2 reflexes.

After heating the sample to 900 °C the diffractogram is measured at room temperature (RT) (see Figure 3.45). The obtained reflex pattern is a mixture of crystal phases including Cu_2Se and CuInSe_2 . This is in accordance with EDS measurements after 900 °C, described in the *in-situ* TEM heating section (see 3.7).

In-situ XRD heating is likewise performed for OLA stabilized elongated CIS NCs. Figure 3.46 shows the temperature range between 30 °C and 900 °C. The reflex width in OLA stabilized elongated CIS is constant up to 700 °C, most likely due to long carbon chain residues of OLA preventing the material to start sintering. This observation is in accordance with the results of the *in-situ* TEM heating of OLA capped elongated CIS NCs (see Figure 3.62 on page 82).

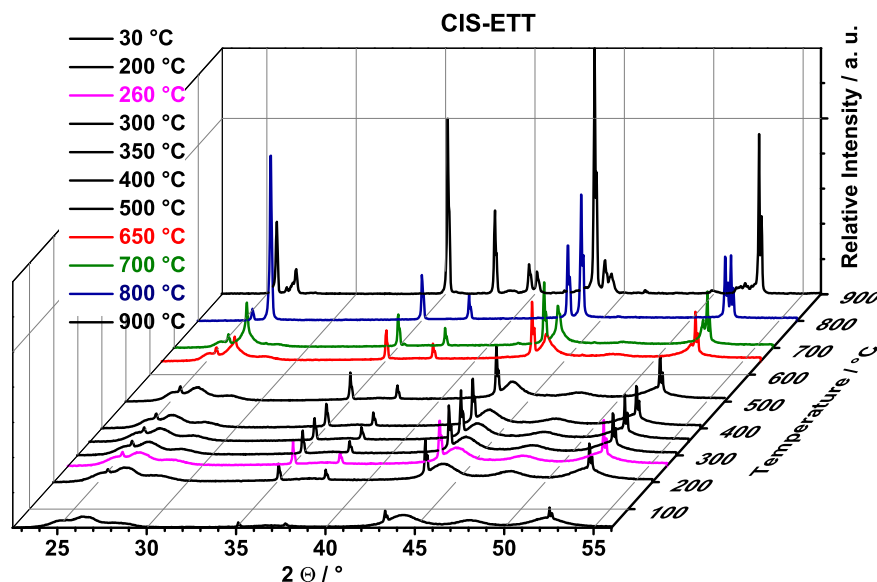


Figure 3.43: *In-situ* XRD heating rate of 30 °C to 900 °C with decreasing reflex width \sim 500 °C crossing over into sharp CuInSe_2 reflexes around 700 °C to 800 °C.

The reflex width of OLA capped CIS starts to narrow between 700 °C to 800 °C. TEM images taken at 800 °C show that OLA stabilized elongated CIS NCs are embedded in a ligand originating carbon matrix (see section 3.7.2, Figure 3.62 on page 82).

In conclusion, ETT capped elongated CIS NCs start to sinter at significantly lower temperatures (\sim 500 °C) than OLA capped elongated CIS NCs. Solid state CuInSe_2 starts phase transitions and melting in the range of 805-990 °C.^[105]

Examining ETT and OLA capped XRD diffractograms after heating to 900 °C shows that both diffractograms contain reflexes of mixed crystal systems including Cu_2Se and residual CuInSe_2 (see Figure 3.47).

It is important to note that OLA capped CIS generally show lower reflex intensity after heating to 900 °C than ETT-based CIS although both diffractograms are recorded under otherwise same measurement conditions. This supports the observations made during *in-situ* TEM heating: ETT capped elongated CIS NCs start forming crystalline sintered assemblies at higher temperatures. This crystalline "carpets" seem to endure temperatures of

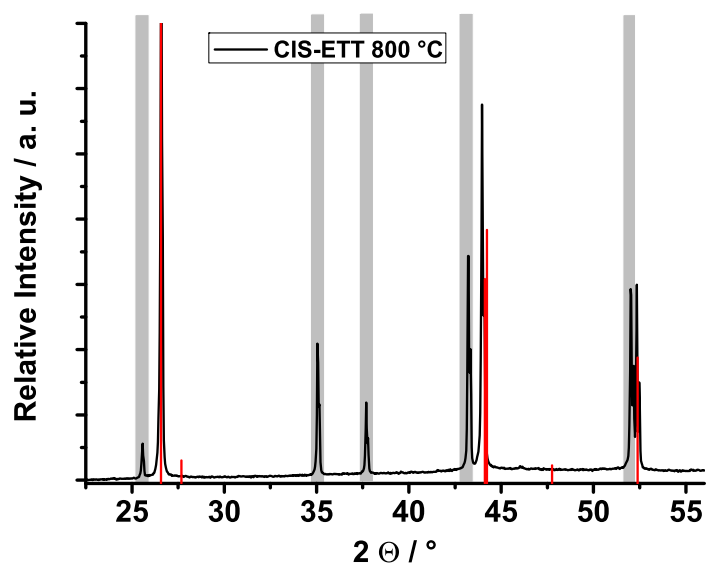


Figure 3.44: XRD of elongated CIS NCs measured in an Al₂O₃ crucible (highlighted in gray) at 800 °C exhibiting sharp reflexes with associated solid red lines indicating CuInSe₂ (JCPDS card # 00-040-1487).

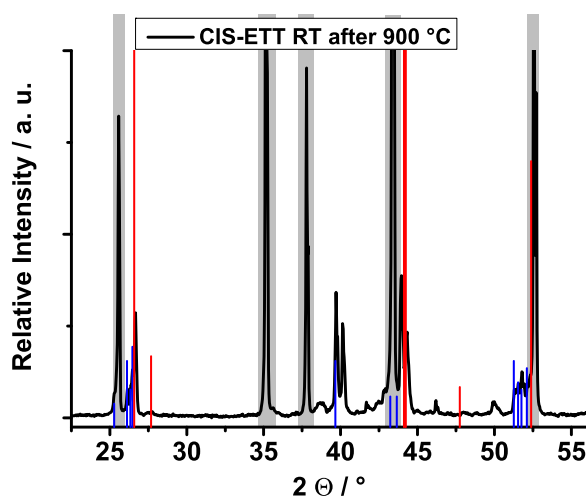


Figure 3.45: ETT stabilized elongated CIS NC sample at RT after heating to 900 °C and exhibiting mixed crystal phases including Cu_2Se (blue solid lines, JCPDS # 00-027-1131) and residual CuInSe_2 (red solid lines, JCPDS card # 00-040-1487), Al_2O_3 signals of the crucible are highlighted in gray.

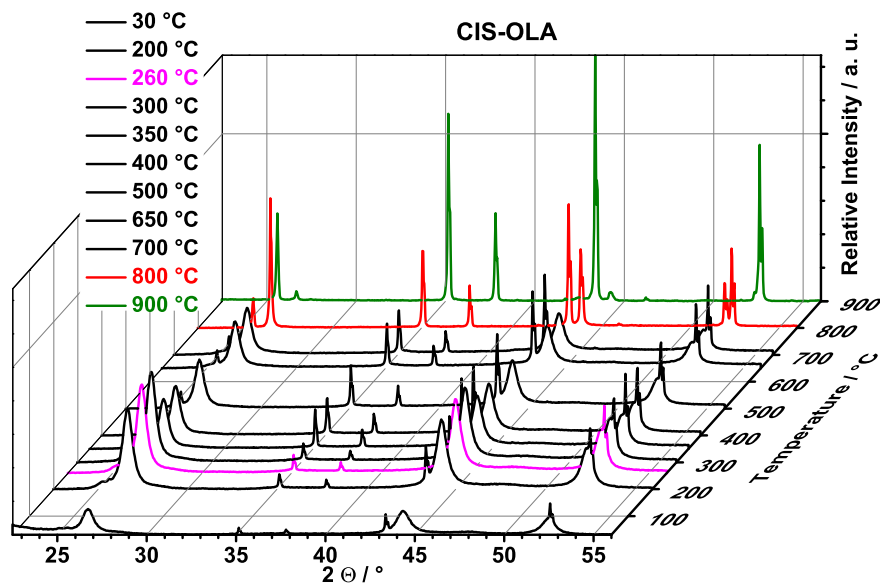


Figure 3.46: XRDs of elongated CIS NCs capped with OLA in the range of 30 °C to 900 °C with reflex width decreasing in the range of 700 °C to 800 °C.

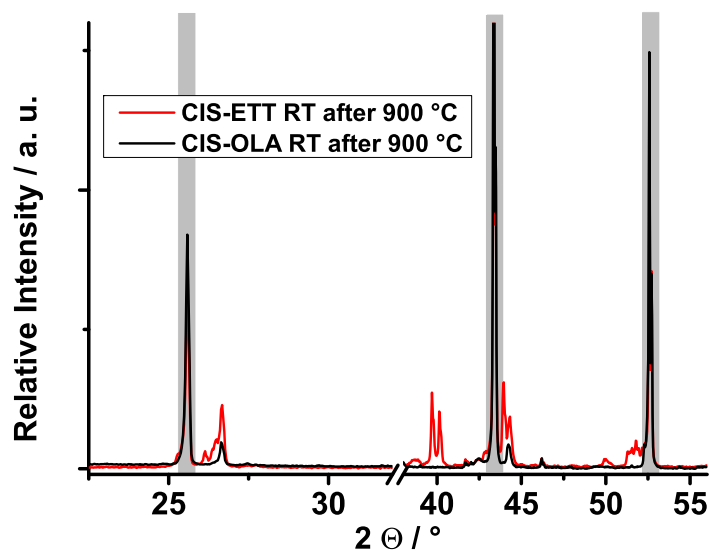


Figure 3.47: XRD of OLA and ETT capped elongated CIS after heating to 900 °C with diffractogram of ligand exchanged CIS showing more distinct mixed crystal phase reflexes, Al₂O₃ originating reflexes marked in gray.

900 °C better than OLA capped CIS which disintegrate into significantly smaller crystalline parts (see Figure 3.62 and 3.63 on page 82 and 83).

The results of the *in-situ* XRD heating experiments underpin the advantage of ETT as thermally degradable ligand with regard to residue-free sintering of CI(G)S chalcopyrite NCs. Due to the complete thermolysis of ETT, it can be assumed that NCs sinter cleanly to form crystalline assemblies at moderate temperatures in the range of 500 °C, whereas OLA covered NCs require more than 700 °C to start exhibiting narrowed reflexes.

3.7 In-situ TEM Heating Experiments - Sintering CI(G)S NCs and X-ray Photoelectron Spectroscopy of CIS Surfaces

To trace the exact processes during annealing of NC thin films and the eventual coalescence and sintering, stepwise *in-situ* TEM heating of ETT capped elongated CIS and CIGS NCs is performed and compared to *in-situ* TEM heating of OLA capped elongated CIS NCs.

The TEM experiments strongly support the results discussed in the *in-situ* XRD heating section for elongated CIS NCs. ETT stabilized CIGS NCs reveal that residual sulfur (the only inorganic residue remaining from the ligand exchange after ETT thermolysis) is completely removed in the temperature range of 25 °C to 400 °C. It is therefore assumed that sulfur atoms from the ligand exchange reside on the NC surface rather than being incorporated into the NC lattice.

A confirmation that sulfur from the ligand exchange is present at the CI(G)S NC surface is additionally exemplarily shown by X-ray photoelectron spectroscopy (XPS) of ETT capped elongated CIS NCs.

Figure 3.48 depicts the XPS survey spectrum of elongated CIS NCs. All elements are clearly detected in the suspected oxidation states. The FWHM of the measurement curves are fitted by the program used for evaluation, *CasaXPS*, automatically with a Marquardt function. The measured binding energies are corrected for charging of the specimen by referencing the obtained values to Au 4f with 84.0 eV.

Figure 3.49 shows the core-level spectra of Cu 2p orbitals in CIS NCs. The Cu 2p_{3/2} is centered at 932.2 eV and the Cu 2p_{1/2} at 952.0 eV well in accordance with literature values for CIS.^[106,107] The FWHM of the 2p_{1/2} is thereby slightly bigger than the FWHM of 2p_{3/2}.^[106,108]

It is important to note that there is no satellite peak detected at 940 eV which would originate from Cu²⁺ species in the CIS NCs.^[26,106-109] It can therefore be assumed that copper in the CI(G)S NCs investigated exclusively exists in oxidation state +1 (Cu⁺).

Figure 3.50 shows an In 3d_{5/2} and In 3d_{3/2} core-level spectrum centered at 444.9 eV and 452.3 eV and Figure 3.51 depicts the Se 3d_{5/2} and Se 3d_{3/2} core-level spectrum centered as one peak at 54.5 eV which lacks further splitting due to limited resolution of the spectrum. These values fit the values described for CIS.^[106,109]

Figure 3.52 depicts the core-level spectrum of sulfur which is originating from the sulfur atoms in ETT. Figure 3.53 combines survey spectra of all

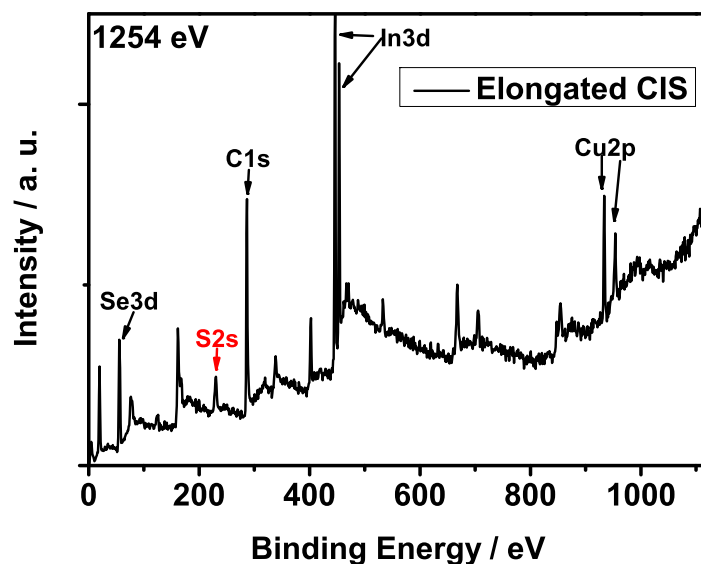


Figure 3.48: XPS survey spectrum of ETT capped elongated CIS NCs with the sulfur signal originating from ETT marked in red.

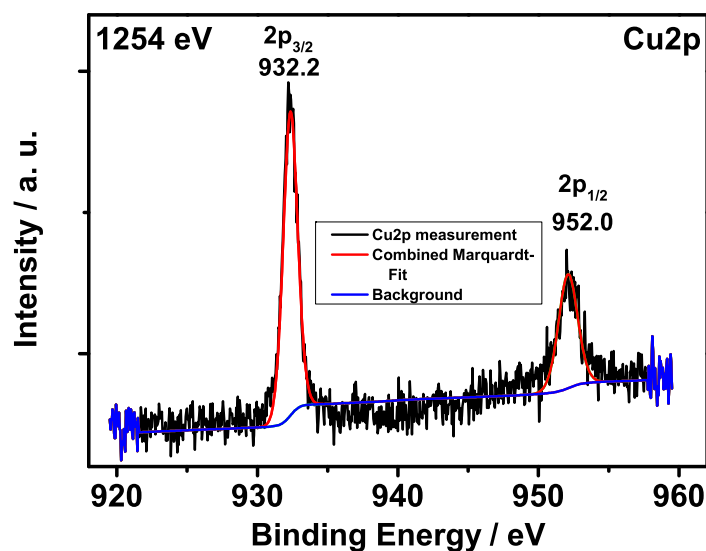


Figure 3.49: A Cu 2p core-level spectrum lacking the presence of Cu^{2+} .

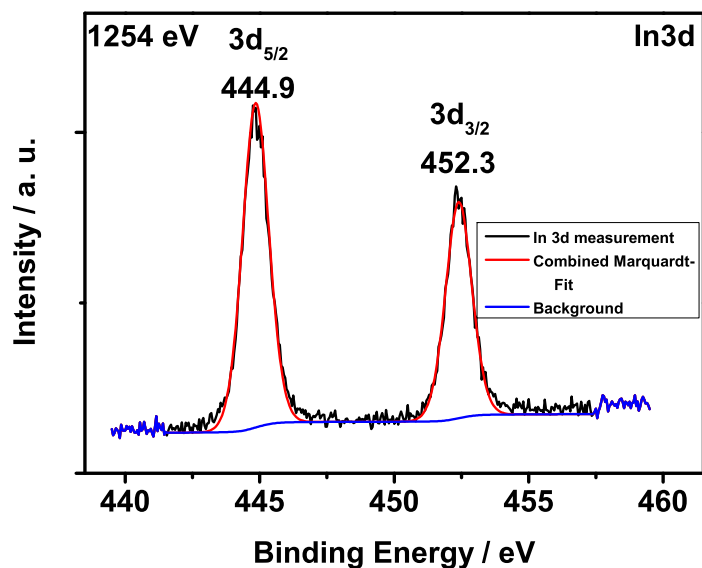


Figure 3.50: An In 3d core-level spectrum of ETT stabilized elongated CIS NCs.

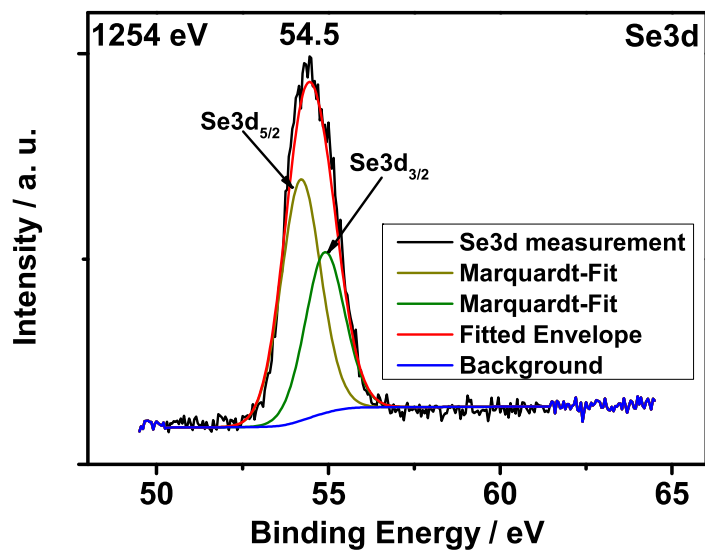


Figure 3.51: A Se 3d core-level spectrum of ETT stabilized elongated CIS NCs.

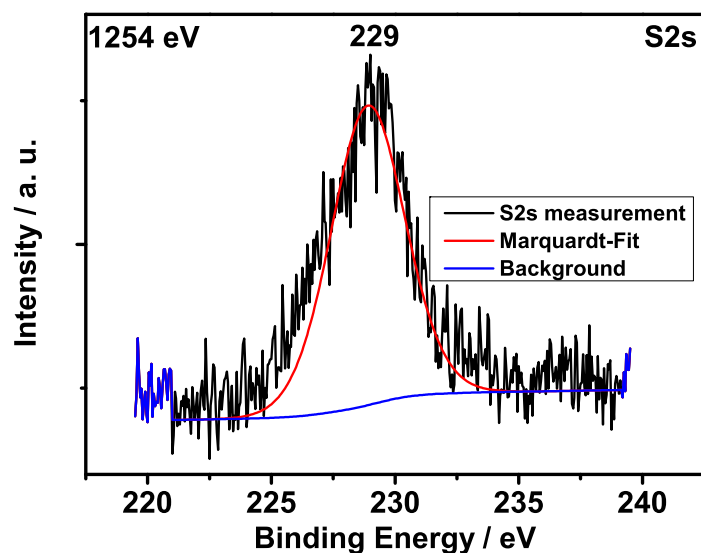


Figure 3.52: ETT originating sulfur core-level spectrum of the 2s sulfur orbital.

ETT exchanged investigated CI(G)S NCs and shows that every NC type exhibits sulfur on its surface from the ligand exchange.

What additionally can be seen is that all spectra feature a large carbon signal which may originate in its intensity from the *Highly Ordered Pyrolytic Graphite* (HOPG) used as measurement substrate. ETT capped CI(G)S NCs show the largest carbon signal as the samples deposited onto HOPG exhibit the lowest concentration.

XPS analysis of elongated CIS NCs additionally proves that the ligand is successfully bound to the surface of the investigated CI(G)S NCs.

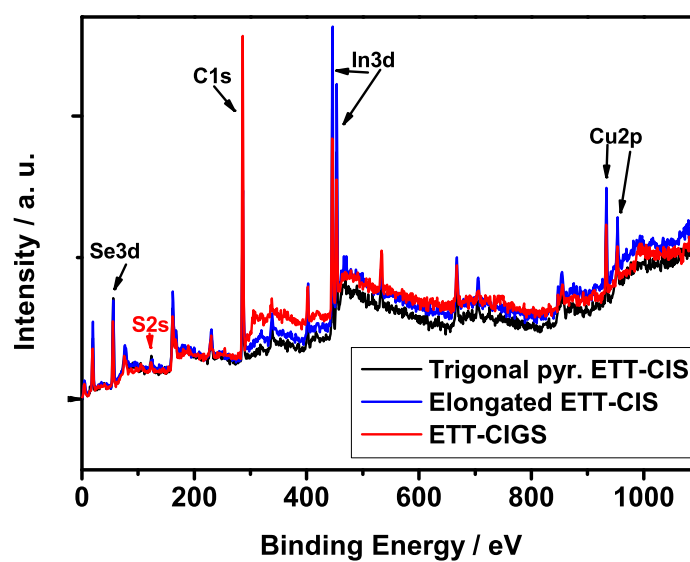


Figure 3.53: XPS of ETT capped CI(G)S NCs with all samples showing the sulfur signal originating from ETT.

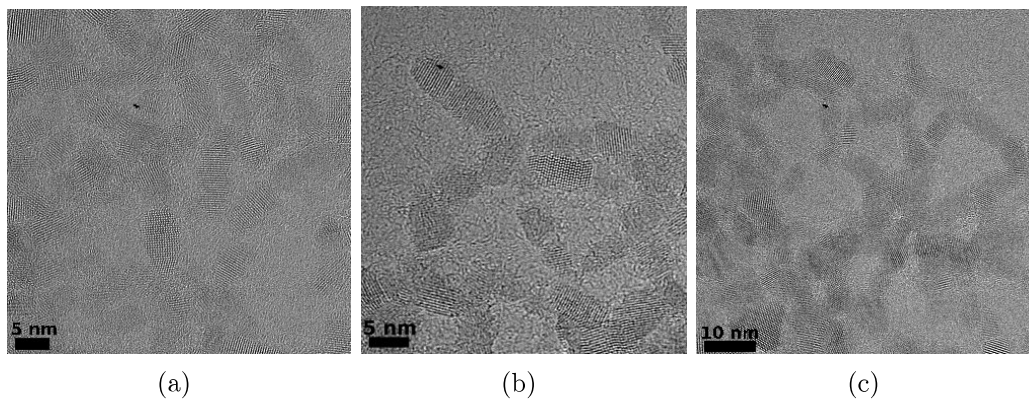


Figure 3.54: TEM images of elongated CIS-ETT NCs heated to (a) 25 °C, (b) 250 °C and (c) 300 °C.

3.7.1 Sintering Elongated CuInSe_2 -ETT NCs

The coalescence and sintering of ETT exchanged elongated CIS NCs described in the *in-situ* XRD heating section can also be visualized on the nanoscale by *in-situ* TEM analysis.

Elongated CIS NCs are heated in a temperature range from 25 °C to 900 °C and equilibrated at the particular temperature for 30 minutes prior to TEM analysis. Figure 3.54a shows the NCs before heating is started at 25 °C. The NCs exhibit interparticle distances originating from the ETT ligand shell which is also visible in Figure 3.54b at 250 °C.

However, at 300 °C the particles seem to have slightly migrated and approached each other, reducing the interparticle distance to a minimum extent (see Figure 3.54c). At 400 °C, sintering of CIS has already started. This means that sintering occurs in the range of 300 °C to 400 °C. At 400 °C NCs have started to form crystalline assemblies over a wider range (see Figure 3.55).

At 500 °C almost closed crystalline films have formed, representing the transition of the NCs to thin films of the solid state phase as described in the *in-situ* XRD section (see Figure 3.55 and 3.43). At 600 °C, the temperature where ETT capped CIS samples in *in-situ* XRD heating show narrowed reflexes associated to finished sintering and approaching bulk formation (see Figure 3.43 on page 63), TEM images likewise depict a finished sintering process. It is impossible to account for single, clearly separated NCs (see Figure 3.56).

The results of the *in-situ* TEM heating are in perfect accordance with results of the *in-situ* XRD heating section. The experiments show that at

3.7 *In-situ* TEM Heating Experiments - Sintering *CI(G)S* NCs and X-ray Photoelectron Spectroscopy of *CIS* Surfaces

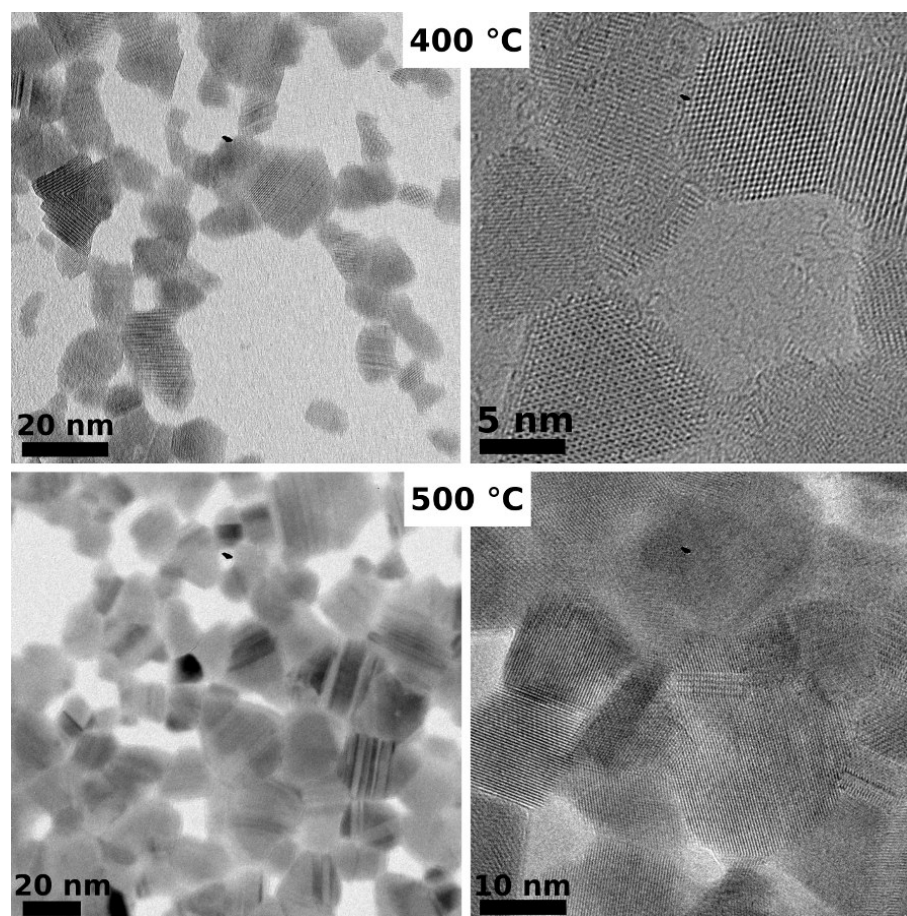


Figure 3.55: TEM images of elongated *CIS*-ETT NCs heated to 400 °C (upper row) respectively 500 °C (lower row), showing the transition from NCs towards solid state.

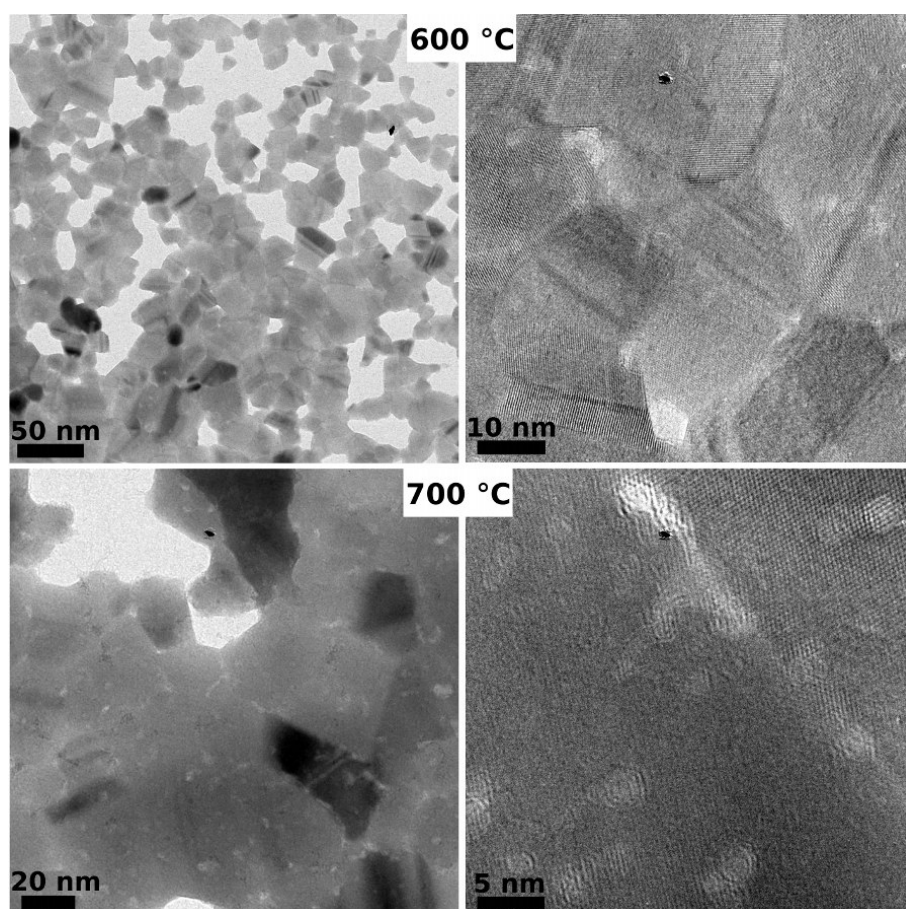


Figure 3.56: TEM images of elongated CIS-ETT NCs heated to 600 °C (upper row) and 700 °C (lower row), showing sintered crystalline "carpets".

~400 °C elongated CIS NCs start to coalesce (see Figure 3.55 and unaltered reflex width at 400 °C in Figure 3.43) and between 600 °C and 700 °C the material is completely sintered (see Figure 3.56 and Figure 3.43).

However, an additional influence of the electron beam or the high vacuum applied leading to slightly lower sintering temperatures in *in-situ* TEM heated samples, cannot be completely excluded.

From 700 °C onwards, the dense crystalline CIS "carpet" seems to slowly disintegrate (see Figure 3.56). This is the temperature range where selenium starts to evaporate from the sample^[18] (see TGA in 3.5.1.2) and the decomposition of the material approaches.

At 800 °C to 900 °C, big crystalline assemblies and additional small NCs are (re)formed under heat and the electron beam. The EDS of CIS NCs at

3.7 *In-situ* TEM Heating Experiments - Sintering CI(G)S NCs and X-ray Photoelectron Spectroscopy of CIS Surfaces

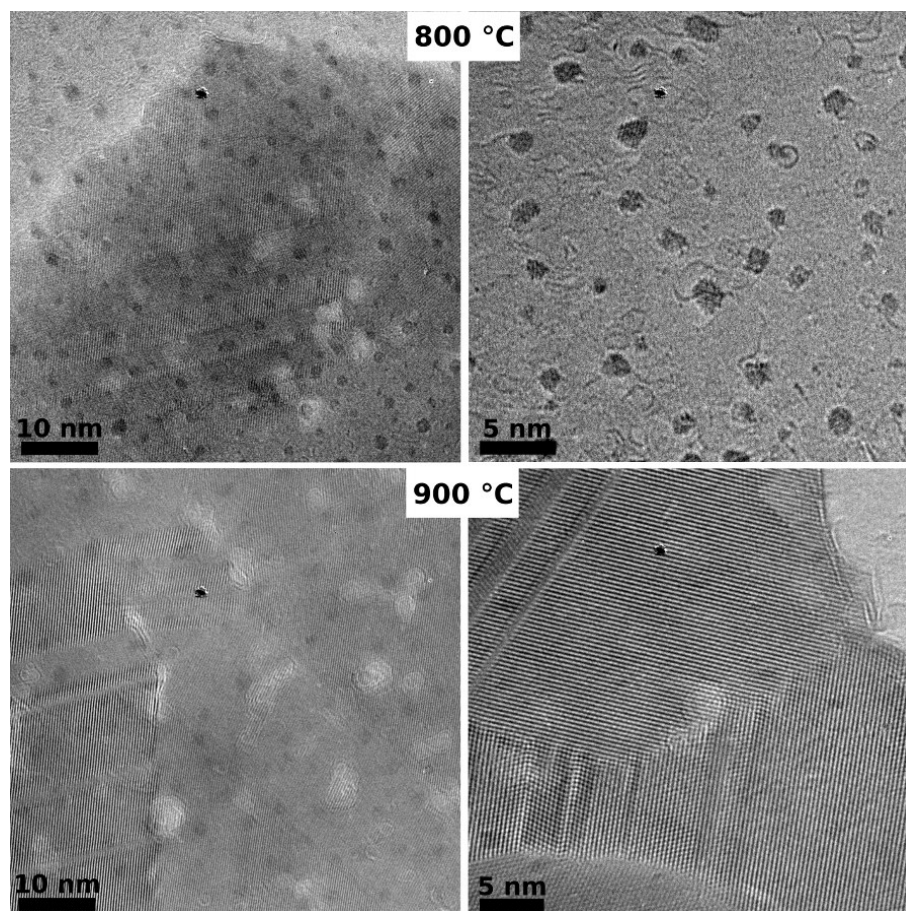


Figure 3.57: TEM images of elongated CIS-ETT NCs heated to 800 °C and 900 °C.

25 °C in table 3.3 is compared with the EDS of CIS after heating to 900 °C in table 3.4, showing that after heating the NCs the CIS structure vanishes and almost stoichiometric Cu_2Se is formed. Indium is reduced to a negligible content. This observation is in accordance with the results of the *in-situ* XRD section (see Figure 3.47 on page 66) although more indium is detected in CuInSe_2 diffractograms after heating to 900 °C. This is most likely due to the fact that *in-situ* XRD is measured under ambient pressure whereas *in-situ* TEM experiments are conducted under ultra high vacuum, leading to possible evaporation of indium.

Figure 3.58 shows a map of a crystalline "carpet" after the NCs have been heated to 900 °C similar to that displayed in Figure 3.57 (lower row). The map features only residual indium and a high copper and selenium content shown in the associated EDS measurement. The elements are evenly

Elongated CIS-ETT at 25 °C		
Element	Atom%	Error
Cu K*	19.40	0.05
Se (Ref.) L*	55.07	0.02
In L*	22.69	0.04
S K*	1.85	0.68

Table 3.3: EDS of ETT capped elongated CIS at room temperature in atom%.

Elongated CIS-ETT after 900 °C		
Element	Atom%	Error
Cu K*	65.19	0.01
Se (Ref.) L*	34.46	0.01
In L*	0.36	0.97

Table 3.4: EDS of ETT capped elongated CIS after heating to 900 °C in atom%.

3.7 *In-situ* TEM Heating Experiments - Sintering CI(G)S NCs and X-ray Photoelectron Spectroscopy of CIS Surfaces

distributed, supporting the assumption that single elements are not accumulating at certain positions.

In-situ TEM and XRD heating of elongated CIS NCs reveals that ETT exchanged CIS NCs can be readily sintered and transformed into thin film bulk material at temperatures between ~ 500 - 650 °C to yield crystalline CIS assemblies.

In the following section it is described that sintering to form wide-spread crystalline assemblies is impossible with OLA stabilized NCs.

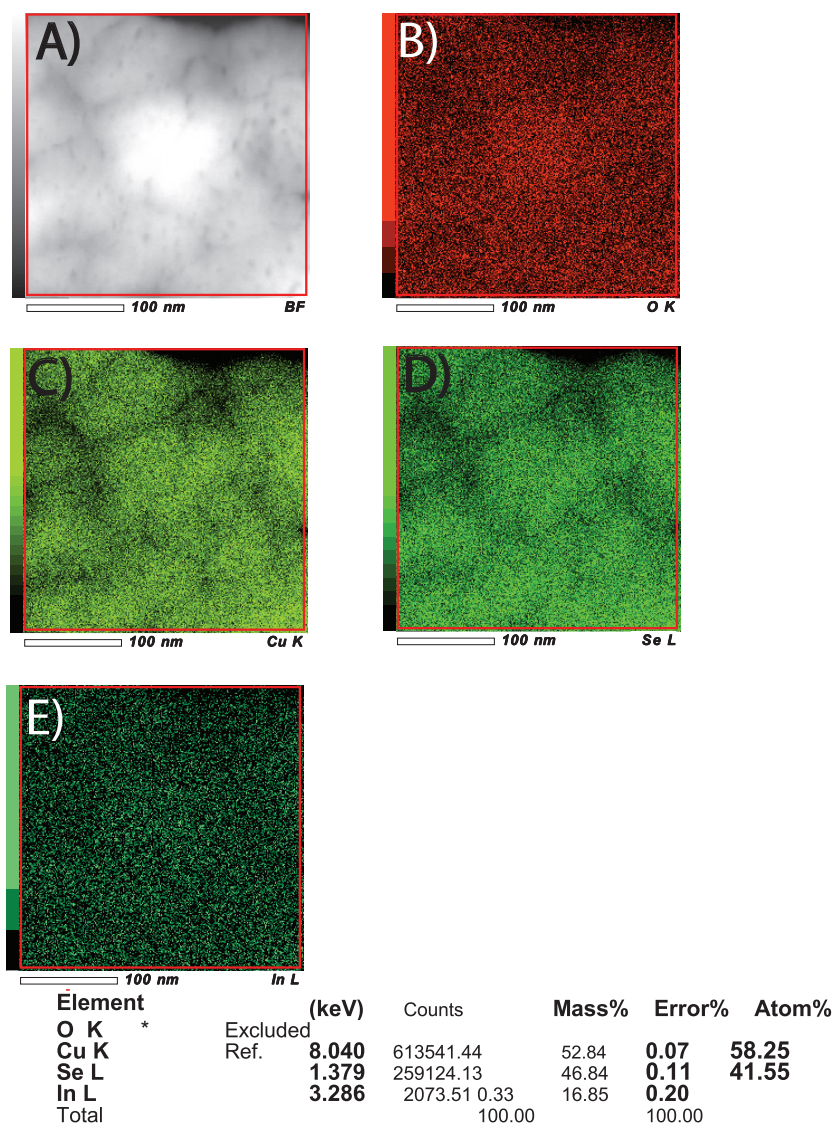


Figure 3.58: Element mapping of a crystalline "carpet" after heating of CIS-ETT NCs to 900 °C, showing a uniform distribution of the remaining elements: A) bright field STEM image, B) EDS scan at O K peak, C) EDS scan at Cu K peak, D) EDS scan at Se L peak and E) EDS scan at In L peak.

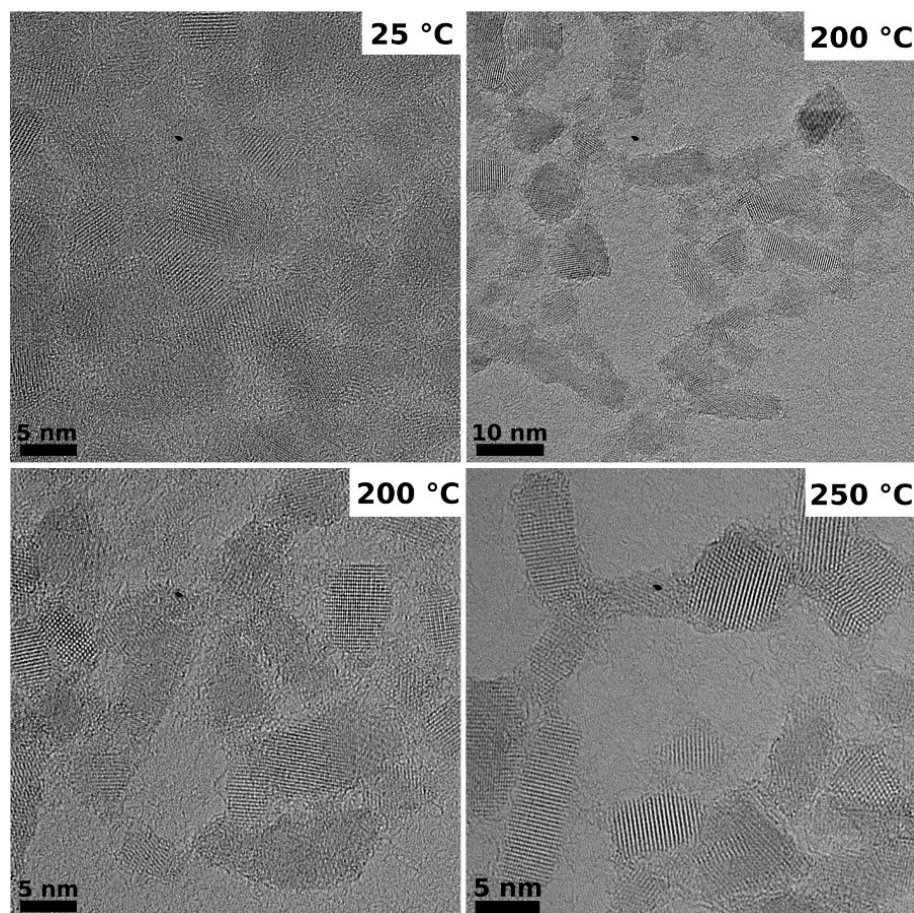


Figure 3.59: TEM images of elongated *CIS*-OLA NCs heated to 25, 200 and 250 °C exhibiting first carbonization effects around 200 °C.

3.7.2 *In-situ* TEM Heating of OLA Stabilized Elongated CuInSe_2 NCs

The straightforward coalescence and sintering behavior of ETT capped elongated *CIS* NCs is compared with the temperature dependent behavior of OLA stabilized elongated *CIS* NCs.

Figure 3.59 shows OLA capped elongated *CIS* in the heating range of 25 °C to 250 °C. It shows that the NCs lack changes in appearance under elevated temperatures but a "corona" appears covering the NC surfaces at temperatures around 200 °C and higher.

This corona can be assigned to the starting carbonization of the oleylamine ligand when heat is applied to the NCs and has been described by other groups before.^[110]

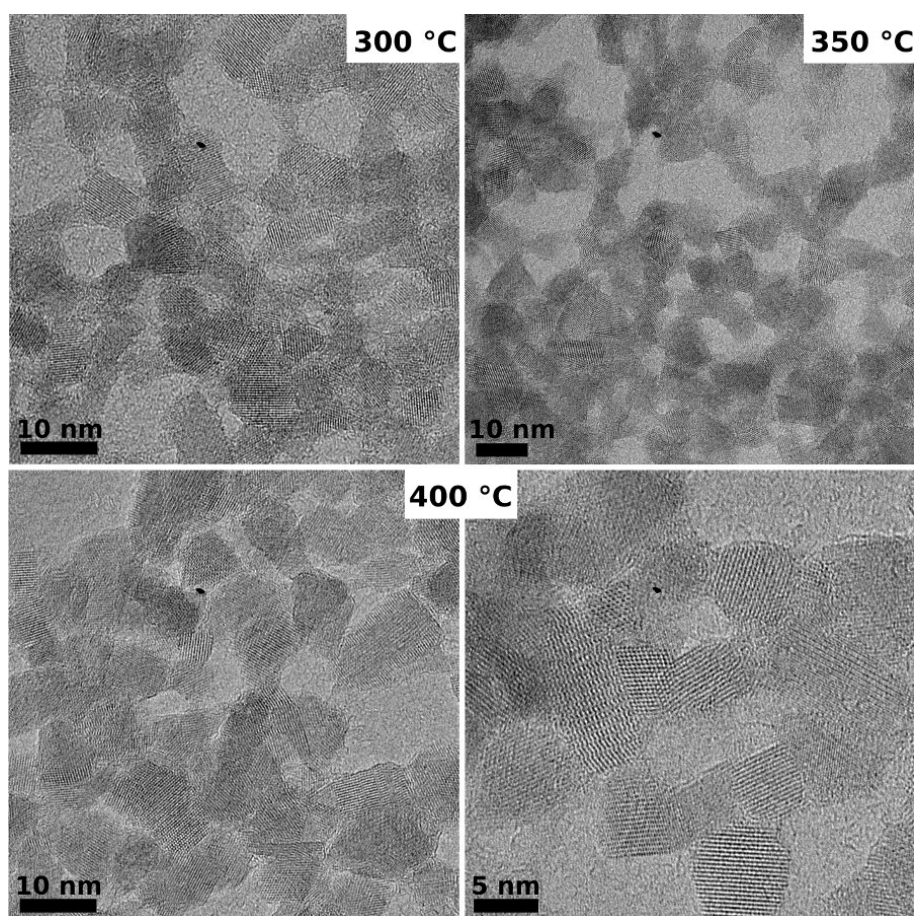


Figure 3.60: TEM images of elongated CIS-OLA NCs heated to 300 °C and 400 °C featuring carbonization effects.

In the temperature range of 300 °C to 400 °C (see Figure 3.60), the range where ETT capped CIS show the first coalescing and sintering effects, the NCs stabilized with OLA lack distinct changes in structure and appearance. The carbon originating corona is still visible.

These observations support the *in-situ* XRD heating experiments at these temperatures (300-400 °C), as here, likewise, the reflex width of the OLA stabilized NCs remains unaltered (see Figure 3.46 on page 65).

At 505 °C to 600 °C, it is revealed that OLA capped NCs do not sinter as easily as ETT capped NCs (see Figure 3.61).

The NCs are still individual at this temperatures in contrast to the ETT capped analoga. The carbonization corona covering the individual NCs shows that there are still organic residues located around the NCs (see Figure 3.61).

At 600 °C, the amorphous carbon residue on the NCs is clearly visible.

3.7 *In-situ* TEM Heating Experiments - Sintering CI(G)S NCs and X-ray Photoelectron Spectroscopy of CIS Surfaces

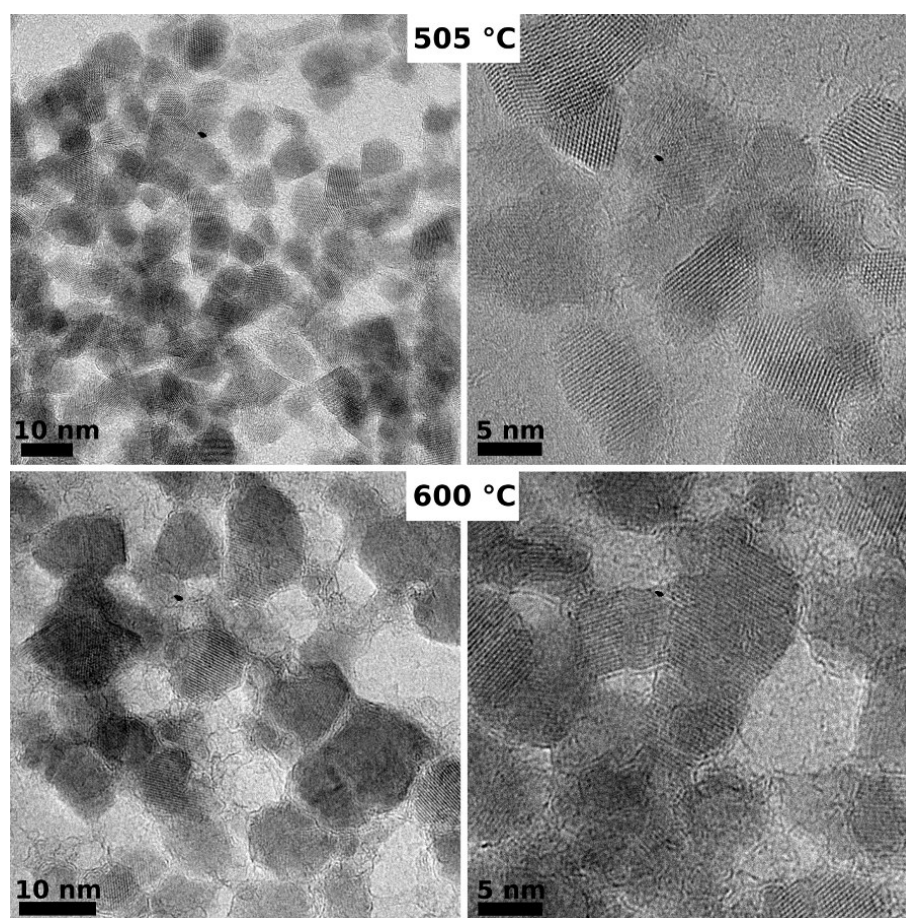


Figure 3.61: TEM images of elongated CIS-OLA NCs heated to 505 °C and 600 °C with single NCs covered by a carbon "corona".

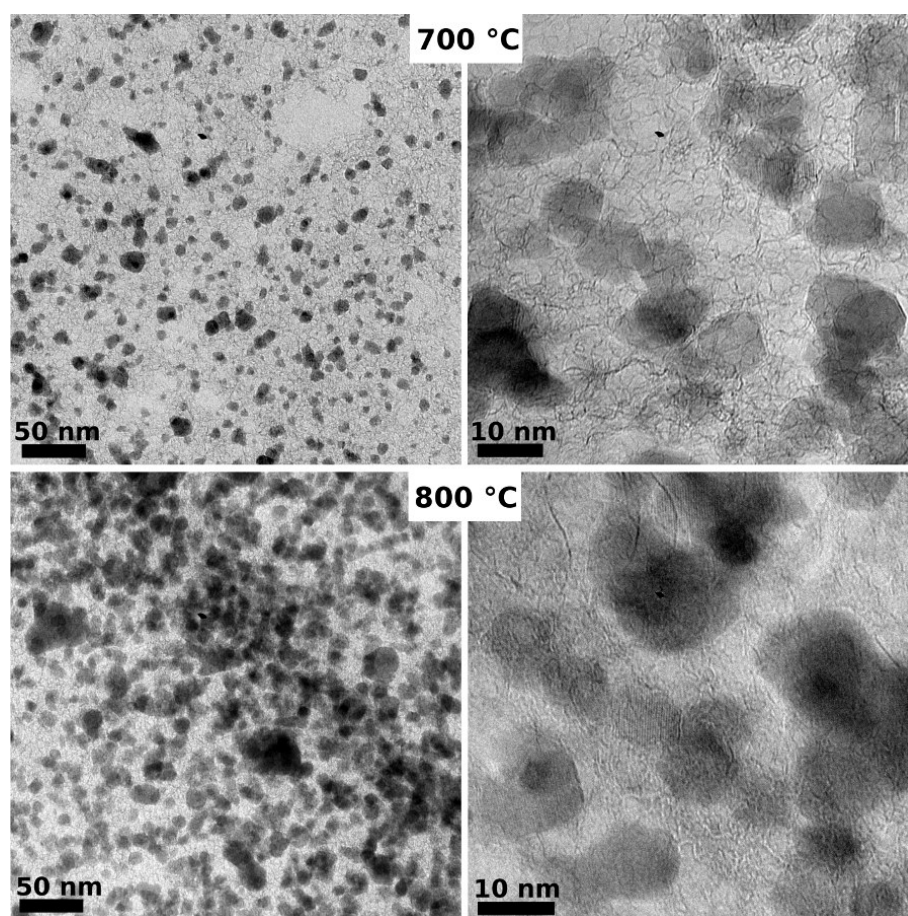


Figure 3.62: TEM images of elongated CIS-OLA NCs heated to 700 °C and 800 °C and exhibiting smaller crystalline pieces.

Between 700 °C and 800 °C, it seems as if the amount of nanocrystalline material decreases. Eventually, CIS NCs start coalescing but simultaneous decomposition and formation of crystalline residues is also observed. As described in section 3.6 on page 63, the carbonization manifests by a lack of reflex narrowing in XRDs of heated OLA capped samples until there is enough energy from heating to clearly overcome the coalescing barrier.

In contrast to the ETT-capped analoga, the results in Figure 3.62 are interpreted such that the NCs do not organize in close assemblies at these high temperatures. Instead, the material disintegrates into unspecified crystalline residues.

Table 3.5 and 3.6 depict EDS measurements of OLA capped CIS NCs prior to and after heating to 900 °C. Eventually, OLA capped samples transform

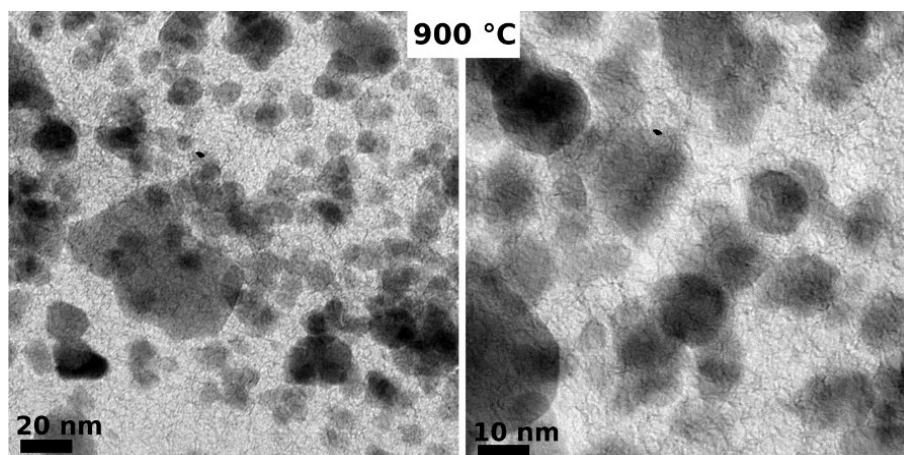


Figure 3.63: TEM images of elongated CIS-OLA NCs heated to 900 °C.

Elongated CIS-OLA at 25 °C		
Element	Atom%	Error
Cu K*	18.58	0.86
Se (Ref.) L*	56.83	0.33
In L*	24.59	0.56

Table 3.5: EDS of OLA capped elongated CIS at room temperature in atom%.

into the same residual mixed crystal systems, including Cu_2Se , like shown for ETT capped CIS.

The performance of OLA capped CIS NCs to form sintered crystalline assemblies is way inferior to the performance of ETT capped CIS. This is due to the fact that closer crystalline "carpet"-like assemblies can only form if the NCs can freely sinter together. This is not the case when they are stabilized with OLA even though high temperatures are applied.

It is underpinned that the widespread thinking of thermally decomposing long-chained organics is wrong and does not lead to nicely sintered materials. In fact, the application of ETT leads to a possibility to produce superior thin bulk-like films.

Elongated CIS-OLA after 900 °C		
Element	Atom%	Error
Cu K*	66.78	0.03
Se (Ref.) L*	31.18	0.07
In L*	2.04	0.77

Table 3.6: EDS of OLA capped elongated CIS after heating to 900 °C in atom%.

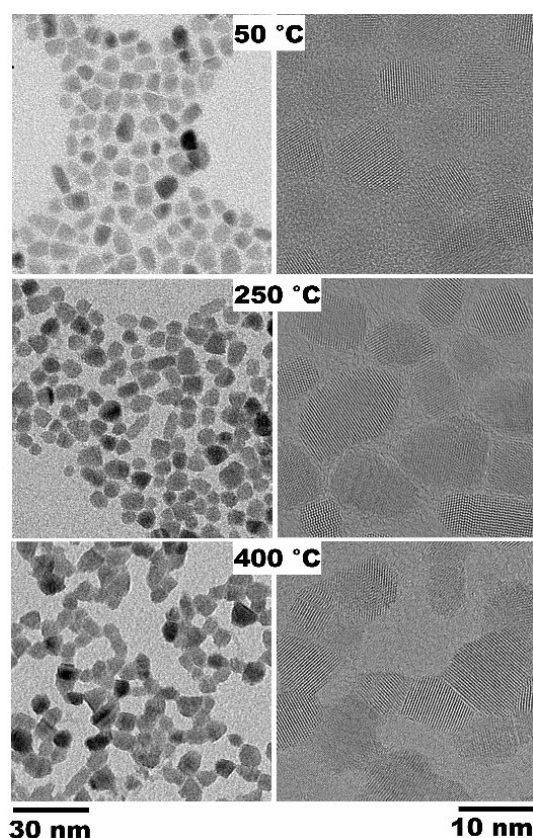


Figure 3.64: *In-situ* TEM heating of CIGS-ETT NCs at 50 °C, at 250 °C with reduced interparticle spacing and started sintering at 400 °C.^[18]

3.7.3 Sintering $\text{CuIn}_{1-x}\text{Ga}_x\text{Se}_2$ -ETT NCs

In-situ TEM sintering of ETT exchanged CIGS is performed with respect to the sulfur amount and the sintering behavior of the CIGS NCs.^[18] In a temperature range up to 400 °C, the CIGS NCs do not alter their composition and chalcopyrite crystal phase (see Figure 3.64).

At every heating equilibration step, an EDS is measured. Figure 3.65 shows the associated EDS at the different temperatures. At 50 °C there is a clear sulfur signal originating from ETT. The materials' composition and chalcopyrite crystal phase thereby are unaltered in the temperature range up to 400 °C also seen in the *Selected Area Electron Diffraction* (SAED) of the sample (see Figure 3.66).

Figure 3.64 shows CIGS NCs at different temperatures. A reduced interparticle distance as determined by *Small Angle X-ray Scattering* (SAXS, see section 3.8) is also apparent in the TEM images at 250 °C, the temperature

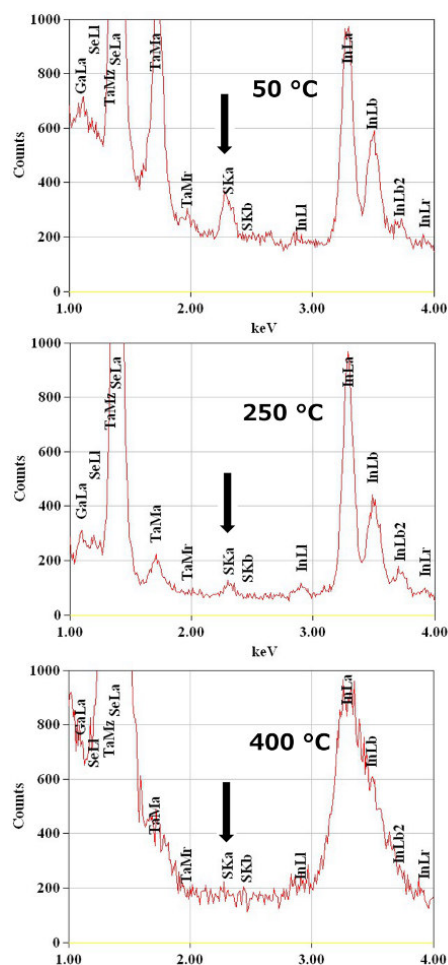


Figure 3.65: The sulfur content originating from ETT is completely removed during heating of the sample.

where ETT starts to decompose. At 400 °C the NCs have started sintering and form assemblies. During heating of the CIGS NCs residual sulfur from ETT exchange is completely removed within the heating range (see Figure 3.65).

When heating CIGS NCs to 550 °C and higher, the same dense crystalline assembly formation occurs as described for elongated CIS in 3.7.1.

In summary, the success of the ligand exchange is underpinned. It is possible to sinter CI(G)S NCs after the thermolysis of ETT at significantly lower temperatures than OLA capped NCs.

Thin films of NC solids are obtained that can be heated to temperatures where the particles migrate closer together but still show the composition of

3.7 *In-situ* TEM Heating Experiments - Sintering CI(G)S NCs and X-ray Photoelectron Spectroscopy of CIS Surfaces

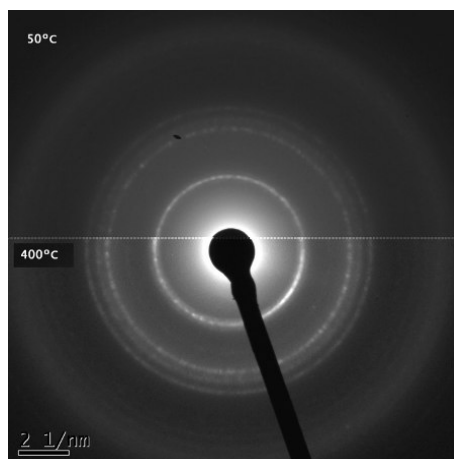


Figure 3.66: SAED of *in-situ* TEM heated CIGS NCs, materials composition and crystal phase stay unaltered between 50 °C and 400 °C.

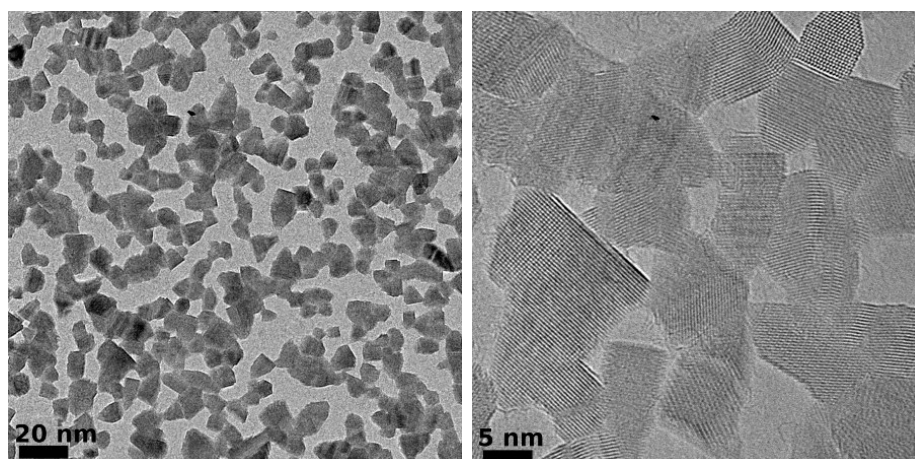


Figure 3.67: ETT capped CIGS NCs, heated to 550 °C

3 Results and Discussion

the initial NCs. This is an additional feature which opens NCs' wide range applicability for different research approaches.

During further heating, the NC solids start sintering without detrimental carbonization effects like detected in OLA stabilized samples.

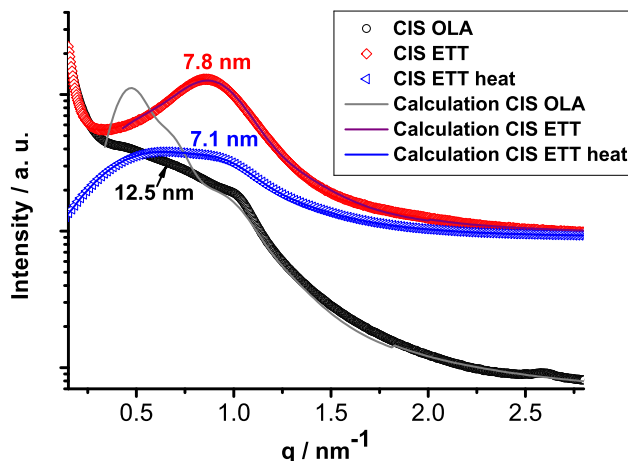


Figure 3.68: SAXS of elongated CIS NCs with reduced center-to-center distance and improved ordering of NCs after ETT exchange.^[18]

3.8 Small Angle X-ray Scattering (SAXS) of CI(G)S NCs

To examine long-range ordering of ETT capped CI(G)S NCs in comparison with initially OLA capped samples, *Small Angle X-ray scattering* (SAXS) measurements are performed. The use of spherical and cylindrical form factors and structure factors which represent the ordering of the NCs allow for the precise determination of size and shape of the investigated CI(G)S NCs, the interparticle distances and their size distribution.

SAXS reveals that the interparticle distance of NCs decreases after ligand exchange from OLA to ETT and underpins the successful procedure. The center-to-center distance of elongated CIS NCs (size distribution: $5.6 \text{ nm} \pm 1.4 \text{ nm}$ in length) decreases by 4.7 nm after ETT exchange (Figure 3.68).^[18] This high value originates from the broad scattering profile of the NCs and leads to certain inaccuracies in NC size distribution and in OLA length and spacing estimation.

However, after ligand exchange ETT capped samples show significantly improved ordering, visible in the narrowed peak width of the scattering curve and the fit quality of the associated simulated pattern. After heating the samples to $260 \text{ }^\circ\text{C}$ for 90 minutes, the center-to-center distance of the ligand-free NC films further decreases by 0.6 nm. At the same time the peak width broadens due to close assembling and aggregation of the NCs in bare films.

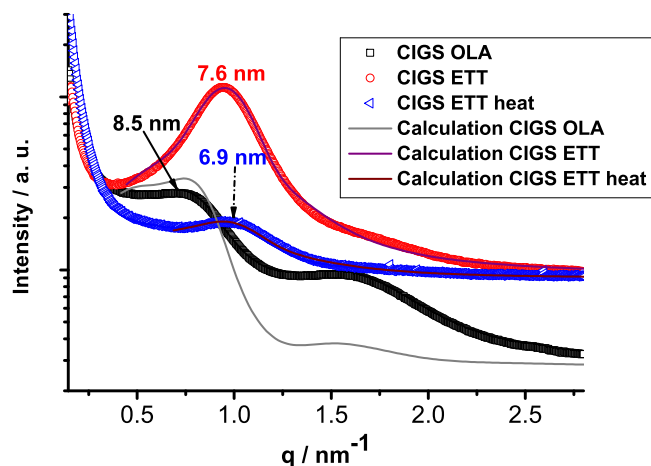


Figure 3.69: SAXS of CIGS NCs prior to and after ligand exchange with the center-to-center distance decreasing from OLA capped over ETT exchanged to heated ligand-free NCs.^[18]

The center-to-center distance of CIGS NCs ($7.4 \text{ nm} \pm 1 \text{ nm}$) decreases by 0.9 nm after ligand exchange (Figure 3.69). The peak width is significantly narrowed indicating small size distribution of the NCs and improved ordering. After annealing of the sample at $260 \text{ }^\circ\text{C}$, the center-to-center distance of the NCs further decreases by 0.7 nm and the peak width of the heated samples broadens like described for CIS NCs (see *in-situ* TEM heating experiments in 3.7, Figure 3.64, closely assembled individual CIGS NCs at $250 \text{ }^\circ\text{C}$).

SAXS patterns of trigonal pyramidal CIS NCs are excluded as the particles have a broad size distribution and lack distinct long-range ordering.

The scattering results show that elongated CIS and CIGS NCs both feature improved long range ordering after ligand exchange upon ETT, accentuating the beneficial role of ETT as ligand for the chalcopyrite systems.

3.9 Electrical Transport Measurements and Conductivity

Electrical transport in closely assembled NC solids is highly dependent on the NC surface functionalization (see section 2.5).^[18] Long-chained organic capping agents suppress effective interparticle coupling and lead to high tunneling barriers for electrons and thus insulating behavior of the materials.^[50] Reduced interparticle distance improves particle coupling and hence charge transport in NC assemblies.

To monitor and measure the effect of reduced interparticle distance upon ligand exchange with ETT (determined by TEM and SAXS, see subsection 3.7.1 and 3.7.3 and section 3.8), the electrical transport properties of CI(G)S NCs are determined prior to and after ETT thermolysis (see Figure 3.70). The results are compared to conductivities of MTT stabilized CI(G)S NC films and OLA capped CI(G)S NC films.

ETT exchanged CI(G)S NC films show up to 3.6 orders of magnitude enhanced conductivities after ETT thermolysis under illumination. CIS NC films thereby show a higher conductivity improvement than CI(G)S NC films. The difference is explained by the generally high number of surface originating trap states in CI(G)S materials which leverage to a greater extent in smaller NCs with a higher surface-to-volume ratio.

The conductivities of MTT stabilized CI(G)S NC films lie in the same range like ETT capped samples and underpin the general suitability of thio-tetrazole-based ligands with low thermolysis temperature for processing ligand-free NC solids.

Interestingly, OLA stabilized CI(G)S NC films exhibit relatively high conductivities after thermal annealing of the films at 260 °C. This enhancement is attributed to carbonization effects known to occur in long-chained hydrocarbon ligand stabilized and heated NC films. The results for improved conductivity in OLA capped annealed CIS NC films are in agreement with observations made during *in-situ* TEM experiments (see section 3.7). The NCs are embedded in a ‘carbon-matrix’ (see Figure 3.59 at 250 °C and Figure 3.60 at 300 °C on page 79, respectively 80) leading to enhanced electrical transport.

Exemplarily heating and electrical transport characterizing OLA stabilized CI(G)S NCs once more supports the beneficial role of the thiotetrazole-based ligands as they in contrast yield organics-free NC solids.

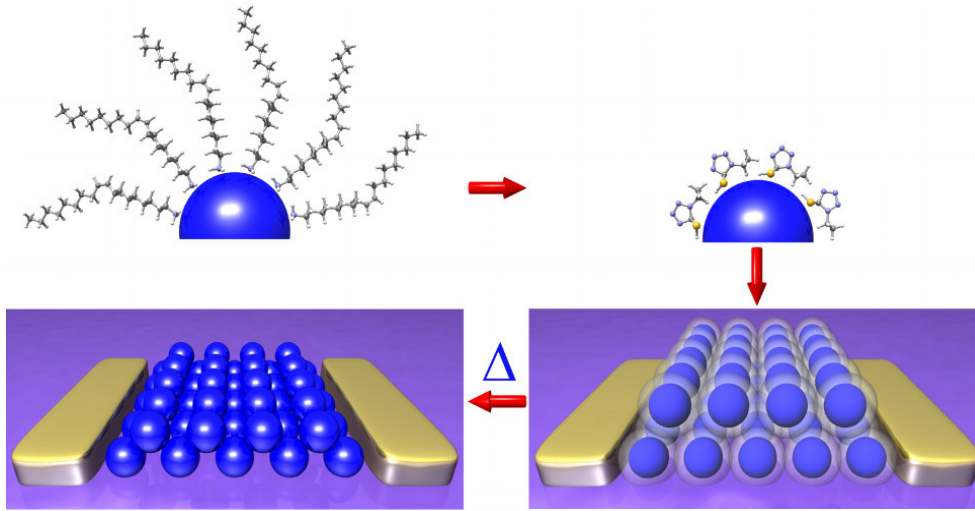


Figure 3.70: Ligand exchange scheme of CI(G)S NCs with ETT and subsequent spin-coating step, film processing and electrical transport measurements prior to and after thermolysis of the ligand.^[18]

3.9.1 ETT stabilized CuInSe_2 and $\text{CuIn}_{1-x}\text{Ga}_x\text{Se}_2$ NCs

As ETT undergoes thermolysis at different temperatures for the three CI(G)S systems (see Figure 3.22, 3.23 and 3.24), all NC thin film samples are heated to 260 °C to assure complete ETT thermolysis and comparable conditions, but prevent sintering of the NCs as observed in the range of 400 °C (see section 3.6 and 3.7).

In a typical experiment, 20 μL ($2 \times 10 \mu\text{L}$) of a colloidal CI(G)S NC solution are spin-coated (20 sec at 500 rpm, subsequently 20 sec at 2000 rpm) onto a highly n-doped silicon substrate with a 300 nm insulating layer of silicon oxide and pre-deposited gold electrodes. Directly after spin-coating, the substrates are transferred to a probe station connected to a parameter analyzer and electrical measurements are carried out under vacuum conditions.^[18]

The NC thin films are characterized in the dark and under illumination with a Schott ACE 150 Watt halogen AC powered light source with fiber optics. The bias voltage V_{ds} is swept between -5 V and +5 V.

After measuring the current-voltage curves of ETT capped NCs, the samples are transferred to an oven and heated to 260 °C for 90 minutes under oil pump vacuum. The annealed samples are kept under argon as they are prone to oxidation and transferred back to the probe station. The previously

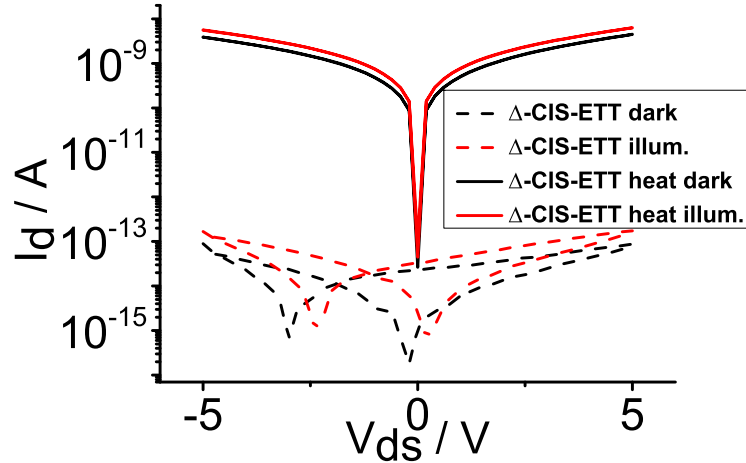


Figure 3.71: Current-voltage curves of trigonal pyramidal CIS-ETT NCs (Δ -CIS) at room temperature with a conductivity increase by 3.6 orders of magnitude after thermolysis of ETT.^[18]

characterized devices are measured again in the dark and under illumination. The conductivity of the samples is then calculated according to

$$\sigma = \frac{I_{ds}}{V_{ds}} \cdot \frac{L}{h \cdot W} \quad (3.2)$$

with $V_{ds} = +200$ mV, channel length $L = 300$ nm for trigonal pyramidal CIS, 350 nm for elongated CIS and CIGS, width $W = 14.5 \mu\text{m}$ and height h of the film ~ 20 nm for trigonal pyramidal CIS and ~ 40 nm for elongated CIS and CIGS films.^[18]

To determine the conductivities, three devices with each holding at least 80 measurable contacts are used. Figure 3.71 shows the current-voltage characteristics of a trigonal pyramidal CIS NC thin film (see Figure 3.72) prior to and after ETT thermolysis on the logarithmic scale.

Table 3.7 depicts the associated conductivities of trigonal pyramidal CIS NCs. Prior to ligand thermolysis, trigonal pyramidal CIS NCs exhibit a conductivity of 3.69×10^{-9} S/cm in the dark. These values are comparable to conductivities measured for trigonal pyramidal CIS NCs capped with the initial ligand OLA (see 3.9.3). After ETT thermolysis however, the NC film shows a 3.6 orders of magnitude enhanced electrical transport with a conductivity of 5.91×10^{-6} S/cm under illumination.

Elongated CIS NC films were characterized likewise, (see Figure 3.73 and 3.74 and table 3.8) exhibiting conductivities of 5.35×10^{-9} S/cm in the dark

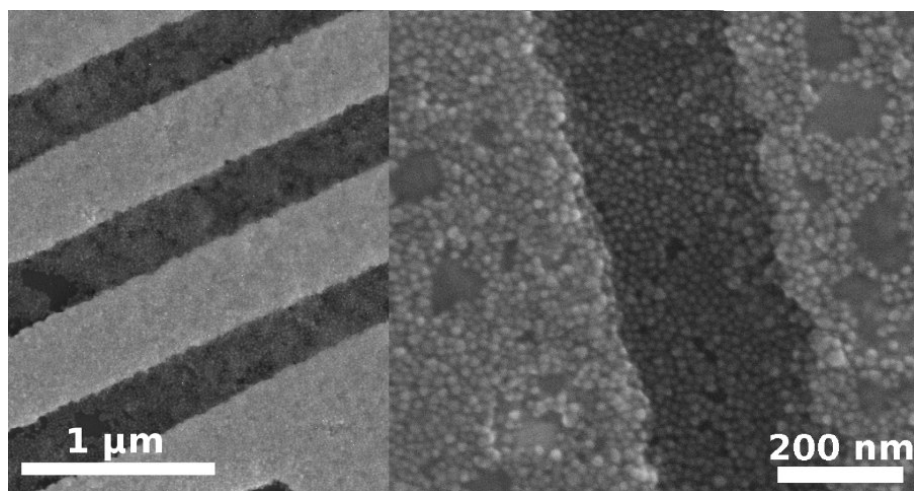


Figure 3.72: A densely packed quasi-monolayer of trigonal pyramidal CIS-ETT NCs (Δ -CIS).

σ [S/cm]	
Ligand	Δ -CIS
ETT	3.69×10^{-9}
ETT illum	4.63×10^{-9}
ETT heat	4.23×10^{-6}
ETT heat illum.	5.91×10^{-6}

Table 3.7: Conductivities of ETT capped trigonal pyramidal CIS NCs.

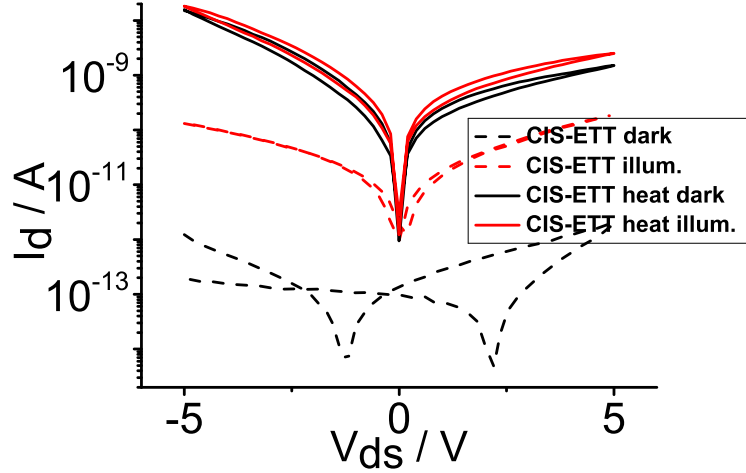


Figure 3.73: Current-voltage curves of elongated CIS-ETT NCs with a conductivity increase by 2.6 orders of magnitude after thermolysis of ETT.^[18]

prior to ligand thermolysis. The hysteresis in the current-voltage curves of ETT capped samples prior to the annealing step (see Figure 3.71, 3.73 and 3.75) originates from charging of the NC film when a bias voltage of -5 V to +5 V is applied. However, after annealing this effect is minimized once more underpinning the successful ligand-free state of the NC films.

Electrical transport in elongated ligand-free CIS NCs is enhanced by 2.6 orders of magnitude to conductivities of 2.05×10^{-6} S/cm under illumination (see Figure 3.74 for densely packed elongated CIS NC films).

In comparison with trigonal pyramidal NCs, it is apparent that the NC size plays a role in electrical transport of the CIS materials. Elongated CIS

σ [S/cm]	
Ligand	Elongated CIS
ETT	5.35×10^{-9}
ETT illum	7.53×10^{-8}
ETT heat	1.45×10^{-6}
ETT heat illum.	2.05×10^{-6}

Table 3.8: Conductivities of ETT capped elongated CIS NCs.

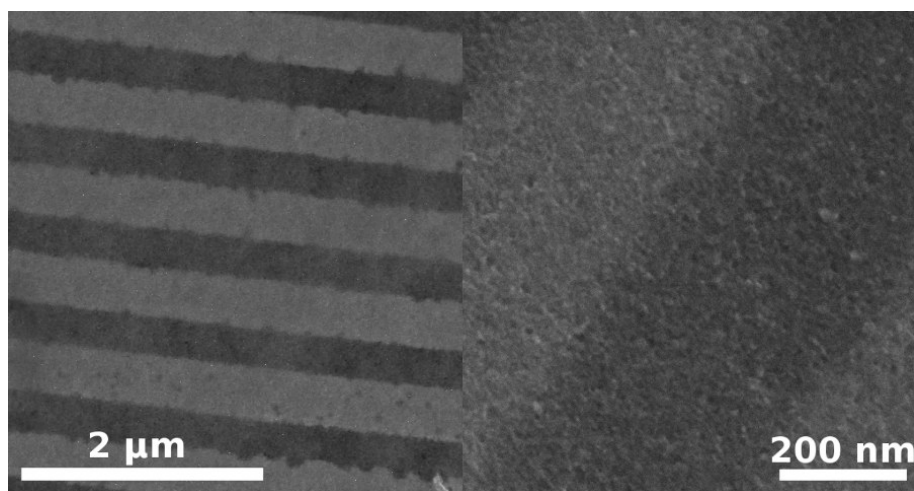


Figure 3.74: Elongated CIS-ETT NCs, densely packed film without cracks and holes over a long range.

NCs with an average size of 9 nm show one order of magnitude reduced conductivity compared to 19 nm sized trigonal pyramidal CIS NCs. Two factors are supposable for this behavior:

1. CI(G)S is a defect compound exhibiting many (surface) originating trap states^[111–113] that rise in importance when the surface-to-volume ratio in smaller NCs increases. Trap states can lead to charge carrier recombination and reduced electrical transport.^[114]
2. Charge carriers in smaller NCs have to overcome more grain boundaries to cross the channel length and will likely more often recombine. In addition, if looking at a NC film as a series of resistors with each (albeit infinitesimal) interparticle spacing representing one resistor, the more resistors you have, the larger will be the total resistance.

Figure 3.75 shows electrical transport of CIGS NC films (Figure 3.76) exhibiting conductivities of 1.21×10^{-8} S/cm in the dark prior to ligand thermolysis (see table 3.9). After annealing, the same devices show 1.8 orders of magnitude enhanced conductivity of 7.54×10^{-7} S/cm under illumination.

Here, again probably the higher number of surface originating trap states and grain boundaries in smaller NCs may lead to a lower conductivity.

All NC types show slight photoresponse after ligand thermolysis, whereas CIGS NCs exhibit the strongest effect (see Figure 3.77). The current measured at +5 V increases from 5×10^{-10} to 1×10^{-9} A (see Figure 3.77c), a

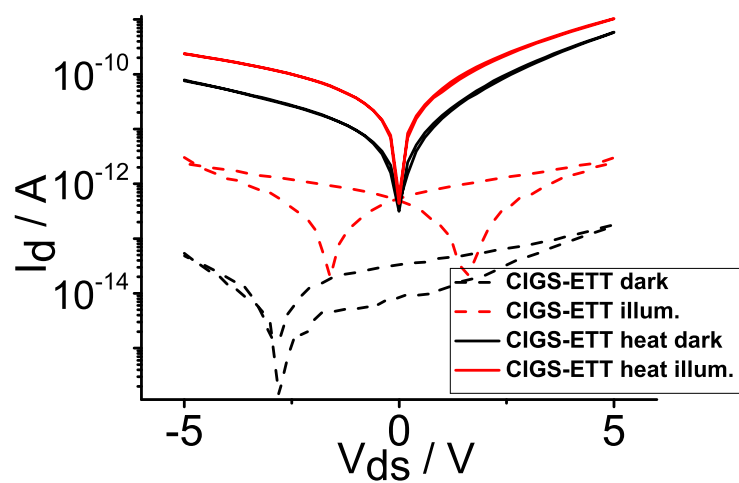


Figure 3.75: Current-voltage curves of ETT capped CIGS NCs with a conductivity increase by 1.8 orders of magnitude after thermolysis of ETT.^[18]

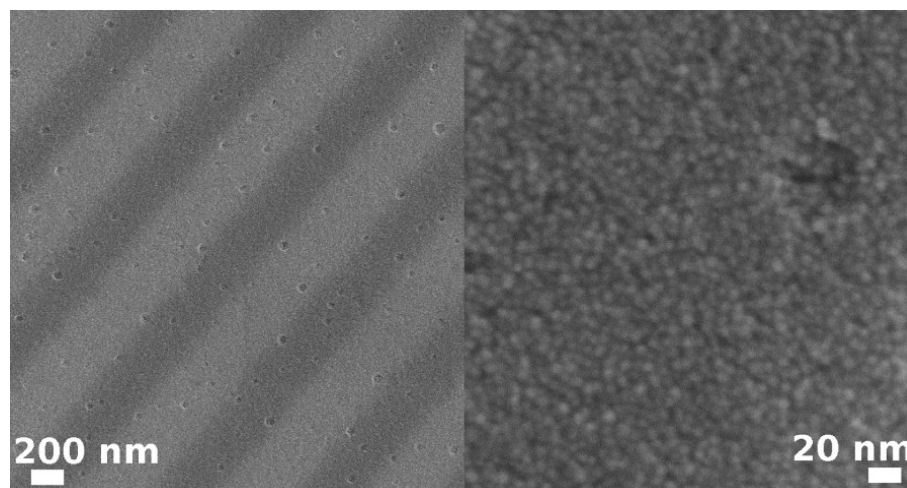
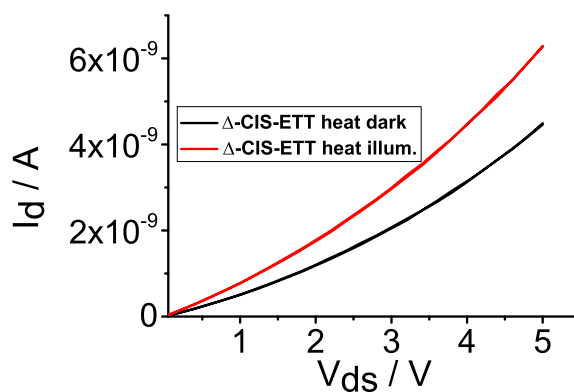


Figure 3.76: A densely packed film of CIGS-ETT NCs without cracks and deeper holes over a long range.

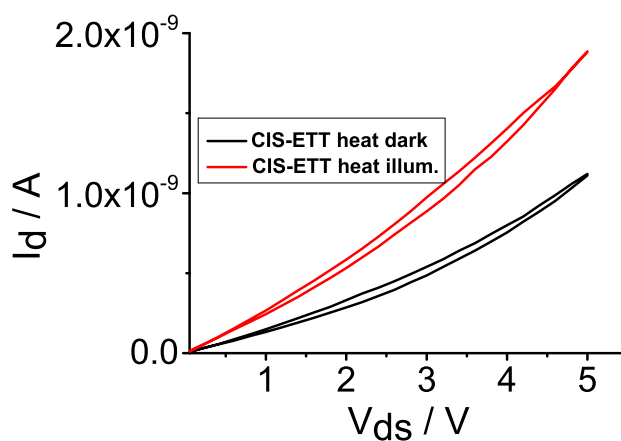
σ [S/cm]	
Ligand	CIGS
ETT	1.21×10^{-8}
ETT illum	1.78×10^{-7}
ETT heat	4.59×10^{-7}
ETT heat illum.	7.54×10^{-7}

Table 3.9: Conductivities of ETT capped CIGS NCs.

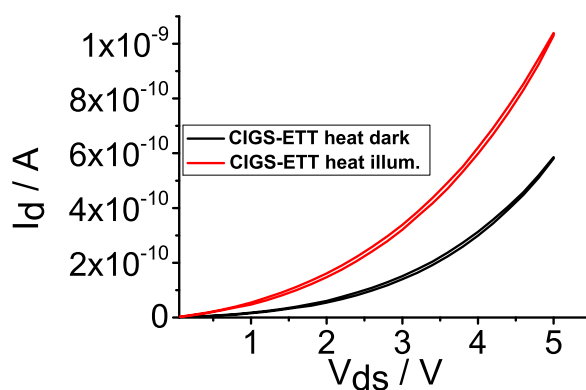
2 fold gain, when ligand-free NCs are illuminated by diffuse microscope light.



(a)



(b)



(c)

Figure 3.77: Photoresponse of ligand-free (a) trigonal pyramidal CIS (b) elongated CIS and (c) CIGS NCs.

σ [S/cm]			
Ligand	Δ -CIS	Elongated CIS	CIGS
MTT	5.54×10^{-9}	7.65×10^{-10}	1.06×10^{-9}
MTT illum	7.00×10^{-9}	7.65×10^{-10}	1.06×10^{-9}
MTT heat	3.15×10^{-6}	4.64×10^{-6}	4.56×10^{-6}
MTT heat illum.	3.50×10^{-6}	1.10×10^{-7}	6.22×10^{-6}

Table 3.10: Conductivities of MTT stabilized CI(G)S NCs.

3.9.2 MTT stabilized CuInSe_2 and $\text{CuIn}_{1-x}\text{Ga}_x\text{Se}_2$ NCs

Conductivity determination of MTT stabilized CI(G)S NCs supports the general benefit of thiotetrazole-based ligand exchanges for CI(G)S NCs.

The conductivities of MTT capped CI(G)S NC films lie in the same range as the conductivities determined for ETT capped samples (see table 3.10 and 3.12), showing that reducing the thiotetrazole unit by one $-\text{CH}_2$ group has no impact on the electrical transport performance of the ligand-free, closely assembled CI(G)S NC solids.

σ [S/cm]			
Ligand	Δ -CIS	Elongated CIS	CIGS
OLA	2.76×10^{-8}	2.68×10^{-7}	2.89×10^{-7}
OLA illum	3.46×10^{-8}	3.19×10^{-7}	4.74×10^{-7}
OLA heat	1.58×10^{-10}	1.51×10^{-6}	4.76×10^{-6}
OLA heat illum.	2.17×10^{-9}	1.83×10^{-6}	6.70×10^{-6}

Table 3.11: Conductivities of OLA stabilized CI(G)S NCs.

3.9.3 OLA stabilized CuInSe_2 and $\text{CuIn}_{1-x}\text{Ga}_x\text{Se}_2$ NCs

Conductivities of ETT and MTT exchanged CI(G)S NC solids are compared to conductivities of OLA capped CI(G)S NCs films. The electrical transport measurements are performed under ambient pressure and atmosphere.

Prior to the annealing step at 260 °C, OLA capped CI(G)S NCs exhibit conductivities higher than thiotetrazole stabilized NCs (see table 3.11). As electrical transport measurements of OLA capped CI(G)S NCs are conducted under ambient pressure in air, it is possible that effects caused by the reaction with oxygen lead to higher conductivities in OLA capped CI(G)S.

After annealing, conductivities of OLA capped elongated CIS and CI(G)S NCs increase due to carbonization effects known to set in when NCs are heated with long-chained hydrocarbon ligands (see 3.7.2).^[110]

The conductivities of ETT and MTT exchanged CI(G)S and OLA stabilized NCs prior to and after annealing in the dark and under illumination are summarized in table 3.12.

In conclusion, the formation of virtually bare CI(G)S NCs by thermolyzing ETT and MTT leads to improved electrical transport in closely assembled NC solids depending on the size and surface trap number and density in the NCs.

It is shown that annealing of OLA capped CI(G)S leads to carbonization of the NC films, representing a detrimental effect for the semiconducting properties of the CI(G)S and leading to impracticality for their use in semiconductor-related technologies like LEDs, photodetectors or transistors.

The application of ETT as ligand is superior as it leads to the possibility to determine the electrical transport of ligand-free CI(G)S NCs and to sinter CI(G)S NCs to close crystalline assemblies which is not possible with OLA capped CI(G)S NCs.

σ [S/cm]			
Ligand	Δ -CIS	Elongated CIS	CIGS
ETT	3.69×10^{-9}	5.35×10^{-9}	1.21×10^{-8}
ETT illum	4.63×10^{-9}	7.53×10^{-8}	1.78×10^{-7}
ETT heat	4.23×10^{-6}	1.45×10^{-6}	4.59×10^{-7}
ETT heat illum.	5.91×10^{-6}	2.05×10^{-6}	7.54×10^{-7}
MTT	5.54×10^{-9}	7.65×10^{-10}	1.06×10^{-9}
MTT illum	7.00×10^{-9}	7.65×10^{-10}	1.06×10^{-9}
MTT heat	3.15×10^{-6}	4.64×10^{-6}	4.56×10^{-6}
MTT heat illum.	3.50×10^{-6}	1.10×10^{-7}	6.22×10^{-6}
OLA	2.76×10^{-8}	2.68×10^{-7}	2.89×10^{-7}
OLA illum	3.46×10^{-8}	3.19×10^{-7}	4.74×10^{-7}
OLA heat	1.58×10^{-10}	1.51×10^{-6}	4.76×10^{-6}
OLA heat illum.	2.17×10^{-9}	1.83×10^{-6}	6.70×10^{-6}

Table 3.12: Conductivities of ETT and MTT exchanged and initially OLA stabilized CI(G)S NCs for comparison; it is possible that the reaction with oxygen leads to improved conductivities of OLA capped CI(G)S NCs in comparison with ETT and MTT capped CI(G)S samples prior to annealing.

Indium Selenide Sheets - Ensemble		
Element	Atom%	Error
Se (Ref.) L*	69.54	0.03
In L*	30.46	0.04

Table 3.13: EDS of multiple In_xSe_y nanosheets in atom%.

3.10 2D Indium Selenide Nanosheets

Determining and describing the synthesis effects leading to the formation of hexagonal two-dimensional In_xSe_y nanosheets is still underexplored.

Investigation of different reaction attributes in In_xSe_y nanosheets at the moment lead to the assumption that the two-dimensional structures' formation mechanism is based on *aggregative* growth and associated *oriented attachment* processes (see 2.2 and 2.6).

Furthermore, it is assumed that the formation of hexagonal indium selenide nanosheets can be described by a model of Hayashi *et al.* who report the formation of either hexagonal or trigonal InSe, depending on the selenium ratio in reaction (see 2.6).^[75,76]

If a high selenium amount is present, hexagonally shaped InSe is formed in contrast to trigonally formed InSe structures when the selenium amount is decreased.^[75]

The indium and selenium precursors in our case are templated by the stabilizer and co-solvent octadecylamine (ODA, exchange from OLA to ODA). The compound is solid at room temperature and dissolves at temperatures in the range of 75 °C.

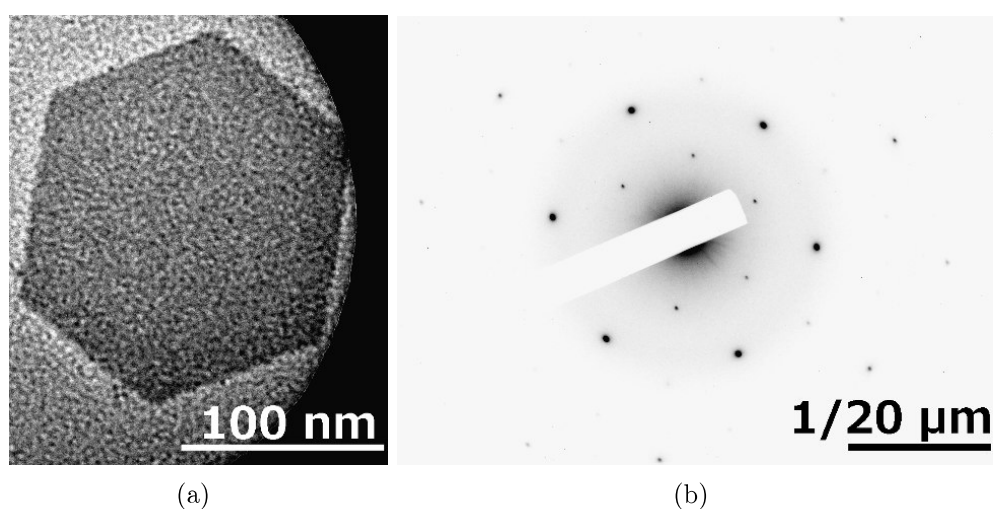
In the case of the In_xSe_y nanosheets, most likely small primary In_xSe_y NCs are assembled *via oriented attachment* into their final hexagonal or trigonal structure.^[15]

It is important to note that a stoichiometrical amount of indium to selenium precursor in reactions fails in the formation of two-dimensional In_xSe_y nanosheets.

The stoichiometry of the obtained In_xSe_y structures clearly deviates from the stoichiometry described for hexagonal InSe. EDS shows that the material exhibits an indium to selenium ratio of roughly 1:2 (see table 3.13 and table 3.14 for a single sheet).

Figure 3.78a depicts a TEM image of a typical In_xSe_y nanosheet with a hexagonal crystal system shown by the SAED of the structure (see Figure 3.78b) and pointing in the direction of the hexagonal InSe stoichiometry.

Single Indium Selenide Sheet		
Element	Atom%	Error
Se (Ref.) L*	58.72	0.28
In L*	41.28	0.29

Table 3.14: EDS of a single In_xSe_y nanosheet in atom%.Figure 3.78: (a) Single In_xSe_y nanosheet and (b) associated SAED elucidating a hexagonal crystal structure.

This assumption is supported by the SEM images in Figure 3.83 on page 107. Here, a film of In_xSe_y sheets is depicted, showing big bright spheres which most likely originate from elemental selenium accumulating on the nanosheets.

The reason for the formation of elemental selenium is that it has to be used in excess for reaction. The formed elemental selenium spheres are also detected in EDS and may lead to the stoichiometry deviation. However, as indium selenide exists in various stoichiometries and phases, the formation of a mixed phase in In_xSe_y nanosheets cannot be excluded (see section 2.6).

The formation mechanism for In_xSe_y nanosheets' hexagonal or trigonal shape is tested by modifying the reaction conditions. Hexagonal sheets are formed at an early stage of reaction when the selenium to indium ratio is balanced^[75] and are depicted in Figure 3.79 after 5 minutes at 240 °C.

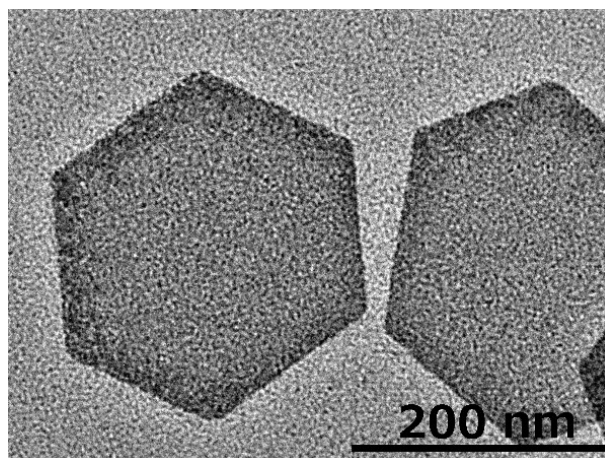


Figure 3.79: In_xSe_y nanosheets synthesized for 5 min at 240 °C and showing a hexagonal structure.

In the time range of 5 minutes to 60 minutes, the structure of the In_xSe_y nanosheets transfers from a hexagonal to a more trigonal one. This can be explained by the amount of selenium available for incorporation into the nanosheets. As the reaction proceeds, excess elemental selenium is not further incorporated into hexagonal In_xSe_y nanosheets but accumulates on the formed structures (see Figure 3.83 and 3.84 on page 107). In_xSe_y nanosheets further grow in trigonal direction (see Figure 3.82 on page 107).

As previously described by Dogan *et al.*, it is possible to contact single semiconductor PbS nanosheets and determine their electrical transport properties.^[115] Such two-dimensional quantum well structures exhibit entirely different properties from films of assembled quantum dots of which enhanced electrical transport is only one advantage.^[116]

Similar enhancements are to be expected in the case of In_xSe_y nanosheets as described in the present work, provided the size of an average sheet can be increased such that contacting with suitable electrodes becomes possible.

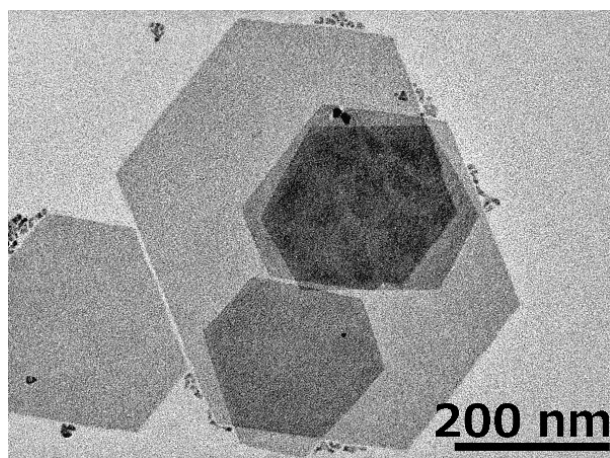


Figure 3.80: In_xSe_y nanosheets synthesized for 15 min at 240 °C, slightly losing the hexagonal shape.

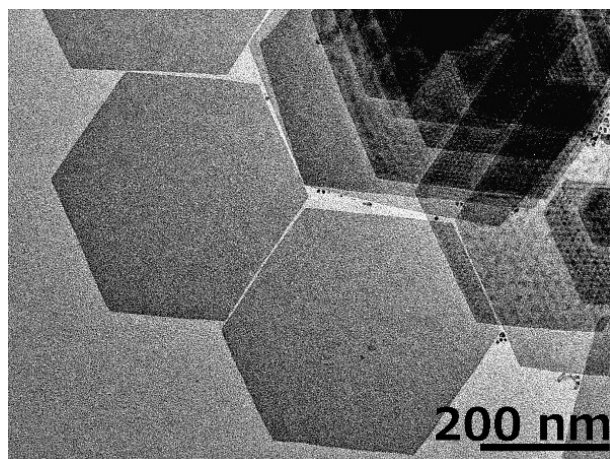


Figure 3.81: In_xSe_y nanosheets synthesized for 30 min at 240 °C, a mix of hexagonal and trigonal structures.

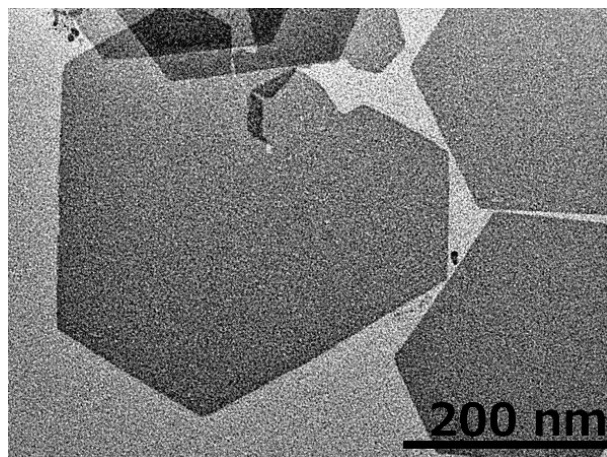


Figure 3.82: In_xSe_y nanosheets synthesized for 60 min at 240 °C with a rather trigonal structure.

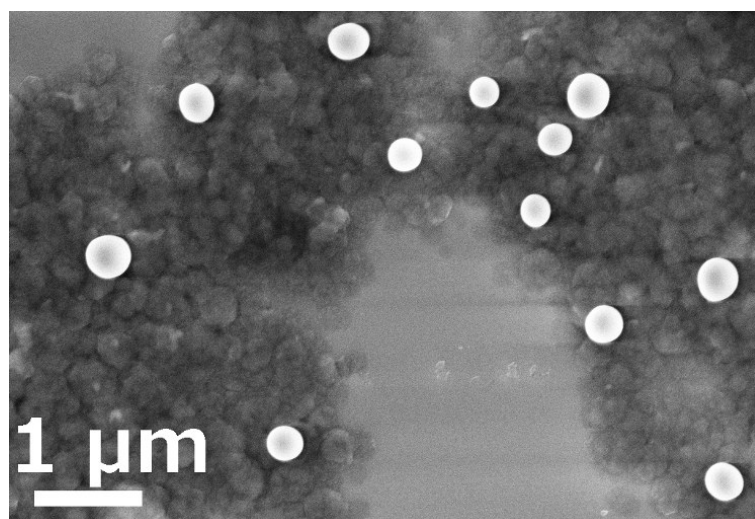


Figure 3.83: A film of In_xSe_y nanosheets with a high amount of elemental selenium accumulating as spheres on the film.

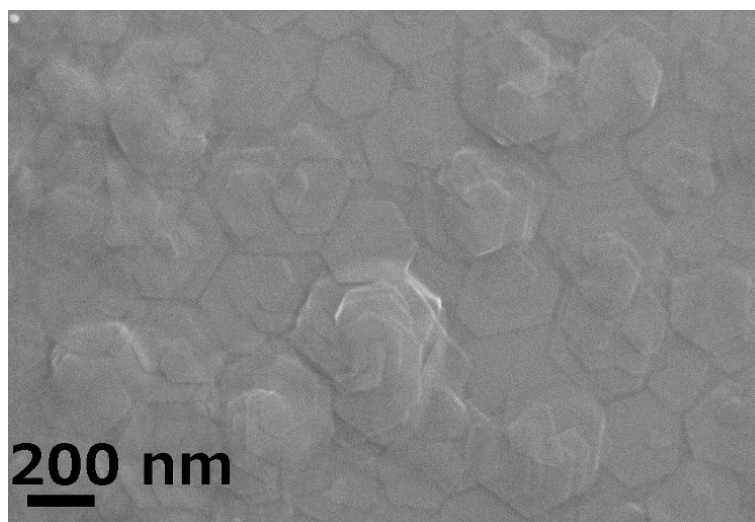


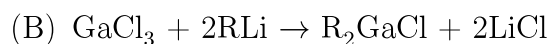
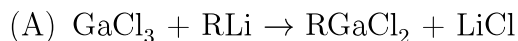
Figure 3.84: A film of In_xSe_y nanosheets from a lower concentrated solution, exhibiting less accumulated selenium on the film.

3.11 Gallium Arsenide Nanocrystals

A novel simple wet-chemical way to obtain rather monodisperse GaAs NCs (8.4 nm) in a three-step formation is presented. The described transmetalation reaction pathway offers an effective way to obtain high quality GaAs NCs in terms of size distribution and crystallinity. The precursors used for reaction are low-cost reactants with a moderate toxicity, offering a cost-effective way to obtain the desired materials. The presented solution-processed synthesis route significantly broadens the scope of possible applications for GaAs and other III-V semiconductor NCs.^[12]

3.11.1 Three-step Formation of III-V Nanocrystals

The general reaction path for the synthesis of III-V NCs is discussed exemplarily for GaAs. The formation of GaAs NCs using *n*-butyllithium as a reduction reagent occurs in three steps. Every NC reaction starts with a transmetalation taking place, when GaCl₃ reacts with *n*-butyllithium at elevated reaction temperatures. Herein, three intermediate products have been reported (see equation A-C). Note that diverse fragmentation modes are possible for R_{*n*}GaCl_{3-*n*} compounds.^[117,118]



The degree of substituted halide ligands in the particular metal salt depends on the molar ratio of *n*-butyllithium to the corresponding halide used for reaction. All three transition states are likely to coexist, although they are not isolated during reaction. The metal alkyl compounds decompose to form elemental gallium which subsequently reacts with Mg₃As₂ to form GaAs NCs as schematically described in Figure 3.85. Figure 3.86 shows TEM images of crystalline and rather monodisperse GaAs NCs obtained in a typical synthesis with GaCl₃ as precursor. The particles have an average size of 8.4 nm (± 1.7 nm) in diameter. The crystal phase of the NCs is characterized by SAED shown in Figure 3.86B and powder XRD (see Figure 3.87A).

The SAED shows the characteristic pattern of the cubic phase (F- $\bar{4}3m$) of GaAs with the corresponding lattice spacing of 3.27 Å [111], 2.00 Å [220] and 1.71 Å [311]. EDS confirms the composition of the material is gallium and arsenic nearly 1:1 with a slight gallium excess (see Figure 3.88).

The samples for powder XRD measurements are precipitated several times to remove residues of unconverted Mg₃As₂ and by-products like MgO, which

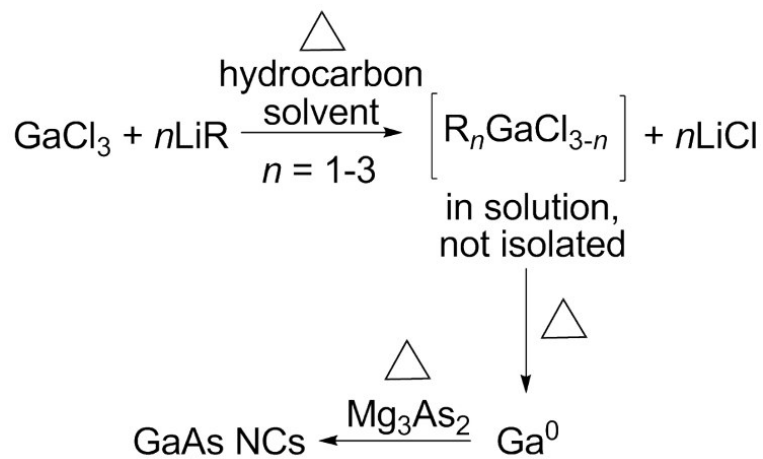


Figure 3.85: Transmetalation reaction of GaCl₃ resulting in elemental gallium at elevated temperatures and in GaAs NCs after reaction with Mg₃As₂.

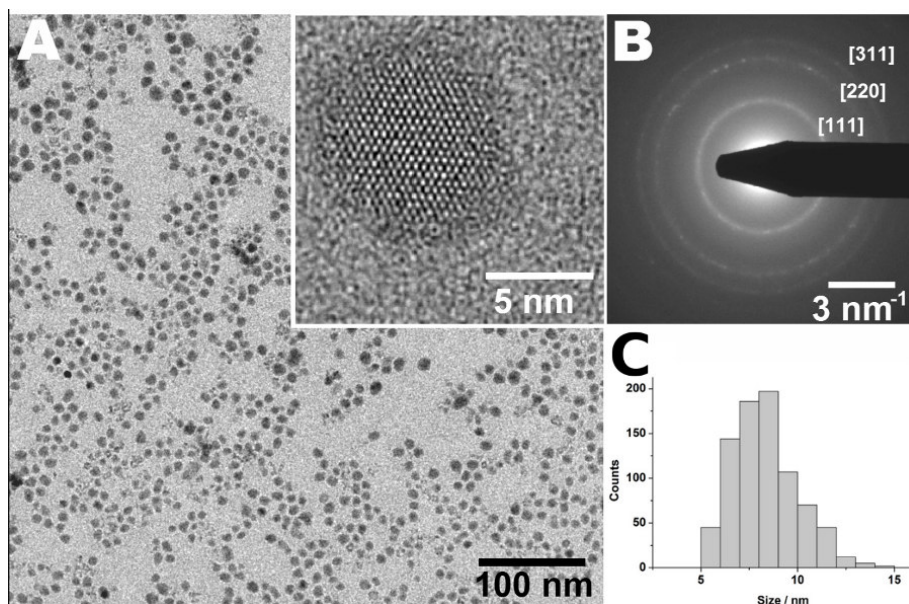


Figure 3.86: TEM image of crystalline GaAs particles and inset of a single NC (A), corresponding SAED (B) and a histogram of NC size distribution.

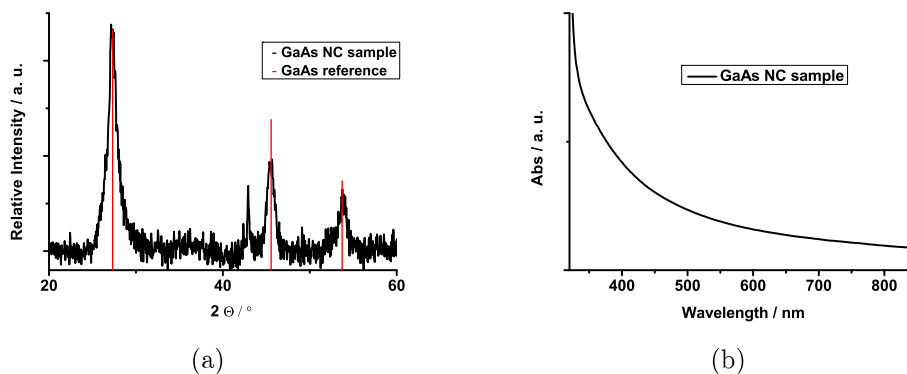


Figure 3.87: (a) Powder XRD pattern of GaAs NCs, vertical lines below indicate corresponding bulk GaAs reflexes, (b) UV-Vis absorption spectrum of a typical GaAs NC synthesis taken after 1 h of reaction time.

forms in the course of the NC purification from elemental magnesium. A small amount of elemental magnesium is formed during the reaction, because of the reductive conditions supplied by *n*-butyllithium addition. All reflexes correspond to the common face-centered cubic (fcc) structure of GaAs (JCPDS # 00-080-16).

Distinctive absorption edges in the absorption spectrum of a typical GaAs NC synthesis shown in Figure 3.87B are absent. This result is in qualitative agreement with observations made by Butler *et al.* who describe that absorption features in GaAs are only observable for NCs with sizes less than or equal to 4 nm and who attribute these features to discrete electron transitions in the material.^[91] When exceeding sizes of 4 nm, GaAs NCs lack of spectral features like similarly examined by Byrne *et al.*^[119] and Sandroff *et al.*^[120]

A possible reason for the absence of absorption features in GaAs NCs might be the low exciton ‘binding energy’ in the material (0.007 eV).^[91,121] This would mean that absorption features can only be observable at temperatures of 80 K and lower.^[12]

3.11.2 Molecular Gallium to Arsenic Ratio in the Reaction

An important factor in the GaAs NC synthesis is the molar ratio of the gallium and arsenic precursors. Best crystalline GaAs NCs with smallest size distribution are obtained with a gallium to arsenic ratio of 1:2.

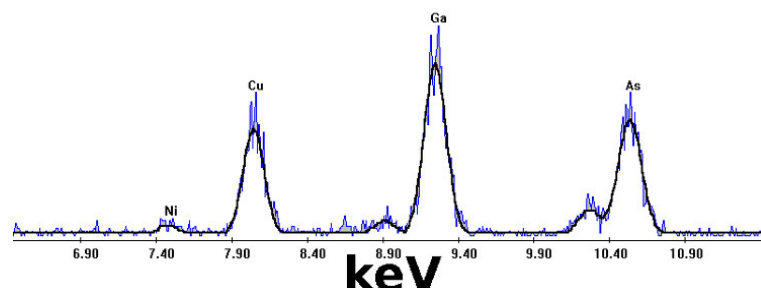


Figure 3.88: EDS of GaAs NCs, performed on a copper grid.

A stoichiometrical gallium to arsenic ratio of 1:1 leads to a broader size distribution of the NCs with additional gallium spheres in the reaction mixture. A gallium excess (Ga:As ratio of 2:1) leads to a sediment of bulk material composed of GaAs and undefined by-products.

Only if the formation rate of elemental gallium is adjusted with the reactivity of the arsenic source Mg_3As_2 at temperatures of 300 °C, NCs are obtained. If the concentration of elemental gallium in solution is too high, the arsenic source is not able to react with all the gallium available for reaction which results in the formation of elemental gallium spheres.

If the release of elemental gallium in solution is too low, the reaction yields amorphous GaAs agglomerates.^[12]

3.11.3 Reactivity of Gallium(III) Halides and HSAB Principle

Using the different gallium(III) halides GaF_3 , GaCl_3 , GaBr_3 and GaI_3 as precursors for the GaAs synthesis clearly shows the dependency of the sizes, size distribution and morphology of the NCs on the different precursors.

In good correlation with the *Hard and Soft Acids and Bases* (HSAB) principle introduced by Pearson, the leaving group ability of the gallium(III) halides enhances from fluoride over chloride and bromide to iodide, the bigger the halide, the better its ability to stabilize a negative charge.^[97,98] This ability leads to the assumption that elemental gallium available for the NC reaction is formed the slowest from GaF_3 and the fastest from GaI_3 . Figure 3.89 shows the syntheses results with GaCl_3 (A), GaBr_3 (B) and GaI_3 (C) as gallium precursors.

The formation of GaAs NCs fails using GaF_3 as a precursor. The average size of GaAs NCs in Figure 3.86A and 3.89A is 8.4 nm (± 1.7 nm) in diameter.

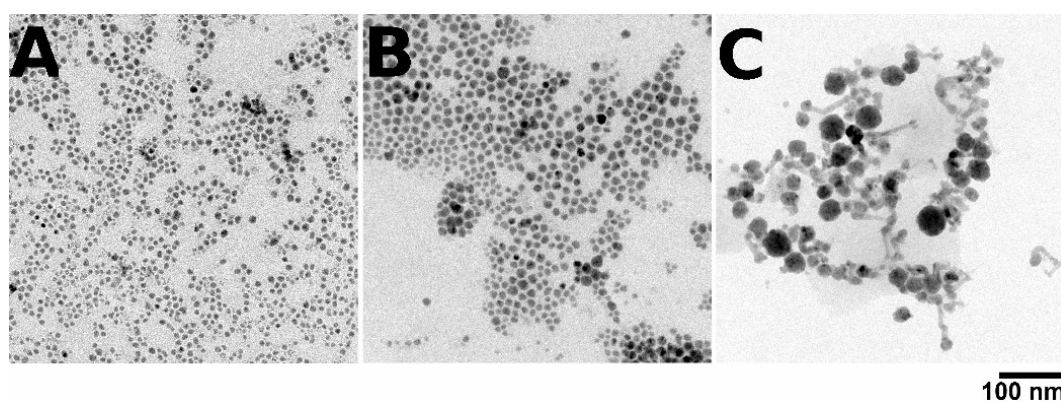


Figure 3.89: GaCl₃ (A), GaBr₃ (B) and GaI₃ (C) as gallium precursor for the reaction.

GaAs NCs obtained with GaBr₃ as precursor are slightly bigger, showing an average size of 11.6 nm (± 2.8 nm, see Figure 3.89B).

Polycrystalline structures of different morphologies like elemental gallium spheres, GaAs nanoneedles and NCs were obtained by using GaI₃ as precursor (see Figure 3.89C).^[12]

3.11.4 GaAs Synthesis Reaction Temperature

The influence of the reaction temperature on GaAs NC syntheses is tested for 250 °C, 270 °C, 300 °C and 315 °C. Best results are achieved at a reaction temperature of 315 °C. Below 300 °C, the reaction mixtures turn turbid gray, indicating the formation of elemental, macro sized gallium with diameters of several hundred nanometers.

3.11.5 Applicability of the Transmetalation Reaction

The transmetalation reaction and the subsequent formation of NCs from elemental gallium or indium formed within this process is tested for a variety of different III-V semiconductor NCs. InP NCs with sizes of 8.7 nm (± 1.9 nm) depending on the indium precursor are synthesized.

InAs NCs with sizes of 15.7 nm (± 4.3 nm) are successfully synthesized and for the first time it is possible to obtain GaP NCs (see Figure 3.90).

For further information and experiments the reader is forwarded to the corresponding reference of Lauth *et al.*^[12]

A novel simple wet-chemical way to obtain rather monodisperse GaAs NCs (8.4 nm) in a three-step formation is presented. The described transmeta-

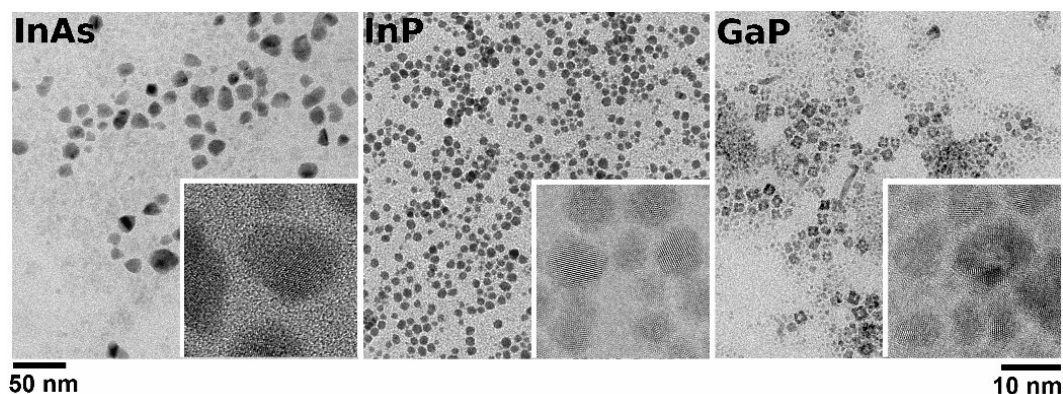


Figure 3.90: InAs, InP and GaP NCs synthesized *via* the transmetalation method.

lation reaction pathway offers an effective way to obtain high quality GaAs NCs in terms of size distribution and crystallinity.

InP NCs (8.7 nm) are synthesized, that, to the best of our knowledge, show the best size distribution for bigger sized InP NCs up to now.

The principle of the transmetalation reaction pathway is extended to InAs NCs, which tend to show bigger average sizes (15.7 nm) than most commonly synthesized InAs NCs from $(\text{TMS})_3\text{As}$ as precursor.

First experiments in obtaining GaP NCs are made, showing the universal use of the transmetalation reaction.

The precursors used for reaction are low-cost reactants with a moderate toxicity, offering a cost-effective way to obtain the desired materials. The presented solution-processed synthesis route significantly broadens the scope of possible applications for GaAs and other III-V semiconductor NCs.

4 Summary

This work is based on the comprehensive analysis of CuIn(Ga)Se₂ NCs with regard to their applicability towards optoelectronic NC solids.

Wet-chemical syntheses approaches are modified and enhanced, thereby emphasizing the importance of well-balanced precursor combination and reaction conditions to obtain CI(G)S NCs with high quality in terms of crystallinity, reproducibility and size distribution. The obtained materials are further utilized for ligand exchange reactions and determination of their electrical transport properties.

A wet-chemical ligand exchange procedure for the processed CI(G)S NCs with 1-ethyl-5-thiotetrazole is established and the exchange is monitored by *Attenuated Total Reflectance Fourier Transformation Infrared Spectroscopy*, *Thermogravimetric Analysis* and *X-ray Photoelectron Spectroscopy*.

The ligand exchanged CI(G)S NCs are used to compare their suitability for solution-processed, ligand-free NC solids with enhanced electrical transport properties. It is proven that electrical transport in CI(G)S NC solids is significantly enhanced after the ligand thermolysis. The reason for the enhanced electrical transport is the reduced interparticle distance in ligand exchanged and ligand-free CI(G)S NC solids which leads to improved coupling of the CI(G)S NCs and is characterized by *Transmission Electron Microscopy*, *X-ray Diffraction* and *Small Angle X-ray Scattering*.

In-situ Transmission Electron Microscopy and *X-ray Diffraction* heating experiments reveal the unique suitability of the described method: The possibility to sinter virtually bare CI(G)S NCs without detrimental organic residues. This property, for the first time, offers the possibility to process ligand-free NC surfaces by a wet-chemical method.

This work describes the possibilities for CI(G)S NCs, starting with the reproducible processing of the materials in high quality to the subsequent functionalization of the NCs to determine their electrical transport properties.

It is intended to act as starting point for utilizing the materials in photovoltaics.

Furthermore, first synthesis and characterization steps for two-dimensional In_xSe_y nanosheets are carried out by omitting the copper reactant from

CI(G)S synthesis and slightly varying the reaction conditions. Pursuing control over the size of the nanosheets with a multiphase and multicrystal system like indium selenide will lead to the possibility to characterize the electrical transport properties of the nanosheets.

To elucidate the reaction pathways of CuIn(Ga)Se_2 related compounds including III-V semiconductors, synthetic routes for III-V NCs, mainly GaAs, are established.

The presented transmetalation reaction pathway offers the possibility to process the most common III-V NCs: GaAs, InP, InAs and GaP.

This work shows that by carefully probing and adjusting the reaction conditions and behavior of the different elements in the investigated compounds, complicated I-III-VI₂ and III-V semiconductor NCs can be rationally synthesized to allow access to promising functional materials for regenerative energy conversion.

Zusammenfassung

Die vorliegende Arbeit basiert auf der eingehenden und fundierten Analyse von CuIn(Ga)Se_2 Nanokristallen hinsichtlich ihrer Nutzung als optoelektronische Nanokristall Festkörper.

Nasschemische Syntheserouten werden hierfür modifiziert und verbessert und unterstreichen dabei die Bedeutsamkeit von ausgewogener Vorstufenkombination und angepassten Reaktionsbedingungen, um qualitativ hochwertige Nanokristalle zu erhalten, welche kristallin, eng größenverteilt und reproduzierbar herzustellen sind. Diese Nanokristalle werden für weiterführende Zwecke wie den Ligandenaustausch und die Charakterisierung ihrer elektrischen Transporteigenschaften verwendet.

Ein Ligandenaustauschprozess für die hergestellten CI(G)S Nanokristalle wird etabliert und mithilfe von *Attenuated Total Reflectance Fourier Transformation Infrared Spectroscopy*, *Thermogravimetric Analysis* und *X-ray Photoelectron Spectroscopy* untersucht. Die ausgetauschten CI(G)S Nanokristalle werden auf ihre Eignung als nasschemisch hergestellte, liganden-freie Nanokristalle mit verbesserten elektrischen Transporteigenschaften untersucht.

Es wird nachgewiesen, dass sich der elektrische Transport in CI(G)S Nanokristallen nach der Ligandenthermolyse signifikant verbessert. Hierfür ist die Abnahme des Interpartikelabstandes verantwortlich, welcher zu verbesserter Kopplung der Nanokristalle führt und durch weitreichende *Transmission Electron Microscopy* und *X-ray Diffraction* Analysen und *Small Angle X-ray Scattering* Messungen charakterisiert wird.

In-situ Transmission Electron Microscopy und *X-ray Diffraction* Heizexperimente unterstreichen die einzigartige Eignung der beschriebenen Methode: Die Möglichkeit, quasi-freie Nanokristalle ohne nachteilige Einschlüsse von organischen Resten zu dünnen kristallinen Festkörpern zu sintern. Diese Eigenschaft ermöglicht es erstmals mithilfe eines einfachen nasschemischen Weges, ligandenfreie Nanokristalloberflächen zu erhalten.

Die vorliegende Arbeit beschreibt die Möglichkeiten eines hoch interessanten und nützlichen Materials, von der reproduzierbaren Herstellung in hoher Qualität, über die Funktionalisierung der Nanokristalle, bis hin zur Anwendung der neu herausgearbeiteten Materialeigenschaften. Sie soll als Ausgangspunkt für die Nutzbarmachung des Materials in der Photovoltaik dienen.

Weiterhin werden die Synthese und erste Charakterisierungsschritte für interessante zweidimensionale In_xSe_y *Nanosheets* beschrieben, welche sich durch die leichte Variation der CI(G)S Synthesebedingungen und Ausschließen von Kupfer als Reaktanden herstellen lassen. Die weiterführende Kontrolle über die Größe der *Nanosheets* mit Indiumselenid als multikristallinem und -phasigem System wird die Charakterisierung der elektrischen Transporteigenschaften dieser interessanten dünn-schichtigen Strukturen ermöglichen.

Um die möglichen Reaktionswege von $\text{CuIn}(\text{Ga})\text{Se}_2$ -ähnlichen Verbindungen zu beleuchten, werden Syntheserouten für III-V Halbleiter Nanokristalle, hauptsächlich GaAs, etabliert.

Der dargestellte Transmetallierungsweg ermöglicht die Herstellung der gängigsten III-V Halbleiter: GaAs, InP, InAs und GaP.

Die vorliegende Arbeit zeigt, dass es durch die fundierte Untersuchung und Anpassung der Reaktionsbedingungen der untersuchten Substanzen möglich ist, komplizierte I-III-VI₂ and III-V Halbleiter Nanokristalle zu erzeugen und zu kontrollieren, die vielversprechene Materialien für regenerative Energieansätze darstellen.

5 Experimental

Unless stated otherwise all synthetic steps were carried out using standard SCHLENK-line techniques under nitrogen as inert gas or inside a nitrogen filled glovebox.

5.1 CuInSe₂ and CuIn_{1-x}Ga_xSe₂ NC Syntheses

5.1.1 Trigonal pyramidal CuInSe₂

Trigonal pyramidal CIS NCs were synthesized according to a method of Koo *et al.*^[95] In a typical synthesis of 19 nm NCs, 0.50 mmol (50 mg) copper(I) chloride were mixed with 0.500 mmol (111 mg) indium(III) chloride inside a glovebox in a 25 mL threenecked flask equipped with a septum and thermocouple. 10 mL OLA were added to the components and the solution marked A. The flask was connected to a condenser under nitrogen flow outside of the glovebox.

In a separate 5 mL threenecked flask likewise equipped with septum, thermocouple and condenser, 1.00 mmol (123 mg) selenourea were mixed with 1 mL OLA and marked solution B. Solution A was kept stirring under oil pump vacuum at 60 °C for one hour whereas solution B was stirred under nitrogen flow. After one hour solution A was set under nitrogen, heated to 130 °C for 10 minutes and subsequently cooled to 100 °C.

Solution B meanwhile was heated to 210 °C to dissolve the reactant and set free selenium species for reaction. Subsequently it was cooled to 110 °C, transferred by syringe and rapidly injected into solution A. The reaction mixture was then heated to 240 °C with a rate of 15 °C/min.

After one hour of reaction time the suspension was cooled to room temperature. 30 mL of ethanol were added to the crude product to precipitate the NCs. The mixture was centrifuged at 4000 rpm for 4 minutes. The colorless supernatant was discarded and the NCs redissolved in 5 mL chloroform. After centrifugation of this solution at 4000 rpm for 5 minutes, the NC product in the deep black supernatant was separated from sediment which contained poorly capped NCs. The reaction typically yielded ~50 % purified NCs.

Characterization and ligand exchange were conducted with the purified NCs from the supernatant.^[18]

5.1.2 Elongated CuInSe_2

Elongated CIS NCs were synthesized based on a method by Panthani *et al.*^[19] A typical synthesis included 0.50 mmol (61 mg) copper(I) acetate, 0.500 mmol (111 mg) indium(III) chloride and 1.00 mmol (123 mg) selenourea mixed in a 25 mL threenecked flask and combined with 10 mL OLA. The reaction solution was kept under oil pump vacuum at 60 °C for one hour, then set under nitrogen and stirred for another hour at 110 °C. Subsequently the mixture was heated to 240 °C and kept at this temperature for one hour.

Afterwards, the solution was cooled to room temperature. For purification and additional stabilization of the NC product, 4 mL of a TOP/toluene mixture (TOP/Tol 3:1) were added to the crude product. The solution was vortexed and centrifuged at 4500 rpm for 5 minutes to remove poorly capped NCs. The supernatant was separated from the sediment and 30 mL 2-propanol were added for precipitation. The mixture was centrifuged at 10000 rpm for 15 minutes. The NC product was redissolved in 5 mL chloroform and filtered with a 0.2 μm hydrophobic syringe filter. 15 mL of a methanol/2-propanol solution (4:1) were added and the mixture centrifuged at 10000 rpm for 5 minutes.

The reaction typically yielded ~25 % purified NCs which were redissolved in chloroform and used for characterization and ligand exchange.^[18]

5.1.3 $\text{CuIn}_{1-x}\text{Ga}_x\text{Se}_2$

CIGS NCs were synthesized based on a method by Panthani *et al.*^[19] In a typical one-pot synthesis, 0.10 mmol (12 mg) copper(I) acetate, 0.10 mmol (22 mg) indium(III) chloride, 0.10 mmol (45 mg) gallium(III) iodide and 0.20 mmol (25 mg) selenourea were mixed in a 25 mL threenecked flask and 10 mL OLA were added. The reaction mixture was stirred at 60 °C under oil pump vacuum, then set under nitrogen and stirred at 110 °C for an additional hour and subsequently heated to 240 °C for one hour for reaction.

Afterwards, the solution was allowed to cool to room temperature. For purification and additional stabilization of the NC product, 4 mL of TOP/Tol (3:1) were added to the crude product. The solution was vortexed and centrifuged at 5600 rpm for 5 minutes to remove poorly capped NCs. The supernatant was separated and 25 mL 2-propanol were added for precipitation. The mixture was centrifuged at 10000 rpm for 15 minutes. The NCs

5 *Experimental*

were redissolved in 2 mL chloroform and filtered with a 0.2 μm hydrophobic syringe filter.

The reaction typically yielded $\sim 60\%$ NCs.^[18]

5.2 Choice of Selenium Precursors

CI(G)S NC syntheses were conducted with different selenium precursors to probe their use as efficient reactant with the different copper(I)-, indium(III)- and gallium(III)-precursors. The vast majority of the experiments was conducted with selenourea as selenium source as it turned out to be the most effective selenium reagent for the investigated purpose (see 3.4).

5.2.1 Elemental Selenium

A Panthani *et al.* based CIS synthesis attempt with elemental selenium as precursor^[19] involved the combination of 122 mg (1.00 mmol) copper(I) acetate, 221 mg (1.00 mmol) indium(III) chloride and 158 mg (2.00 mmol) selenium powder in a 25 mL threenecked flask. The reaction mixture was stirred for one hour under oil pump vacuum at 60-75 °C and was subsequently set under nitrogen at 110 °C for 90 minutes. The reaction temperature then was set to 240 °C and the reaction was stirred for 4 hours after reaching this temperature.

Afterwards, the reaction mixture was cooled to room temperature and precipitated three times with acetone. The mixture was centrifuged at 4500 rpm for 5 minutes after the particular precipitation step and the sediment was separated and redissolved in toluene. The colorless supernatant was discarded.

The obtained CIS NCs were dissolved in toluene for characterization.

5.2.2 Bis(trimethylsilyl)selenide

0.50 mmol (61 mg) copper(I) acetate and 0.50 mmol (111 mg) indium(III) chloride were mixed with 10 mL OLA inside the glovebox and set under oilpump vacuum at 60 °C for 60 minutes. Subsequently, the mixture was set to 110 °C for 60 minutes. After one hour, 1.0 mmol (TMS)₂Se were added rapidly to the reaction mixture and the temperature was set to 240 °C. The reaction mixture was stirred for one hour at this temperature and then slowly cooled to room temperature.

Purification of the NC product involved transferring the reaction mixture out of the glovebox and additional stabilization of the NC product with 4 mL of TOP/Tol (3:1). The solution was vortexed and centrifuged at 5600 rpm for 5 minutes to remove poorly capped NCs. The supernatant was separated and 25 mL 2-propanol were added for precipitation. The mixture was centrifuged at 10000 rpm for 15 minutes.

The NCs were redissolved in 2 mL chloroform and filtered with a 0.2 μm hydrophobic syringe filter.

ETT Ligand Exchange				
	Estimated NC concentration in CHCl ₃ [mmol/mL]	ETT 2.8M in CHCl ₃ [mL]	Molar Excess ETT vs. NCs	Time [h]
Trig. pyr. CIS	0.025	2	~220	20
El. CIS	0.013	2	~450	20
CIGS	0.006	2	~930	30

Table 5.1: ETT Ligand Exchange Conditions for CI(G)S NCs.

5.3 Ligand Exchange and Surface Modification

5.3.1 1-Ethyl-5-thiotetrazole (ETT)

Ligand exchange of the CI(G)S NCs with ETT was conducted in solution. In a typical experiment, 1 mL of a 0.025 M trigonal pyramidal CIS NC solution in chloroform, that had been precipitated once with 2-propanol, was mixed with 2 mL of a 2.8 M ETT chloroform solution (220 fold molar ligand excess, conditions for ligand exchange, see table 5.1).

The ligand exchange mixture was stirred at 50 °C for 20 hours for CIS, respectively 30 hours for CIGS NCs and subsequently precipitated once with *n*-hexane.

5.3.2 1-Methyl-5-thiotetrazole (MTT)

For efficiently stabilizing CI(G)S NCs with MTT, ligand exchange variations were performed. Elongated CIS NCs were ligand exchanged with MTT under the same conditions like described in 5.3.1. CI(G)S NC ligand exchange with MTT was modified. The NCs were precipitated once more with 2-propanol from their initial purified chloroform solution. Subsequently, a high concentrated (5.6 M) MTT solution in tetrahydrofuran was used for incubating the CI(G)S NCs. The solutions were combined like described in 5.3.1 and stirred at 50 °C for 68 hours to enable ligand exchange.

The yield of MTT ligand exchanged trigonal pyramidal CIS and CIGS NCs generally was lower than with ETT exchange.

5.3.3 Meerwein's Salt (Et_3OBF_4)

OLA capped CI(G)S NCs were drop-coated onto a silicon substrate and soaked with a 500 mM Et_3OBF_4 solution (95 mg in 10 mL dichloromethane). The immersed substrates were rinsed with *n*-hexane to remove residual Meerwein's salt.

5.4 2D Indium Selenide Nanosheets

The indium selenide nanosheet synthesis is a modified approach based on a synthesis by Koo *et al.*^[95]

0.078 mmol (17 mg) indium(III) chloride were combined with 4.91 g octadecylamine (ODA) in a 25 mL threenecked flask and heated under oilpump vacuum at 75 °C to allow ODA to liquefy. Subsequently, the indium(III) chloride mixture was set under nitrogen, heated to 130 °C for 10 minutes and then cooled to 100 °C. Meanwhile, 0.30 mmol (37 mg) selenourea in 4.0 mL 1-octadecene (ODE) were heated to 220 °C in a separate flask to allow dissolution of the selenium precursor. After cooling to 120 °C, the selenourea solution was transferred from the flask by syringe and rapidly injected into the indium(III) chloride mixture.

The combined reaction mixture was heated to 240 °C for one hour and quenched by slowly cooling it to room temperature. At 100 °C, 5 mL toluene were added to the solution to keep it fluid.

For purification, 10 mL 2-propanol were added to the crude product and it was centrifuged at 5000 rpm for 5 minutes. The colorless supernatant was discarded and the sediment redispersed in 3 mL toluene. The solution was precipitated three additional times with 2-propanol and centrifuged at 10000 rpm.

The sediment from the last precipitation step was redispersed in chloroform and used for characterization.

For monitoring the nanosheet formation (see 3.10), the reactions were quenched at 5 min, 15 min, 30 min and 60 min respectively.

5.5 GaAs Nanocrystals

For all syntheses, a 25 mL three-neck flask was placed in a heating mantle and equipped with a condenser, a thermocouple and a septum. The reaction components were kept under oil pump vacuum at 120 °C for one hour to remove residual oxygen and water before they were set under nitrogen and the reaction was started.

GaAs NC Synthesis In a standard GaAs NC synthesis, 0.13 mmol GaCl₃ (22 mg) and 0.14 mmol Mg₃As₂ (31 mg) were mixed with 1 g TOPO as stabilizing agent and 10 mL ODE as solvent. The reaction mixture was set under nitrogen, heated to 315 °C and 0.4 mmol of *n*-butyllithium (0.25 mL of a solution of 1.6 M *n*-butyllithium in *n*-hexane) diluted in 4 mL ODE were added dropwise to the reaction mixture with a syringe pump at a rate of 10 mL/h. The solution rapidly turned greyish during addition of the *n*-butyllithium. Within 30 minutes the color changed to brownish red. Upon further progression of the reaction, the solution got turbid and turned dark brown. After 90 minutes, the mixture was cooled to 280 °C and kept at this temperature for an additional hour. Subsequently, it was cooled to 100 °C and 10 mL of toluene were added before the crude product was centrifuged at 4500 rpm for 10 minutes to obtain a clear deep brownish supernatant which was separated from the sediment. The NCs were precipitated from the supernatant by adding 10 mL of acetone or methanol and redispersed in toluene.

This procedure was performed three to five times. The precipitation of the NCs and all characterization steps were performed under air.

The reaction conditions for synthesizing InP, InAs and GaP can be found in *Chemistry of Materials*, 2013, 25, 1377-1383.^[18].

5.6 Methods and Equipment

Transmission Electron Microscopy (TEM)

TEM imaging was conducted with a JEOL JEM 2200FS (UHR) with *CESCOR* and *CETCOR* corrector at an acceleration voltage of 200 kV, a Philips CM 300 UT at an acceleration voltage of 200 kV or a JEOL JEM 1011 microscope at 100 kV equipped with a CCD camera.

Energy dispersive X-ray spectroscopy (EDS) was performed using either a Si(Li) JEOL JED-2300 energy dispersive X-ray detector installed on the JEOL JEM 2200FS or an EDAX DX-4 system installed at the Philips CM 300 UT.

Scanning Electron Microscopy (SEM)

SEM images were obtained on a LEO1550 scanning electron microscope with a spatial resolution of ~ 1 nm or a FEI Quanta 3D FEG.

Powder X-ray Diffraction (XRD)

Powder XRDs were recorded with a Philipps X'Pert-diffractometer with BRAGG-Brentano-geometry on applying copper-K α radiation. Samples of NC solutions were dropped onto a single crystal Si support plate and the solvent was evaporated before the measurement was started.

Attenuated Total Reflectance Fourier Transformation Infrared Spectroscopy (ATR-FTIR)

IR spectra were recorded with a Bruker Equinox 55 spectrometer by applying ATR-FTIR technique. The dried NC sample was placed on the crystal of the ATR unit and the spectra were recorded in the range of 600-4000 cm^{-1} .

Thermogravimetric Analysis (TGA)

TGA was carried out using a Netzsch TG 209 C in the temperature range of 25-550 $^{\circ}\text{C}$, typically with a heating rate of 20 $^{\circ}\text{C}/\text{min}$ under nitrogen atmosphere. Subsequently, samples were heated from 550-900 $^{\circ}\text{C}$ under oxygen/nitrogen atmosphere, typically at a rate of 20 $^{\circ}\text{C}/\text{min}$.

X-ray Photoelectron Spectroscopy (XPS)

XPS was performed at the *Optics Beamline SurICat* at BESSY II in Berlin, Germany. Synchrotron radiation of 1254 eV and a Scienta SES100 electron energy analyzer were used to acquire photoemission spectra. CuInSe₂ samples were dropped from ETT stabilized solution onto *highly ordered pyrolytic graphite* (HOPG) for the measurement.










Small Angle X-Ray Scattering (SAXS)

SAXS experiments were performed at a rotating anode device consisting of a rotating copper (Cu) anode (Seifert, Ahrensburg), crossed Goebel mirrors, and an image plate detector (Fuji) at a sample-detector distance of 1.0 m. The revealed scattering patterns were radially integrated, transformed into SAXS curves and analyzed with the software Scatter^[122]. Scatter is an application for analyzing SAXS and *Small Angle Neutron Scattering* (SANS) curves and patterns of nano- and mesoscopically structured materials.








Characterization of Electrical Transport and Conductivity Measurements

Electrical measurements were performed on a 4200-SCS semiconductor characterization system from Keithley Instruments inside the VFTTP4 probestation by Lake Shore Cryotronics.










5.7 Chemicals - Safety and Waste Disposal

Substance ^[123,124]	GHS icon	H/P Statement	Disposal
Acetone		H225-H319-H336; P210-P261-P305+ P351+P338	(1)
Z-1-Amino-9-octadecene		H314-H400; P273- P280-P305+351+338- P310	(1)
Chloroform		H351-H302-H373- H315; P302+352-P314	(2)
Copper(I) acetate		H315-H319-H335; P261-P305+351+338	(3)
Copper(I) chloride		H302-H400-H410 P273	(3)
Dichloromethane		H351; P281-308+ 313	(2)
1-Ethyl-5-thiotetrazole		H315-H319-H335 P261-P305+351+338	(1)
Gallium(III) bromide		H314; P280-P305+ P351+P338-P310	(3)
Gallium(III) chloride		H314; P280-P305+ P351+P338-P310	(3)









5.7 Chemicals - Safety and Waste Disposal

Substance ^[123,124]	GHS icon	H/P Statement	Disposal
Gallium(III) fluoride		H302+H312+H332; P280	(3)
Gallium(III) iodide		H314-H317-H361; P280-P305+351+338- P310	(3)
<i>n</i> -Heptane		H225-H304-H315- H336-H410; P210- P273-P301+P310- P331-P302+P352- P403+P235	(1)
<i>n</i> -Hexane		H225-H361f-H304- H373-H315-H336- H411; P210-P240- P273-P301+P310- P331-P302+P352- P403+P235	(1)
Indium(III) acetate		H315-H319-H335; P261-P305+351+ P338	(3)
Indium(III) acetylacetonate		H302+H312+H332- H315-H319-H335; P261-P280-P305+ P351+338	(3)
Indium(III) bromide		H315-H319-H335; P261- P305+P351+P338	(3)


5 Experimental

Substance ^[123,124]	GHS icon	H/P Statement	Disposal
Indium(III) chloride		H302-H314; P280- P305+351+338-P310	(3)
Indium(III) fluoride		H315-H319-H335; P261- P305+P351+P338	(3)
Indium(III) iodide		H317-H361; P281	(3)
Magnesium Arsenide Mg ₃ As ₂		H301+H331-H410; P261-P273-P304+ P340-P309+P310	(3)
Methanol		H225-H331-H311- H301-H370; P210- P233-P280-P302+352- P309+310	(1)
1-Methyl-5- thiotetrazole		H315-H319-H335 P261-P305+351+338	(1)
Octadecylamine		H315-H319-H335; P261-P305+351+ P338	(1)
1-Octadecene		H304; P301+310-P331; EUH066	(1)
2-Propanol		H225-H319-H336; P210-P233- P305+351+338	(1)

5.7 Chemicals - Safety and Waste Disposal

Substance ^[123,124]	GHS icon	H/P Statement	Disposal
Selenourea SeC(NH ₂) ₂		H301-H331-H373- H410; P261-P273- P301+310-P311-P501	(1)
Selenium		H310-H331-H373 H413; P261-P301+ P310-P311	(3)
Bis(trimethylsilyl)- selenide (TMS) ₂ Se		H226-H331-H311- H301; P261-P280- P301+310	(4)
Tetrachloroethylene		H351-H411; P273-P281	(2)
Tetrahydrofuran		H225-H319-H335- H351; P210-P233- P243-P305+351+ P338	(1)
Toluene		H225-H304-H315- H336-H361d-H373; P210-P261-P281- P301+310-P331	(1)
Triethyloxonium- tetrafluoroborate (Et ₃ OBf ₄)		H314; P280-P305+ P351+338-P310	(5)
Trioctylphosphine		H314; P280-P305+ P351+338-P310	(1)

5 Experimental

Substance ^[123,124]	GHS icon	H/P Statement	Disposal
Trioctylphosphine oxide		H315-H318; P280-P305+P351+P338	(1)

Disposal Key

- (1) dissolve and dispose of in canister for non-halogenated organic solvents (blue)
- (2) dissolve and dispose of in canister for halogenated organic solvents (red)
- (3) dissolve carefully in diluted hydrochloric acid and dispose of in canister for inorganic acids
- (4) abreaction in 2-propanol followed by complete abreaction in ethanol, then dispose of in canister for non-halogenated solvents (blue)
- (5) abreaction in 2-propanol followed by complete abreaction in ethanol, then dispose of in canister for halogenated organic solvents (red)

6 GHS List

Table 6.2: All H, EUH, and P Statements.

Identifier	Statement
H200	Unstable explosives.
H201	Explosive; mass explosion hazard.
H202	Explosive, severe projection hazard.
H203	Explosive; fire, blast or projection hazard.
H204	Fire or projection hazard.
H205	May mass explode in fire.
H220	Extremely flammable gas.
H221	Flammable gas.
H222	Extremely flammable aerosol.
H223	Flammable aerosol.
H224	Extremely flammable liquid and vapour.
H225	Highly flammable liquid and vapour.
H226	Flammable liquid and vapour.
H228	Flammable solid.
H240	Heating may cause an explosion.
H241	Heating may cause a fire or explosion.
H242	Heating may cause a fire.
H250	Catches fire spontaneously if exposed to air.
H251	Self-heating; may catch fire.
H252	Self-heating in large quantities; may catch fire.
H260	In contact with water releases flammable gases which may ignite spontaneously.
H261	In contact with water releases flammable gases.

continues on next page

Identifier	Statement
H270	May cause or intensify fire; oxidiser.
H271	May cause fire or explosion; strong oxidiser.
H272	May intensify fire; oxidiser.
H280	Contains gas under pressure; may explode if heated.
H281	Contains refrigerated gas; may cause cryogenic burns or injury.
H290	May be corrosive to metals.
H300	Fatal if swallowed.
H301	Toxic if swallowed.
H302	Harmful if swallowed.
H304	May be fatal if swallowed and enters airways.
H310	Fatal in contact with skin.
H311	Toxic in contact with skin.
H312	Harmful in contact with skin.
H314	Causes severe skin burns and eye damage.
H315	Causes skin irritation.
H317	May cause an allergic skin reaction.
H318	Causes serious eye damage.
H319	Causes serious eye irritation.
H330	Fatal if inhaled.
H331	Toxic if inhaled.
H332	Harmful if inhaled.
H334	May cause allergy or asthma symptoms or breathing difficulties if inhaled.
H335	May cause respiratory irritation.
H336	May cause drowsiness or dizziness.
H340	May cause genetic defects. <i><state route of exposure if it is conclusively proven that no other routes of exposure cause the hazard></i>
H341	Suspected of causing genetic defects. <i><state route of exposure if it is conclusively proven that no other routes of exposure cause the hazard></i>

continues on next page

Identifier	Statement
H350	May cause cancer. <i><state route of exposure if it is conclusively proven that no other routes of exposure cause the hazard></i>
H351	Suspected of causing cancer. <i><state route of exposure if it is conclusively proven that no other routes of exposure cause the hazard></i>
H360	May damage fertility or the unborn child. <i><state specific effect if known> <state route of exposure if it is conclusively proven that no other routes of exposure cause the hazard></i>
H361	Suspected of damaging fertility or the unborn child. <i><state specific effect if known> <state route of exposure if it is conclusively proven that no other routes of exposure cause the hazard></i>
H362	May cause harm to breast-fed children.
H370	Causes damage to organs <i><or state all organs affected, if known></i> . <i><state route of exposure if it is conclusively proven that no other routes of exposure cause the hazard></i>
H371	May cause damage to organs <i><or state all organs affected, if known></i> . <i><state route of exposure if it is conclusively proven that no other routes of exposure cause the hazard></i>
H372	Causes damage to organs <i><or state all organs affected, if known></i> through prolonged or repeated exposure. <i><state route of exposure if it is conclusively proven that no other routes of exposure cause the hazard></i>
H373	May cause damage to organs <i><or state all organs affected, if known></i> through prolonged or repeated exposure. <i><state route of exposure if it is conclusively proven that no other routes of exposure cause the hazard></i>
H400	Very toxic to aquatic life.
H410	Very toxic to aquatic life with long lasting effects.
H411	Toxic to aquatic life with long lasting effects.
H412	Harmful to aquatic life with long lasting effects.
H413	May cause long lasting harmful effects to aquatic life.
H350i	May cause cancer by inhalation.
H360F	May damage fertility.

continues on next page

Identifier	Statement
H360D	May damage the unborn child.
H361f	Suspected of damaging fertility.
H361d	Suspected of damaging the unborn child.
H360FD	May damage fertility. May damage the unborn child.
H361fd	Suspected of damaging fertility. Suspected of damaging the unborn child.
H360Fd	May damage fertility. Suspected of damaging the unborn child.
H360Df	May damage the unborn child. Suspected of damaging fertility.
EUH001	Explosive when dry.
EUH006	Explosive with or without contact with air.
EUH014	Reacts violently with water.
EUH018	In use may form flammable/explosive vapour-air mixture.
EUH019	May form explosive peroxides.
EUH044	Risk of explosion if heated under confinement.
EUH029	Contact with water liberates toxic gas.
EUH031	Contact with acids liberates toxic gas.
EUH032	Contact with acids liberates very toxic gas.
EUH066	Repeated exposure may cause skin dryness or cracking.
EUH070	Toxic by eye contact.
EUH071	Corrosive to the respiratory tract.
EUH059	Hazardous to the ozone layer.
EUH201	Contains lead. Should not be used on surfaces liable to be chewed or sucked by children.
EUH201A	Warning! contains lead.
EUH202	Cyanoacrylate. Danger. Bonds skin and eyes in seconds. Keep out of the reach of children.
EUH203	Contains chromium (VI). May produce an allergic reaction.
EUH204	Contains isocyanates. May produce an allergic reaction.
EUH205	Contains epoxy constituents. May produce an allergic reaction.

continues on next page

Identifier	Statement
EUH206	Warning! Do not use together with other products. May release dangerous gases (chlorine).
EUH207	Warning! Contains cadmium. Dangerous fumes are formed during use. See information supplied by the manufacturer. Comply with the safety instructions.
EUH208	Contains <name of sensitising substance>. May produce an allergic reaction.
EUH209	Can become highly flammable in use.
EUH209A	Can become flammable in use.
EUH210	Safety data sheet available on request.
EUH401	To avoid risks to human health and the environment, comply with the instructions for use.
P101	If medical advice is needed, have product container or label at hand.
P102	Keep out of reach of children.
P103	Read label before use.
P201	Obtain special instructions before use.
P202	Do not handle until all safety precautions have been read and understood.
P210	Keep away from heat/sparks/open flames/hot surfaces. — No smoking.
P211	Do not spray on an open flame or other ignition source.
P220	Keep/Store away from clothing/.../combustible materials.
P221	Take any precaution to avoid mixing with combustibles ...
P222	Do not allow contact with air.
P223	Keep away from any possible contact with water, because of violent reaction and possible flash fire.
P230	Keep wetted with ...
P231	Handle under inert gas.
P232	Protect from moisture.
P233	Keep container tightly closed.
P234	Keep only in original container.
P235	Keep cool.

continues on next page

Identifier	Statement
P240	Ground/bond container and receiving equipment.
P241	Use explosion-proof electrical/ventilating/lighting/... equipment.
P242	Use only non-sparking tools.
P243	Take precautionary measures against static discharge.
P244	Keep reduction valves free from grease and oil.
P250	Do not subject to grinding/shock/.../friction.
P251	Pressurized container: Do not pierce or burn, even after use.
P260	Do not breathe dust/fume/gas/mist/vapours/spray.
P261	Avoid breathing dust/fume/gas/mist/vapours/spray.
P262	Do not get in eyes, on skin, or on clothing.
P263	Avoid contact during pregnancy/while nursing.
P264	Wash ... thoroughly after handling.
P270	Do not eat, drink or smoke when using this product.
P271	Use only outdoors or in a well-ventilated area.
P272	Contaminated work clothing should not be allowed out of the workplace.
P273	Avoid release to the environment.
P280	Wear protective gloves/protective clothing/eye protection/face protection.
P281	Use personal protective equipment as required.
P282	Wear cold insulating gloves/face shield/eye protection.
P283	Wear fire/flame resistant/retardant clothing.
P284	Wear respiratory protection.
P285	In case of inadequate ventilation wear respiratory protection.
P231 + P232	Handle under inert gas. Protect from moisture.
P235 + P410	Keep cool. Protect from sunlight.
P301	IF SWALLOWED:
P302	IF ON SKIN:
P303	IF ON SKIN (or hair):
P304	IF INHALED:
P305	IF IN EYES:

continues on next page

Identifier	Statement
P306	IF ON CLOTHING:
P307	IF exposed:
P308	IF exposed or concerned:
P309	IF exposed or if you feel unwell:
P310	Immediately call a POISON CENTER or doctor/physician.
P311	Call a POISON CENTER or doctor/physician.
P312	Call a POISON CENTER or doctor/physician if you feel unwell.
P313	Get medical advice/attention.
P314	Get medical advice/attention if you feel unwell.
P315	Get immediate medical advice/attention.
P320	Specific treatment is urgent (see ... on this label).
P321	Specific treatment (see ... on this label).
P322	Specific measures (see ... on this label).
P330	Rinse mouth.
P331	Do NOT induce vomiting.
P332	If skin irritation occurs:
P333	If skin irritation or rash occurs:
P334	Immerse in cool water/wrap in wet bandages.
P335	Brush off loose particles from skin.
P336	Thaw frosted parts with lukewarm water. Do not rub affected area.
P337	If eye irritation persists:
P338	Remove contact lenses, if present and easy to do. Continue rinsing.
P340	Remove victim to fresh air and keep at rest in a position comfortable for breathing.
P341	If breathing is difficult, remove victim to fresh air and keep at rest in a position comfortable for breathing.
P342	If experiencing respiratory symptoms:
P350	Gently wash with plenty of soap and water.
P351	Rinse cautiously with water for several minutes.

continues on next page

Identifier	Statement
P352	Wash with plenty of soap and water.
P353	Rinse skin with water/shower.
P360	Rinse immediately contaminated clothing and skin with plenty of water before removing clothes.
P361	Remove/Take off immediately all contaminated clothing.
P362	Take off contaminated clothing and wash before reuse.
P363	Wash contaminated clothing before reuse.
P370	In case of fire:
P371	In case of major fire and large quantities:
P372	Explosion risk in case of fire.
P373	DO NOT fight fire when fire reaches explosives.
P374	Fight fire with normal precautions from a reasonable distance.
P375	Fight fire remotely due to the risk of explosion.
P376	Stop leak if safe to do so.
P377	Leaking gas fire: Do not extinguish, unless leak can be stopped safely.
P378	Use ... for extinction.
P380	Evacuate area.
P381	Eliminate all ignition sources if safe to do so.
P390	Absorb spillage to prevent material damage.
P391	Collect spillage.
P301 + P310	IF SWALLOWED: Immediately call a POISON CENTER or doctor/physician.
P301 + P312	IF SWALLOWED: Call a POISON CENTER or doctor/physician if you feel unwell.
P301 + P330 + P331	IF SWALLOWED: rinse mouth. Do NOT induce vomiting.
P302 + P334	IF ON SKIN: Immerse in cool water/wrap in wet bandages.
P302 + P350	IF ON SKIN: Gently wash with plenty of soap and water.
P302 + P352	IF ON SKIN: Wash with plenty of soap and water.
P303 + P361 + P353	IF ON SKIN (or hair): Remove/Take off immediately all contaminated clothing. Rinse skin with water/shower.

continues on next page

Identifier	Statement
P304 + P340	IF INHALED: Remove victim to fresh air and keep at rest in a position comfortable for breathing.
P304 + P341	IF INHALED: If breathing is difficult, remove victim to fresh air and keep at rest in a position comfortable for breathing.
P305 + P351 + P338	IF IN EYES: Rinse cautiously with water for several minutes. Remove contact lenses, if present and easy to do. Continue rinsing.
P306 + P360	IF ON CLOTHING: Rinse immediately contaminated clothing and skin with plenty of water before removing clothes.
P307 + P311	IF exposed: Call a POISON CENTER or doctor/physician.
P308 + P313	IF exposed or concerned: Get medical advice/attention.
P309 + P311	IF exposed or if you feel unwell: Call a POISON CENTER or doctor/physician.
P332 + P313	If skin irritation occurs: Get medical advice/attention.
P333 + P313	If skin irritation or rash occurs: Get medical advice/attention.
P335 + P334	Brush off loose particles from skin. Immerse in cool water/wrap in wet bandages.
P337 + P313	If eye irritation persists: Get medical advice/attention.
P342 + P311	If experiencing respiratory symptoms: Call a POISON CENTER or doctor/physician.
P370 + P376	In case of fire: Stop leak if safe to do so.
P370 + P378	In case of fire: Use . . . for extinction.
P370 + P380	In case of fire: Evacuate area.
P370 + P380 + P375	In case of fire: Evacuate area. Fight fire remotely due to the risk of explosion.
P371 + P380 + P375	In case of major fire and large quantities: Evacuate area. Fight fire remotely due to the risk of explosion.
P401	Store . . .
P402	Store in a dry place.
P403	Store in a well-ventilated place.
P404	Store in a closed container.
P405	Store locked up.

continues on next page

Identifier	Statement
P406	Store in corrosive resistant/. . . container with a resistant inner liner.
P407	Maintain air gap between stacks/pallets.
P410	Protect from sunlight.
P411	Store at temperatures not exceeding /.
P412	Store at temperatures not exceeding 50/122.
P413	Store bulk masses greater than / at temperatures not exceeding /.
P420	Store away from other materials.
P422	Store contents under . . .
P402 + P404	Store in a dry place. Store in a closed container.
P403 + P233	Store in a well-ventilated place. Keep container tightly closed.
P403 + P235	Store in a well-ventilated place. Keep cool.
P410 + P403	Protect from sunlight. Store in a well-ventilated place.
P410 + P412	Protect from sunlight. Do not expose to temperatures exceeding 50/122.
P411 + P235	Store at temperatures not exceeding /. Keep cool.
P501	Dispose of contents/container to . . .

GHS-Pictograms

GHS01		GHS02	
GHS03		GHS04	
GHS05		GHS06	
GHS07		GHS08	
GHS09			

Table 6.1: GHS-Pictograms: GHS01-explosive, GHS02-flammable, GHS03-oxidizing, GHS04-compressed gas, GHS05-corrosive, GHS06-toxic, GHS07-irritant, GHS08-health hazard, GHS09-environmentally damaging.

Acronyms

CIS	CuInSe ₂
CIGS	CuIn _{1-x} Ga _x Se ₂
ETT	1-Ethyl-5-thiotetrazole
FWHM	Full width at half maximum
HOPG	Highly Ordered Pyrolytic Graphite
MTT	1-Methyl-5-thiotetrazole
NC	Nanocrystal
OLA	Oleylamine
ODE	1-Octadecene
ODA	Octadecylamine
QD	Quantum Dot
SAED	Selected Area Electron Diffraction
SANS	Small Angle Neutron Scattering
SAXS	Small Angle X-ray Scattering
SEM	Scanning Electron Microscopy
STEM	Scanning Transmission Electron Microscopy
TEM	Transmission Electron Microscopy
THF	Tetrahydrofuran
TOP	<i>n</i> -Trioctylphosphine
TOPO	Tri- <i>n</i> -octylphosphine oxide
XPS	X-ray Photoelectron Spectroscopy
XRD	(Powder-)X-ray diffraction

Bibliography

- [1] Hergert, F.; Jost, S.; Hock, R.; Purwins, M. *J. Solid State Chem.* **2006**, *179*, 2394–2415.
- [2] Shockley, W.; Queisser, H. J. *J. Appl. Phys.* **1961**, *32*, 510–519.
- [3] Stanbery, B. J. *Crit. Rev. Solid State Mater. Sci.* **2002**, *27*, 73–117.
- [4] Jaffe, J. E.; Zunger, A. *Phys. Rev. B* **1984**, *29*, 1882–1906.
- [5] Hergert, F.; Jost, S.; Hock, R.; Purwins, M.; Palm, J. *phys. stat. sol. (a)* **2006**, *203*, 2615–2623.
- [6] Hergert, F.; Hock, R.; Weber, A.; Purwins, M.; Palm, J.; Probst, V. *J. Phys. Chem. Solids* **2005**, *66*, 1903–1907.
- [7] Murray, C. B.; Kagan, C. R.; Bawendi, M. G. *Ann. Rev. Mater. Sci.* **2000**, *30*, 545–610.
- [8] Reiss, H. *J. Chem. Phys.* **1950**, *19*, 482–487.
- [9] LaMer, V. K.; Dinegar, R. H. *J. Am. Chem. Soc.* **1950**, *72*, 4847–54.
- [10] Murray, C. B.; Norris, D. J.; Bawendi, M. G. *J. Am. Chem. Soc.* **1993**, *115*, 8706–8715.
- [11] R. Heath, *J. Chem. Soc. Rev.* **1998**, *27*, 65–71.
- [12] Lauth, J.; Strupeit, T.; Kornowski, A.; Weller, H. *Chem. Mater.* **2013**, *25*, 1377–1383.
- [13] Mekis, I.; Talapin, D. V.; Kornowski, A.; Haase, M.; Weller, H. *J. Phys. Chem. B* **2003**, *107*, 7454–7462.
- [14] Peng, Z. A.; Peng, X. *J. Am. Chem. Soc.* **2001**, *123*, 183–184.
- [15] Wang, F.; Richards, V. N.; Shields, S. P.; Buhro, W. E. *Chem. Mater.* **2013**, DOI: 10.1021/cm402139r.

- [16] Zheng, H.; Smith, R. K.; Jun, Y.-w.; Kisielowski, C.; Dahmen, U.; Alivisatos, A. P. *Science* **2009**, *324*, 1309–1312.
- [17] Bogush, G.; Zukoski, C. F. *J. Colloid Interface Sci.* **1991**, *142*, 19–34.
- [18] Lauth, J.; Marbach, J.; Meyer, A.; Dogan, S.; Klinke, C.; Kornowski, A.; Weller, H. *Adv. Funct. Mater.* **2013**, DOI: 10.1002/adfm.201301957.
- [19] Panthani, M. G.; Akhavan, V.; Goodfellow, B.; Schmidtke, J. P.; Dunn, L.; Dodabalapur, A.; Barbara, P. F.; Korgel, B. A. *J. Am. Chem. Soc.* **2008**, *130*, 16770–16777.
- [20] Efros, A. L.; Efros, A. L. *Sov. Phys. Semicond.* **1982**, *16*, 772.
- [21] Brus, L. E. *J. Chem. Phys.* **1983**, *79*, 5566–5571.
- [22] Brus, L. *J. Chem. Phys.* **1984**, *80*, 4403–4409.
- [23] Weller, H. *Adv. Mater.* **1993**, *5*, 88–95.
- [24] Castro, S. L.; Bailey, S. G.; Raffaele, R. P.; Banger, K. K.; Hepp, A. F. *Chem. Mater.* **2003**, *15*, 3142–3147.
- [25] Rincón, C.; Márquez, R. *J. Phys. Chem. Solids* **1999**, *60*, 1865–1873.
- [26] Zhong, H.; Li, Y.; Ye, M.; Zhu, Z.; Zhou, Y.; Yang, C.; Li, Y. *Nanotechnology* **2007**, *18*, 025602–.
- [27] Zhong, H.; Wang, Z.; Bovero, E.; Lu, Z.; van Veggel, F. C. J. M.; Scholes, G. D. *J. Phys. Chem. C* **2011**, *115*, 12396–12402.
- [28] Allen, P. M.; Bawendi, M. G. *J. Am. Chem. Soc.* **2008**, *130*, 9240–9241.
- [29] Nose, K.; Omata, T.; Otsuka-Yao-Matsuo, S. *J. Phys. Chem. C* **2009**, *113*, 3455–3460.
- [30] Tauc, J.; Grigorovici, R.; Vancu, A. *phys. stat. sol. (b)* **1966**, *15*, 627–637.
- [31] Sagnes, B.; Salesse, A.; Artaud, M.; Duchemin, S.; Bougnot, J.; Bougnot, G. *J. Cryst. Growth* **1992**, *124*, 620–627.
- [32] Duchemin, S.; Artaud, M.; Ouchen, F.; Bougnot, J.; Pougnet, A. *J. Mater. Sci.: Mater. Electron.* **1996**, *7*, 201–205.

-
- [33] Artaud, M.; Ouchen, F.; Martin, L.; Duchemin, S. *Thin Solid Films* **1998**, *324*, 115–123.
- [34] Geiregat, P.; Justo, Y.; Abe, S.; Flamee, S.; Hens, Z. *ACS Nano* **2013**, *7*, 987–993.
- [35] Wang, X.; Koleilat, G. I.; Tang, J.; Liu, H.; Kramer, I. J.; Debnath, R.; Brzozowski, L.; Barkhouse, D. A. R.; Levina, L.; Hoogland, S.; Sargent, E. H. *Nat Photon* **2011**, *5*, 480–484.
- [36] Beard, M. C. *J. Phys. Chem. Lett.* **2011**, *2*, 1282–1288.
- [37] Nozik, A. J. *Annu. Rev. Phys. Chem.* **2001**, *52*, 193–231.
- [38] Nozik, A. *Physica E: Low Dimens. Syst. Nanostruct.* **2002**, *14*, 115–120.
- [39] Semonin, O. E.; Luther, J. M.; Choi, S.; Chen, H.-Y.; Gao, J.; Nozik, A. J.; Beard, M. C. *Science* **2011**, *334*, 1530–1533.
- [40] Beard, M. C.; Luther, J. M.; Semonin, O. E.; Nozik, A. J. *Acc. Chem. Res.* **2013**, *46*, 1252–1260.
- [41] Yin, Y.; Alivisatos, A. P. *Nature* **2005**, *437*, 664–670.
- [42] Mourdikoudis, S.; Liz-Marzán, L. M. *Chem. Mater.* **2013**, *25*, 1465–1476.
- [43] Bullen, C.; van Embden, J.; Jasieniak, J.; Cosgriff, J. E.; Mulder, R. J.; Rizzardo, E.; Gu, M.; Raston, C. L. *Chem. Mater.* **2010**, *22*, 4135–4143.
- [44] Evans, C. M.; Evans, M. E.; Krauss, T. D. *J. Am. Chem. Soc.* **2010**, *132*, 10973–10975.
- [45] Lobo, A.; Möller, T.; Nagel, M.; Borchert, H.; Hickey, S. G.; Weller, H. *J. Phys. Chem. B* **2005**, *109*, 17422–17428.
- [46] Voitekhovich, S. V.; Talapin, D. V.; Klinke, C.; Kornowski, A.; Weller, H. *Chem. Mater.* **2008**, *20*, 4545–4547.
- [47] Kocienski, P. J.; Bell, A.; Blakemore, P. R. *Synlett* **2000**, *2000*, 365–366.

- [48] Meier, H. R.; Heimgartner, H. In *Methoden der Organischen Chemie (Houben-Weyl)*; Schumann, E., Ed.; George Thieme, Stuttgart, Germany, 1994; Vol. E8d; pp 664–795.
- [49] Rosen, E. L.; Buonsanti, R.; Llordes, A.; Sawvel, A. M.; Milliron, D. J.; Helms, B. A. *Angew. Chem. Int. Ed.* **2012**, *51*, 684–689.
- [50] Talapin, D. V.; Lee, J.-S.; Kovalenko, M. V.; Shevchenko, E. V. *Chem. Rev.* **2010**, *110*, 389–458.
- [51] Vanmaekelbergh, D.; Liljeroth, P. *Chem. Soc. Rev.* **2005**, *34*, 299–312.
- [52] Chandler, R. E.; Houtepen, A. J.; Nelson, J.; Vanmaekelbergh, D. *Phys. Rev. B* **2007**, *75*, 085325–.
- [53] Zabet-Khosousi, A.; Dhirani, A.-A. *Chem. Rev.* **2008**, *108*, 4072–4124.
- [54] Talapin, D. V.; Murray, C. B. *Science* **2005**, *310*, 86–89.
- [55] Yu, D.; Wang, C.; Guyot-Sionnest, P. *Science* **2003**, *300*, 1277–1280.
- [56] Beloborodov, I. S.; Lopatin, A. V.; Vinokur, V. M.; Efetov, K. B. *Rev. Mod. Phys.* **2007**, *79*, 469–518.
- [57] Remacle, F.; Levine, R. D. *ChemPhysChem* **2001**, *2*, 20–36.
- [58] Mentzel, T. S.; Porter, V. J.; Geyer, S.; MacLean, K.; Bawendi, M. G.; Kastner, M. A. *Phys. Rev. B* **2008**, *77*, 075316–.
- [59] de Kergommeaux, A.; Fiore, A.; Faure-Vincent, J.; Chandezon, F.; Pron, A.; de Bettignies, R.; Reiss, P. *Mater. Chem. Phys.* **2012**, *136*, 877–882.
- [60] Kovalenko, M. V.; Scheele, M.; Talapin, D. V. *Science* **2009**, *324*, 1417–1420.
- [61] Luther, J. M.; Law, M.; Song, Q.; Perkins, C. L.; Beard, M. C.; Nozik, A. J. *ACS Nano* **2008**, *2*, 271–280.
- [62] Barkhouse, D. A. R.; Pattantyus-Abraham, A. G.; Levina, L.; Sargent, E. H. *ACS Nano* **2008**, *2*, 2356–2362.
- [63] Fafarman, A. T.; Koh, W.-k.; Diroll, B. T.; Kim, D. K.; Ko, D.-K.; Oh, S. J.; Ye, X.; Doan-Nguyen, V.; Crump, M. R.; Reifsnyder, D. C.; Murray, C. B.; Kagan, C. R. *J. Am. Chem. Soc.* **2011**, *133*, 15753–15761.

-
- [64] Zhang, H.; Hu, B.; Sun, L.; Hovden, R.; Wise, F. W.; Muller, D. A.; Robinson, R. D. *Nano Lett.* **2011**, *11*, 53565361.
- [65] Ho, C.-H.; Lin, C.-H.; Wang, Y.-P.; Chen, Y.-C.; Chen, S.-H.; Huang, Y.-S. *ACS Appl. Mater. Interfaces* **2013**, *5*, 2269–2277.
- [66] Merle, J.; Bartiromo, R.; Borsella, E.; Piacentini, M.; Savoia, A. *Solid State Commun.* **1978**, *28*, 251–255.
- [67] Hogg, J. H. C. *Acta Cryst. B* **1971**, *27*, 1630–1634.
- [68] Li, Y.; Gao, J.; Li, Q.; Peng, M.; Sun, X.; Li, Y.; Yuan, G.; Wen, W.; Meyyappan, M. *J. Mater. Chem.* **2011**, *21*, 6944–6947.
- [69] Ishikawa, M.; Nakayama, T. *Jpn. J. Appl. Phys.* **1998**, *37*, L1122–.
- [70] Ye, J.; Soeda, S.; Nakamura, Y.; Nittono, O. *Jpn. J. Appl. Phys.* **1998**, *37*, 4264–.
- [71] Emziane, M.; Marsillac, S.; Bernède, J. *Mater. Chem. Phys.* **2000**, *62*, 84–87.
- [72] Marsillac, S.; Combot-Marie, A.; Bernède, J.; Conan, A. *Thin Solid Films* **1996**, *288*, 14–20.
- [73] Jasinski, J.; Swider, W.; Washburn, J.; Liliental-Weber, Z.; Chaiken, A.; Nauka, K.; Gibson, G. A.; Yang, C. C. *Appl. Phys. Lett.* **2002**, *81*, 4356–4358.
- [74] Okamoto, H. *J. Phase Equilib. Diff.* **2004**, *25*, 201–201.
- [75] Hayashi, T.; Ueno, K.; Saiki, K.; Koma, A. *J. Cryst. Growth* **2000**, *219*, 115–122.
- [76] Park, K. H.; Jang, K.; Kim, S.; Kim, H. J.; Son, S. U. *J. Am. Chem. Soc.* **2006**, *128*, 14780–14781.
- [77] Bertness, K.; Kurtz, S. R.; Friedman, D. J.; Kibbler, A. E.; Kramer, C.; Olson, J. M. *Appl. Phys. Lett.* **1994**, *65*, 989–991.
- [78] Bett, A.; Dimroth, F.; Stollwerck, G.; Sulima, O. *Appl. Phys. A: Mater. Sci. & Process.* **1999**, *69*, 119–129.
- [79] Takamoto, T.; Kaneiwa, M.; Imaizumi, M.; Yamaguchi, M. *Progr. Photovolt.: Res. Appl.* **2005**, *13*, 495–511.

- [80] Strehlow, W. H.; Cook, E. L. *J. Phys. Chem. Ref. Data* **1973**, *2*, 163–200.
- [81] Yoffe, A. *Adv. Phys.* **1993**, *42*, 173–262.
- [82] Bosi, M.; Pelosi, C. *Prog. Photovolt: Res. Appl.* **2007**, *15*, 51–68.
- [83] Nayak, J.; Mythili, R.; Vijayalakshmi, M.; Sahu, S. *Physica E: Low Dimens. Syst. Nanostruct.* **2004**, *24*, 227 – 233.
- [84] Olshavsky, M. A.; Goldstein, A. N.; Alivisatos, A. P. *J. Am. Chem. Soc.* **1990**, *112*, 9438–9439.
- [85] Manasevit, H. M. *Appl. Phys. Lett.* **1968**, *12*, 156–159.
- [86] Kuan, H.; Su, Y. K. *Semicond. Sci. Technol.* **1995**, *10*, 540–545.
- [87] Wells, R. L.; Pitt, C. G.; McPhail, A. T.; Purdy, A. P.; Shafieezad, S.; Hallock, R. B. *Chem. Mater.* **1989**, *1*, 4–6.
- [88] Kher, S. S.; Wells, R. L. *Chem. Mater.* **1994**, *6*, 2056–2062.
- [89] Uchida, H.; Curtis, C. J.; Nozik, A. J. *J. Phys. Chem.* **1991**, *95*, 5382–5384.
- [90] Uchida, H.; Curtis, C. J.; Prashant, K. V.; Jones, K. M.; Nozik, A. J. *J. Phys. Chem.* **1992**, *96*, 1156–1160.
- [91] Butler, L.; Redmond, G.; Fitzmaurice, D. *J. of Phys. Chem.* **1993**, *97*, 10750–10755.
- [92] Janik, J. F.; Wells, R. L.; Young, V. G.; Rheingold, A. L.; Guzei, I. A. *J. Am. Chem. Soc.* **1998**, *120*, 532–537.
- [93] Malik, M. A.; O’Brien, P.; Norager, S.; Smith, J. *J. Mater. Chem.* **2003**, *13*, 2591–2595.
- [94] Strupeit, T. *Nanostrukturierte III-V Halbleiter*; Physikalische Chemie; Dissertation: Universität Hamburg, 2009.
- [95] Koo, B.; Patel, R. N.; Korgel, B. A. *J. Am. Chem. Soc.* **2009**, *131*, 3134–3135.
- [96] Massa, W. *Kristallstrukturbestimmung*, 6th ed.; Vieweg+Teubner Verlag, 2009.

-
- [97] Pearson, R. G. *J. Am. Chem. Soc.* **1963**, *85*, 3533–3539.
- [98] Pearson, R. G. *Inorg. Chim. Acta* **1995**, *240*, 93–98.
- [99] Shukla, N.; Svedberg, E. B.; Ell, J. *Colloids Surf. A: Physicochem. Eng. Aspects* **2007**, *301*, 113–116.
- [100] Gómez-Zavaglia, A.; Reva, I.; Frija, L.; Cristiano, M.; Fausto, R. *J. Mol. Struct.* **2006**, *786*, 182–192.
- [101] Sägmüller, B.; Freunsch, P.; Schneider, S. *J. Mol. Struct.* **1999**, *482-483*, 231–235.
- [102] Paul, K. W.; Hurley, M. M.; Irikura, K. K. *J. Phys. Chem. A* **2009**, *113*, 2483–2490.
- [103] Piekielek, N.; Zachariah, M. R. *J. Phys. Chem. A* **2012**, *116*, 1519–1526.
- [104] Chen, I.-W.; Wang, X.-H. *Nature* **2000**, *404*, 168–171.
- [105] Tinoco, T.; Rincón, C.; Quintero, M.; Pérez, G. S. *phys. stat. sol. (a)* **1991**, *124*, 427–434.
- [106] Chen, H.; Yu, S.-M.; Shin, D.-W.; Yoo, J.-B. *Nanoscale Res. Lett.* **2009**, *5*, 217–223.
- [107] Partain, L. D.; Schneider, R. A.; Donaghey, L. F.; McLeod, P. S. *J. Appl. Phys.* **1985**, *57*, 5056–5065.
- [108] Llanos, J.; Buljan, A.; Mujica, C.; Ramírez, R. *J Alloys Compd* **1996**, *234*, 40–42.
- [109] Liu, W.-L.; Wu, M.-Q.; Zhou, R.-C.; Yan, L.-D.; Zhang, S.-R.; Zhang, Q.-Y. *Bull. Korean Chem. Soc.* **2011**, *32*, 4332–4336.
- [110] Cai, Y.; Wolfkühler, D.; Myalitsin, A.; Perlich, J.; Meyer, A.; Klinke, C. *ACS Nano* **2010**, *5*, 67–72.
- [111] Zhang, S. B.; Wei, S.-H.; Zunger, A.; Katayama-Yoshida, H. *Phys. Rev. B* **1998**, *57*, 9642–9656.
- [112] Jaffe, J. E.; Zunger, A. *Phys. Rev. B* **2001**, *64*, 241304–4.
- [113] Zhang, S. B.; Wei, S.-H.; Zunger, A. *Phys. Rev. Lett.* **1997**, *78*, 4059–4062.

- [114] Nagpal, P.; Klimov, V. I. *Nat Commun* **2011**, *2*, 486–.
- [115] Dogan, S.; Bielewicz, T.; Cai, Y.; Klinke, C. *Appl. Phys. Lett.* **2012**, *101*, 073102–4.
- [116] Schliehe, C.; Juarez, B. H.; Pelletier, M.; Jander, S.; Greshnykh, D.; Nagel, M.; Meyer, A.; Foerster, S.; Kornowski, A.; Klinke, C.; Weller, H. *Science* **2010**, *329*, 550–553.
- [117] Kovar, R. A.; Loaris, G.; Derr, H.; Callaway, J. O. *Inorg. Chem.* **1974**, *13*, 1476–1479.
- [118] Kovar, R. A.; Derr, H.; Brandau, D.; Callaway, J. O. *Inorg. Chem.* **1975**, *14*, 2809–2814.
- [119] Byrne, E. K.; Parkanyi, L.; Theopold, K. H. *Science* **1988**, *241*, 332–334.
- [120] Sandroff, C. J.; Harbison, J. P.; Ramesh, R.; Andrejco, M. J.; Hedge, M. S.; Chang, C. C.; Vogel, E. M.; Hwang, D. M. *Science* **1989**, *245*, 391–393.
- [121] Sturge, M. D. *Phys. Rev.* **1962**, *127*, 768–773.
- [122] Förster, S.; Apostol, L.; Bras, W. *J. Appl. Cryst.* **2010**, *43*, 639–646.
- [123] euSDB MSDS search, found at <http://www.eusdb.de>, as of 10/2013.
- [124] IFA GESTIS substance database, found at <http://biade.itrust.de>, as of 10/2013.

Acknowledgments

I would like to express my gratitude to the people who constantly supported and accompanied me through this interesting, exciting and instructive time of my life.

I would like to thank Prof. Horst Weller for providing me the support and framework for carrying out the present work on this interesting and challenging topic self-determined and with a high degree of freedom.

My special thank goes to Andreas Kornowski who was always there for debating the concepts and contents of this work. The discussions with him represented important steps for advancing this work.

Many thanks go to Prof. Christian Klinke who motivated me to spend time on elucidating electrical transport processes and who is always enthusiastic about new research ideas.

I would like to thank Dr. Tim Strupeit for inspiring me to search my scientific way in this group and for introducing me to the world of the famous III-V semiconductor nanocrystals.

Almut Barck is greatly acknowledged for measuring hundreds of XRDs and for accepting the challenge of the heating chamber.

I would also like to thank Dr. Andreas Meyer for performing the SAXS measurements and Carsten Ott from the CAN company in Hamburg for synthesizing and providing the 1-ethyl-5-thiotetrazole ligand.

A special thank goes to my former students Friederieke Gorris and Robert Seher. Your motivation to join our research area more than once kept me going.

I would like to thank my Bachelorstudents Friederieke Gorris, Jakob Marbach and Sascha Kull who helped to advance this work. My former trainees Robert Seher, Dawid Bednarski and Tobias Ehmke is thanked for their practical help in the lab.

My "roommates" from office number 253: Thank you for the great time!

I would like to thank all members of the AK Weller group for a great time during the last years. It has been a pleasure to work with you.

My (former office) colleagues and dearest friends Dr. Alina Chanaewa and Dr. Hauke Heller are greatly acknowledged for their dedication to discuss all kinds of problems and sometimes solve them in unusual but efficient ways including punching bags and the odd glass or two of wine.

Acknowledgments

I am indebted to my family and friends who endured years of excitement with me and are always at my side. I love you!

Curriculum Vitae

Omitted because of data protection.

Entfällt aus Datenschutzgründen.

Publications

Publications

1. **Lauth, J.**, Marbach, J., Meyer, A., Dogan, S., Klinke, C., Kornowski, A., Weller, H. "Virtually Bare Nanocrystal Surfaces - Significantly Enhanced Electrical Transport in CuInSe₂ and CuIn_{1-x}GaxSe₂ Thin Films upon Ligand Exchange with Thermally Degradable 1-Ethyl-5-thiotetrazole", *Advanced Functional Materials*, **2013**, DOI:10.1002/adfm.201301957.
2. **Lauth, J.**, Strupeit, T., Kornowski, A., Weller, H. "A Transmetalation Route for Colloidal GaAs Nanocrystals and Additional III-V Semiconductor Materials" *Chemistry of Materials* (Special Issue: Synthetic and Mechanistic Advances in Nanocrystal Growth), **2013**, *25*, 1377-1383.

Contributed Talks

1. "Virtually Bare Nanocrystal Surfaces - Significantly Enhanced Electrical Transport in Copper Indium (Gallium) Selenide Nanocrystal Thin Films upon Ligand Exchange with Thermally Degradable 1-Ethyl-5-thiotetrazole", **J. Lauth**, J. Marbach, A. Meyer, S. Dogan, C. Klinke, A. Kornowski, H. Weller, F.13 6, *E-MRS Spring Meeting*, Strasbourg, France, **2013**.
2. "Synthesis of Colloidal GaAs Nanocrystals and their Use in Thin Film Applications", **J. Lauth**, T. Strupeit, A. Kornowski, H. Weller, *Bun-
sentagung 2011*, 110th Annual German Conference on Physical Chemistry, Berlin, Germany, **2011**.
3. "Broadening the Scope of Applications for Colloidal GaAs Nanocrystals", **J. Lauth**, T. Strupeit, A. Kornowski, H. Weller, D3.5, *MRS Spring Meeting*, San Francisco CA, **2011**.

Poster

"Synthesis of Colloidal GaAs and other III-V Semiconductor Nanocrystals by Using a Transmetalation Route", **J.Lauth**, T. Strupeit, A. Kornowski, H. Weller, *NaNaX5 2012*, Fuengirola, Spain, **2012**.

The following Bachelor's theses were conducted and published within the framework of this thesis:

1. Sascha Kull, *Ligandenaustausch an CuInSe_2 und an $\text{CuIn}_{1-x}\text{Ga}_x\text{Se}_2$ Nanokristallen*, Bachelorarbeit, Universität Hamburg, **2013**.
2. Jakob Marbach, *Ligandenaustausch an CuInSe_2 und $\text{CuIn}_{1-x}\text{Ga}_x\text{Se}_2$ Nanopartikelsystemen - Filmanfertigung und Transportmessungen*, Bachelorarbeit, Universität Hamburg, **2012**.
3. Friederike E. Gorris, *Die Qualität des Oleylamins: Der Einfluss von Isomerenreinheit und Feuchtigkeit auf die Indiumselenidnanopartikelsynthese*, Bachelorarbeit, Universität Hamburg, **2011**.

Affirmation

Hiermit erkläre ich an Eides statt, dass ich die vorliegende Arbeit selbständig verfasst und alle verwendeten Quellen und Hilfsmittel als solche gekennzeichnet habe.

Weiterhin wurden von mir zuvor keine Promotionsversuche unternommen oder diese Arbeit in gleicher oder ähnlicher Form einer anderen Prüfungsbehörde vorgelegt.

Ich bin erster und hauptverantwortlicher Autor der zwei bereits bei Verlagen erschienenen Publikationen, deren Inhalt auch Teil dieser Dissertation ist.

Hamburg, den 10.11.2013

Jannika Lauth